Atmospheric monitoring for the H.E.S.S. experiment using a single scattering lidar

Rulten, Cameron Boyd

Atmospheric monitoring for the H.E.S.S. experiment using a single scattering lidar.

by

Cameron Boyd Rulten

Submitted in conformity with the requirements

for the degree of Master of Science

Department of Physics

University of Durham

United Kingdom

Abstract

The High Energy Stereoscopic System (H.E.S.S.) is an array of 4 telescopes located in Namibia, which use the imaging atmospheric Cherenkov technique (IACT) to study astrophysical emission of gamma radiation in the energy window from 100 GeV to 50 TeV. The calorimetric nature of the technique means that the sensitivity and energy resolution of the instrument are highly dependent on atmospheric parameters.

This thesis presents the findings of atmospheric measurements taken using a 355 nm single scattering lidar. The lidar wavelength is well matched to the maximum in the Cherenkov spectrum seen by the telescopes. Monte Carlo simulation software is presented which has been developed to calculate the integral vertical lidar ratio (the ratio of extinction to backscatter) for Mie scattering by aerosols assumed to be at the H.E.S.S. site. This is found to be 29 $\pm$ 3 steradians. This ratio is used with the Fernald method to derive the probability of transmission profile, and is also compared to other lidar analysis techniques; the Klett method and the multi-angle method. The results of all 3 methods are compared to the lidar manufacturer's closed-source analysis software, with which the Klett method is found to be in strongest agreement. A model that describes the relationship between the lidar ratio and the extinction is presented. Using this with the lidar manufacturer's extinction values provides a vertical lidar ratio profile which, for the first time, provides insight into the aerosol scattering layers present at the H.E.S.S. site in Namibia. Recommendations for improvement of this research, and suggestions for incorporation of data into the H.E.S.S. analysis, have been made.

Declaration

The material contained within this thesis has not previously been submitted for a degree at Durham University or any other university. The research reported within this thesis has been conducted by the author unless indicated otherwise.

Copyright Notice

Acknowledgements

I would like to thank everyone who has supported me in writing this thesis. Particular thanks should go to my supervisors Dr. Paula Chadwick and Dr. Steve Rayner for their much appreciated encouragement, patience and feedback. They have contributed a lot of their time to reading through this thesis as well as providing useful and informative feedback. I would also like to thank other members of the Very High Energy Gamma Ray Group at Durham University including Dr. Sam Nolan and Hugh Dickinson for their patience and willingness to answer numerous questions regarding ROOT, C++ and Linux. Thanks should also go to Christos Hadjichristidis who helped me in my first few weeks by pointing me in the right direction toward all the journals and papers on lidars. A general thanks to all the other group members who I have not named here, but thank you for your encouragement and friendship. I would like to thank my family who have always believed in me and never deterred me from following my dreams. Student life generally means a low income, so thanks to all my family and friends for letting me stay with them during holidays etc. Your generosity and hospitality will never be forgotten. Last but not least a special thanks should go to Rhianne Jones who has had to put up with me and my research over this past year. This thesis has become as much a part of her life as it has mine. Thanks Rhianne for reading through my thesis to help correct all the niggling grammar and spelling errors that I am so skilled at producing.

Without all your support this thesis would not have been completed, all of you have helped me to take this first step on a long journey...

"Be it no concern

Point of no return

Go forward in reverse

This I will recall

Every time I fall

I'm setting forth in the universe..."

Eddie Vedder (2007)

Table of Contents

List of Figures

List of Tables

Introduction

The High Energy Stereoscopic System (H.E.S.S.) is an array of 4 telescopes located in Namibia, which use the imaging atmospheric Cherenkov technique (IACT) to study astrophysical emission of gamma radiation in the energy window from 100 GeV to 50 TeV. The calorimetric nature of the technique means that the sensitivity and the energy resolution of the instrument are highly dependent on atmospheric parameters. This thesis presents the findings of atmospheric measurements taken at the H.E.S.S. site using a single scattering lidar.

Chapter 1 introduces the field of very high energy gamma ray astronomy within the context of cosmic rays. This includes a discussion of the known primary interactions responsible for the creation and destruction of gamma rays within the Universe. Chapter 1 also discusses how gamma rays incident onto the Earth interact with atmospheric nuclei to produce Cherenkov light which propagates down to the ground. Various atmospheric parameters that directly impact on the amount of Cherenkov light readily available for collecting with ground based telescopes are highlighted.

Chapter 2 discusses the structure and composition of the Earth's atmosphere including different molecular and aerosol models used in atmospheric analysis.

The basic principles and theory governing the scattering of light incident onto a particle are discussed including the widely accepted Rayleigh and Mie theories. Chapter 2 also highlights how two measurable atmospheric quantities, optical depth and probability of transmission, are key atmospheric parameters required by the IACT Monte Carlo simulations used to infer the energy of primary gamma ray photons. The lidar remote sensing technique is discussed as a suitable means for measuring the probability of transmission in the atmosphere over the range from where it is expected that Cherenkov photons, as a result of very high energy gamma ray induced air showers, will propagate.

Chapter 3 introduces three widely accepted lidar analysis techniques known as the Klett method, the Fernald method and the multi-angle method. Chapter 3 also discusses how, using Mie theory, a lidar ratio can be calculated for the types of aerosols assumed to occur at the H.E.S.S. site in Namibia. This includes a discussion of how the resulting relationships between extinction and backscatter coefficients can be analysed in order to generate a vertical lidar ratio profile.

Chapter 4 represents the main body of work done by the author which includes presenting and discussing the results of implementing the three lidar analysis techniques. The author has written software (which uses all three lidar analysis techniques) to reconstruct independently the probability of transmission profiles using the lidar's return backscattered signal. The results obtained from these three methods are compared to the lidar manufacturer's closed-source analysis software. Chapter 4 also presents the results of a Mie scattering analysis used to generate an integrated lidar ratio required in the implementation of the Fernald Method. The author has written software that implements a Monte Carlo numer-

ical approach in order to solve for the lidar ratio. Finally, Chapter 4 also presents a model which the author uses in conjunction with the lidar's measurements to reconstruct a vertical profile of the changing lidar ratio. This provides, for the first time, an insight into the aerosol scattering layers present at the H.E.S.S. site in Namibia.

Chapter 5 summarises the main findings of the thesis and also presents the authors recommendations for current and future research work. Chapter 5 recommends that serious consideration should be given to a multi-wavelength Raman or High Spectral Resolution Lidar (HSRL) in order to significantly improve upon the capabilities and accuracy of a single scattering lidar, like that used in this research. Furthermore, Chapter 5 also briefly discusses how the findings of this thesis can be implemented into the H.E.S.S. event reconstruction as well as for the event reconstruction of next generation ground-based gamma ray telescopes like the Cherenkov Telescope Array (CTA).

Chapter 1

Very High Energy Gamma Ray Astronomy

The following chapter introduces the field of Very High Energy Gamma Ray Astronomy (VHEGRA), including the characteristics of cosmic gamma rays. In addition, the different gamma ray interactions will be presented, demonstrating how gamma rays are generated in and propagated across the Universe. The techniques employed to detect gamma rays are discussed with the focus on the Imaging Atmospheric Cherenkov Technique (IACT). Full consideration of electromagnetic and hadronic air showers has been made including an explanation of the generation of Cherenkov radiation. Finally a brief introduction to the H.E.S.S. experiment will be provided, demonstrating gamma ray astronomy in practice.

1.1 Cosmic Rays

In 1912 Victor Hess made a breakthrough in Austria by discovering a strong correlation between increasing altitude and the ionisation of air. These measurements were recorded in a balloon rising to altitudes of approximately 5km. Hess hypothesised that the observed ionisation of air was due to very deeply penetrating radiation from outside of the Earth's atmosphere. In 1936, Hess was awarded the Nobel prize in physics for his discovery of this radiation, later termed cosmic rays [45].

At GeV energies, about 90% of cosmic rays are protons, 9% are helium nuclei (α-particles) and the remaining 1% are electrons (e^-) [24]. The term "cosmic rays" is used to refer to the charged non-thermal radiation incident upon the Earth, i.e. radiation that does not follow a standard black-body spectrum. Cosmic ray measurements illustrate an energy spectrum that follows a power law distribution. Figure 1.1 shows that the cosmic ray spectrum is actually following a broken power law spectrum pivoted around two key features called the "knee" and the "ankle". This suggests that different astrophysical objects are the likely progenitors of cosmic rays. It is generally accepted that galactic Supernova Remnants (SNRs) account for a large amount of the very high energy cosmic rays below the knee. Cosmic rays with energies between the knee and the ankle are assumed to originate from both galactic and extra-galactic sources. Beyond the ankle it is assumed that an extra-galactic component is taking effect and likely source candidates include Active Galactic Nuclei (AGNs).

Cosmic rays are comprised of charged particles and, with the exception of the highest energy cosmic rays, they cannot be traced back to their origins due to

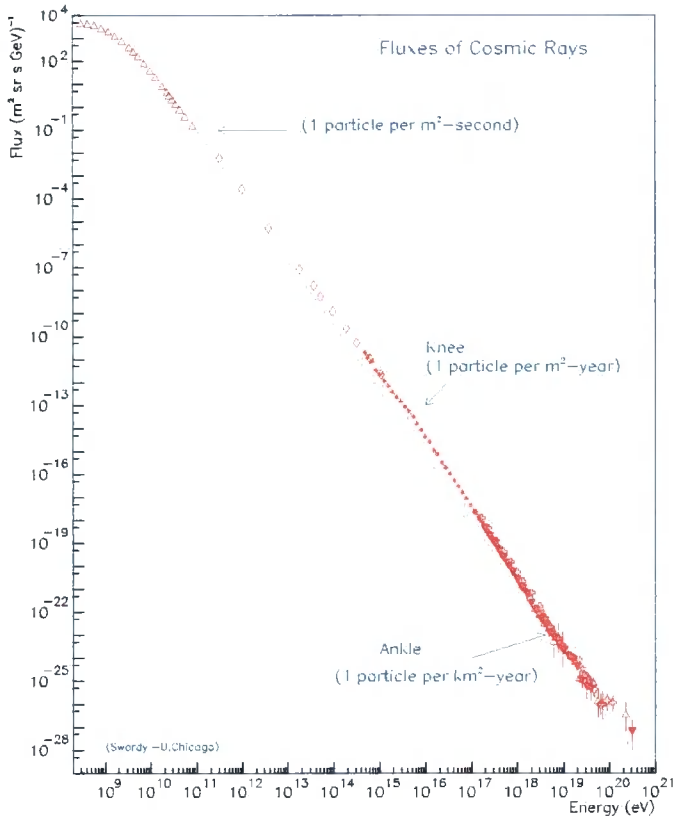

Figure 1.1: The cosmic ray spectrum [51] follows a broken power law the index of which changes at the two highlighted features called the "knee" and the "ankle". It is widely believed that supernova remnants can account for most of the very high energy cosmic rays below the knee. Cosmic rays with energies between the knee and the ankle are assumed to originate from both galactic and extra-galactic sources. Beyond the ankle it is thought that some extragalactic component (for example AGNs) is involved.

the influence of magnetic fields within the Galaxy. As a result of this magnetic field influence cosmic rays follow twisted paths from their point of origin in the universe to their final destination, for example, the Earth.

In contrast to cosmic rays, gamma rays are not charged particles and therefore do not succumb to the influence of magnetic fields. Instead, like other waves in the electromagnetic spectrum, gamma rays travel in straight lines and thus can be traced back to their origins. It is widely accepted that the measurement and analysis of gamma rays can help to pin-point the most likely acceleration sites of cosmic rays. Thus gamma ray astronomy plays an important role in helping to solve the cosmic ray problem.

1.2 Gamma Rays

Gamma rays are the most energetic form of electromagnetic radiation. This thesis considers gamma rays to be electromagnetic radiation with an energy of > 511 keV, the rest mass energy of an electron. The gamma ray energy range can be further sub-divided into different energy bands which are derived from the different techniques implemented to measure gamma rays at these energy values. These energy bands are shown in Table 1.1.

These different energy bands serve as a guide and in practise cross-over between bands occurs. Modern detectors increasingly overlap into the neighbouring bands around their primary energy band of observation. On the 11th June 2008 NASA launched a new gamma ray satellite called the Fermi gamma ray space telescope. NASA claims that Fermi will be able to investigate gamma rays of 30 MeV to

Table 1.1: Gamma Ray Astronomy Categories by Energy [18]

Category Name	Energy Range	Observation Technique
Low/Medium Energy	511 keV - 20 MeV	Satellite Detectors
High Energy	20 MeV - 100 GeV	Satellite Detectors
Very High Energy	100 GeV - 30 TeV	Imaging Atmospheric Cherenkov Telescopes
Ultra High Energy	30 TeV - 30 PeV	Extensive Air Shower Arrays
Extremely High Energy	30 PeV - no limit	Extensive Air Shower Arrays

300 GeV providing complete cross over between the high energy and very high energy bands. However, due to a satellite's small effective area, $\sim$3 m^2 [18] in the case of Fermi, the detection rates obtained within the very high energy band are expected to be very low and it is thus questionable whether any results at these energy values will be statistically significant. Nonetheless, the Fermi results should greatly improve upon existing satellite observations of the gamma-ray sky, and sensible comment regarding its highest energy observations can only be made when the first results from Fermi are published in the near future.

1.3 Creating Gamma Rays

The following section explores the various interactions believed to be responsible for gamma ray production within the universe. Essentially, gamma rays can be produced when electrons (and/or positrons) interact with either matter or radiation fields like the magnetic field of an astrophysical object. In addition, gamma rays can also be produced when hadrons interact with matter or when particles decay. Similarly gamma rays present in the Universe can be attenuated by pair production when a gamma ray interacts with matter or with other photons.

1.3.1 Electromagnetic Interactions

1.3.1.1 Compton Scattering

Compton scattering occurs when a photon scatters off an electron or any other charged particle. This is an inelastic process in which the photon transfers some of its energy to the electron. Equation 1.1 can be used to estimate the change in energy that results when a photon scatters off an electron with mass m_e.

$$\Delta E = \frac{E_{primary} E_{scattered}}{m_e c^2}\Big(1 - cos\theta\Big) \tag{1.1}$$

Figure 1.2 illustrates the Compton scattering process, in which the incident photon's energy loss results in a scattered photon with lower energy and thus lower frequency and longer wavelength.

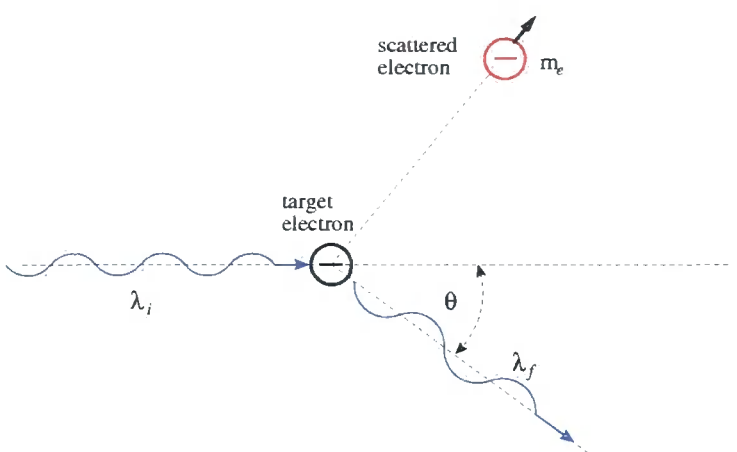

Figure 1.2: Compton scattering as illustrated here occurs when a high energy photon scatters off an electron. During this process the photon transfers some of its energy to the electron, resulting in a scattered photon with lower energy. Adapted from [54].

1.3.1.2 Inverse Compton Scattering

When a relativistic electron collides with a low energy photon, from an ambient field for example, the photon is up-scattered to higher energies. This is a very important gamma ray production mechanism, known as inverse Compton scattering, and is illustrated in Figure 1.3.

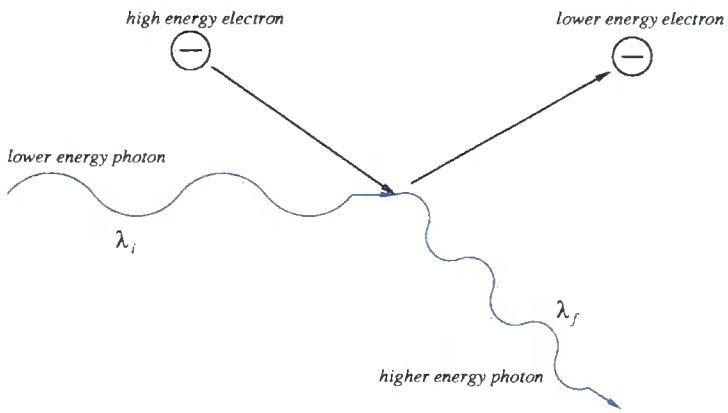

Figure 1.3: Sketch illustrating the basic concept of Inverse Compton scattering. When an electron is accelerated to relativistic speeds and then collides with a low energy photon, the photon is up-scattered to higher energies. This process is very important to very high energy gamma ray astronomy.

1.3.1.3 Synchrotron Radiation

Synchrotron radiation occurs when a relativistic electron is deflected by a magnetic field. An electron travelling non-relativistically in the field radiates electromagnetic waves equally in all directions (cyclotron radiation), whereas a relativistic electron radiates an electromagnetic field forwards in a beamed cone i.e. in the direction of the electron's velocity. Figure 1.4 illustrates this process.

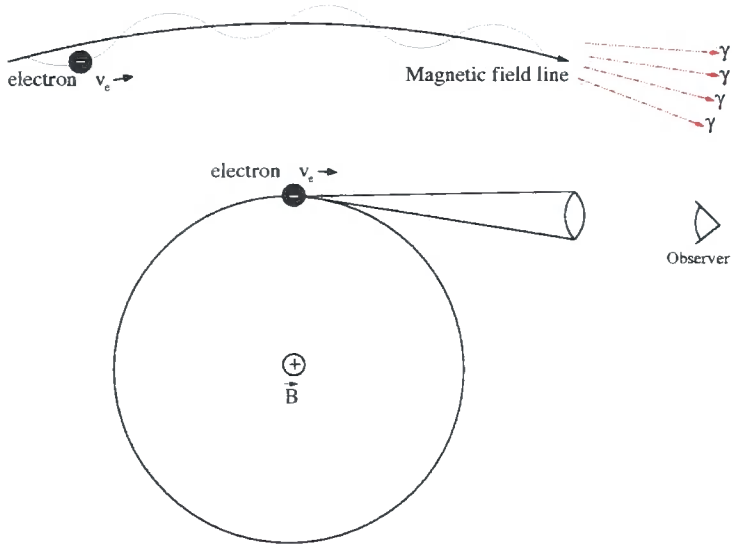

Figure 1.4: Synchrotron radiation illustrated here occurs when a relativistic electron is confined to travel along the magnetic field lines $\vec{B}$ of an object. The electron emits synchrotron radiation which is beamed forward in a cone.

This beaming effect makes synchrotron sources the brightest known x-ray sources in astronomy. It is widely accepted that synchrotron radiation is the main interaction responsible for the production of x-rays. The detection of x-ray sources is possible because synchrotron radiation is highly polarised. When observed on the orbital plane the radiation is linearly polarised and when viewed at a small angle from the orbital plane the radiation is circularly polarised. Another characteristic of synchrotron radiation is the wide range of energies over which it is observed i.e. from radio through to x-rays. Figure 1.5 demonstrates the multi-wavelength emission due to synchrotron radiation.

Sources responsible for synchrotron radiation include active galactic nuclei (AGN),

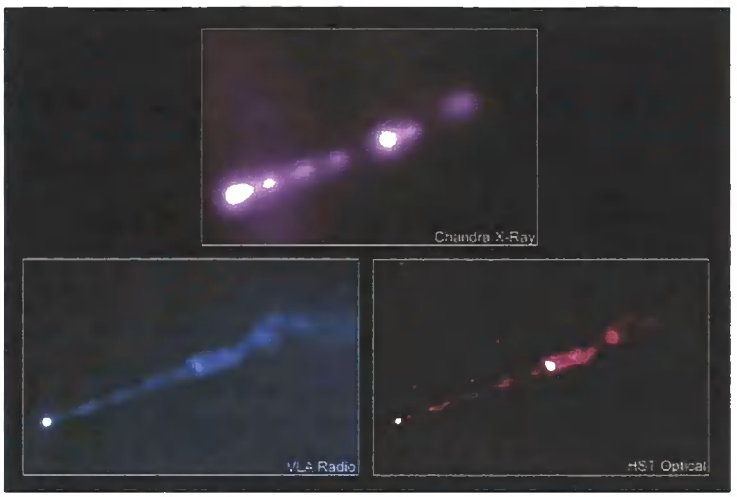

Figure 1.5: An energetic jet from the Virgo cluster elliptical galaxy M87 stretches outward 5000 light years. The image shows the jet in the x-ray, radio and optical bands. In all these bands the observed emission is likely due to synchrotron radiation caused by high energy electrons spiralling along the strong magnetic field lines. [38]

super nova remnants (SNR) and pulsar wind nebulae (PWN). Neutron stars with unusually strong magnetic dipole fields $10^{14} - 10^{15}$ G, sometimes called Magnetars [20], are also a source of synchrotron radiation as particles are accelerated along their very strong magnetic field lines. Sometimes this is referred to as curvature radiation [54].

Synchrotron sources are very important within gamma ray astronomy as they are often an indication of potential very high gamma ray emission sites. These sources are believed to provide the ambient fields or lower energy radiation which is then up-scattered by inverse Compton scattering as is described by the synchrotron self Compton model (SSC). The spectral energy distribution of a gamma source thought to be undergoing emission via the SSC process is illustrated in Figure 1.6.

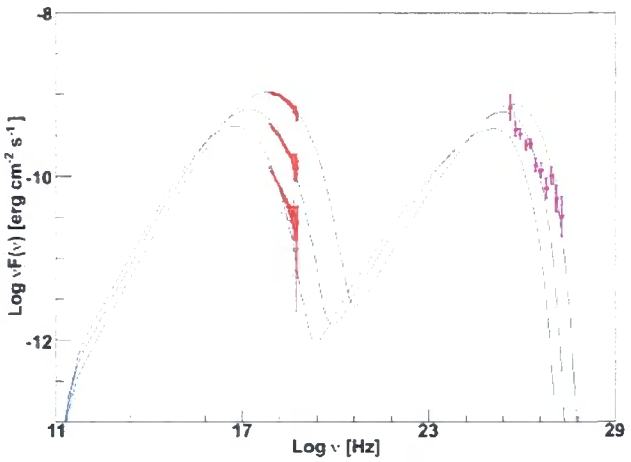

Figure 1.6: Illustrated here is the spectral energy distribution of Mkn421. It is thought that emission from this very high energy gamma ray source is via the SSC process. The first peak is believed to be as a result of synchrotron emission and the second peak due to inverse Compton scattering. [35]

1.3.1.4 Bremsstrahlung

Bremsstrahlung or "braking radiation" occurs when a particle is decelerated or deflected in the strong electric field of an atomic nucleus. In astrophysics this might happen when a relativistic electron moves through a gas or plasma and is decelerated suddenly over a small distance, resulting in an energy loss. Energy is conserved through the emission of radiation whose energy spectrum is dependent on the energy levels of the atomic nuclei as well as the velocity with which the incident electron is travelling. Thus very high energy gamma rays can be emitted when an incident electron is travelling at relativistic speeds, where its kinetic energy is much greater than the rest mass energy of the electron. Figure 1.7 illustrates the Bremsstrahlung interaction process.

In addition to being an interaction process responsible for electron accelerated gamma ray sources, Bremsstrahlung is also the process that produces secondary

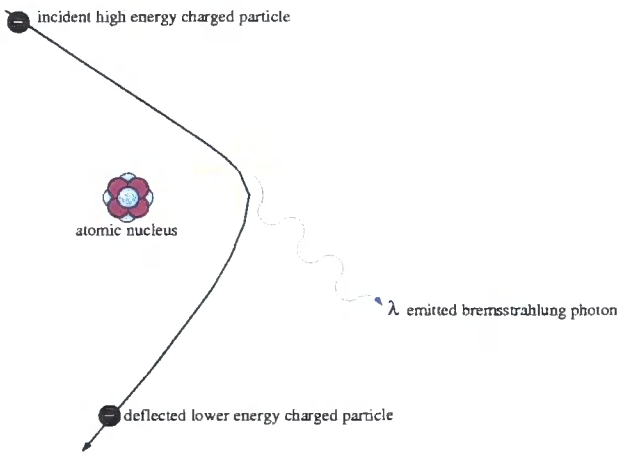

Figure 1.7: Bremsstrahlung Radiation [26] illustrated here occurs when a relativistic electron is decelerated over a very short distance in the strong electric field of an atomic nuclei. The electron loses energy and is deflected during the interaction which also results in the emission of a photon.

photons in electromagnetic air showers. The process and importance of air showers will be discussed later in Section 1.5.1.

1.3.2 Hadronic Interactions

Up until now all of the gamma ray production mechanisms introduced have been as a result of electromagnetic interactions. However, this is not the only production mechanism and gamma rays can also be produced from hadronic interactions. For example, the most common hadronic interaction is that of high energy protons interacting with matter resulting in the production of pions (both charged and neutral), shown in Equation 1.2.

$$p + nucleus \rightarrow p + nucleus + \Pi(\pi^+; \pi^-; \pi^0) \tag{1.2}$$

Pions of all charges are produced in almost equal number except at lower energies

where the π^+ is favoured [36]. Such collisions might occur when protons are accelerated to high energies in the shock fronts of supernova remnants and then interact with the nucleus of the interstellar medium for example. The resulting neutral pion decays into very high energy gamma rays as shown in Equations 1.3 and 1.4.

$$\pi^0 \rightarrow \gamma\gamma \tag{1.3}$$

$$\pi^0 \rightarrow \gamma + e^+ + e^- \tag{1.4}$$

The decay processes shown in Equations 1.3 and 1.4 are not equally likely. It is postulated that this interaction process is responsible for most of the galactic gamma ray production, but this cannot be concluded for certain.

1.3.3 Dark Matter, Particle Decay and Other Interactions

Finally it is also postulated that gamma rays can be produced by more exotic interactions, for instance when dark matter candidates such as Weakly Interacting Massive Particles (WIMPs) self annihilate or decay. Observations of the galactic centre have and continue to be conducted in order to test this theory. However, this is not without difficulty due to other gamma ray sources within this region. So far, evidence for dark matter annihilation at the galactic centre has proved elusive [2]. It is also possible for gamma rays to be produced by nuclear decay.

1.4 The Destruction of Gamma Rays

Up until now this thesis has presented all of the accepted astrophysical gamma ray production mechanisms. This section concentrates on how gamma rays are destroyed or attenuated, therefore these are also the interactions by which gamma rays are detected.

1.4.1 Pair Production $\gamma\gamma$ Interactions

Gamma ray photons can be attenuated through collisions with other photons. The result of such collisions is the production of electron positron pairs, in other words matter is created, when two photons collide as shown in Equation 1.5.

$$\gamma + \gamma \rightarrow e^- + e^+ \tag{1.5}$$

For pair production to occur through photon photon collisions, the following two conditions must be satisfied:

1. Energy must be conserved i.e. The combined energy of the photons must be greater than the rest mass energy of the created particles.
2. Momentum must be conserved.

Thus the threshold energy required for such an interaction to take place is shown in Equation 1.6:

$$E_{threshold} \geq 2m_e c^2 \tag{1.6}$$

where m_e is the rest mass energy of an electron and c is the speed of light. The rest mass energy of an electron is 511 keV, so for pair production the threshold energy must be greater than or equal to 1.022 MeV. This means gamma ray photons are ideal candidates for pair production.

1.4.2 Pair Production γ + Matter Interactions

When gamma rays pass through matter they can interact with atomic nuclei by yielding some of their energy to produce electron positron pairs. Equation 1.7 shows the photon matter interaction and Figure 1.8 illustrates the interaction.

$$\gamma + nucleus \rightarrow e^- + e^+ + nucleus \tag{1.7}$$

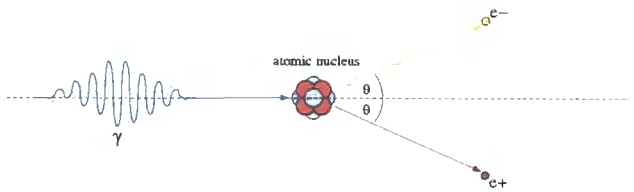

Figure 1.8: Pair Production: The photon + matter interaction illustrated here occurs when a high energy photon collides with the nucleus of an atom. The photon is absorbed resulting in the creation of two symmetrically charged particles, an electron and a positron.

Despite the fact that gamma ray photons can be attenuated when they interact with matter, there is relatively little matter in-between a gamma ray source and the Earth for the emitted gamma ray to interact with. This can be demonstrated by a crude calculation using the gamma ray 'standard candle', the Crab Nebula. The assumed column density of hydrogen in the path of the Crab Nebula is 10^{21} atoms cm^{-2} [49] [31]. Approximately 40% of the interstellar medium is

comprised of neutral hydrogen (HI) regions [11], therefore it is reasonable to assume that neutral hydrogen is the most likely form of matter that a gamma ray from the Crab could interact with on its path toward Earth. Multiplying the mass of a proton with the column density finds the column mass density in the direction of the Crab Nebula.

An approximate radiation length can be calculated using Equation 1.8 [25] where A is the mass number and Z the atomic number.

$$\chi_0 = \frac{716.4[\text{g cm}^{-2}]A}{Z(Z+1)ln(\frac{287}{\sqrt{Z}})}\ [\text{g cm}^{-2}] \tag{1.8}$$

Substituting in Z=1 and A=1 for neutral hydrogen the radiation length calculated is $\chi_{H1} \approx 63\ \text{g cm}^{-2}$. Thus along the path of a gamma ray photon from the Crab Nebula there are $\frac{1.67 \times 10^{-3}\ \text{g cm}^{-2}}{63\ \text{g cm}^{-2}} \approx 3 \times 10^{-5}$ radiation lengths. This is $\ll 1$, meaning that there is very little probability of the photon interacting with any of the matter in its path. However, this is not the case when a gamma ray enters a medium such as the Earth's atmosphere. In order to determine to what depth a gamma ray can penetrate the Earth's atmosphere, we make a similar crude calculation using the radiation lengths. The radiation length for photons in air is approximately $\chi_{air} \approx 36.66\ \text{g cm}^{-2}$ [25] whereas the column density (or total thickness) of the Earth's atmosphere is roughly $1000\ \text{g cm}^{-2}$. Therefore the total atmosphere corresponds to approximately $\frac{1000\ \text{g cm}^{-2}}{36.66\ \text{g cm}^{-2}} = 27$ radiation lengths. This means that no primary gamma ray photon is ever likely to arrive at the Earth's surface. Instead, a gamma ray incident on the Earth will interact with atmospheric nuclei resulting in pair production, which ultimately results in

electromagnetic air showers.

1.5 Gamma Ray Detection

The following section will discuss how very high energy gamma rays can be detected both from the surface of the Earth and from satellites. Gamma rays can only be detected indirectly by the products of the interactions discussed in Section 1.4. Furthermore, when gamma rays enter the Earth's atmosphere, as has already been mentioned, they interact with it. Therefore it would be preferable to conduct gamma ray detection experiments outside the atmosphere. Unfortunately conducting experiments outside the Earth's atmosphere is not trivial, comes at great expense and is limited by instrumentation constraints. For example, the Fermi gamma ray space telescope cost a total of $ 690 million [12].

In addition to the high cost, satellite detectors need to be small, therefore placing constraints on the instrumentation. For example, the Fermi satellite is only 2.8 metres high with a diameter of 2.5 metres. Therefore Fermi has a very small effective area, constraining the detectable gamma ray fluxes. Fermi has a very large field of view ($>$ 2 steradians) allowing for observation of a large proportion of the visible sky.

From the ground it is possible to detect gamma rays indirectly by observing the secondary air showers that are produced when gamma rays incident on the Earth's atmosphere interact with it through pair production. The resulting secondary air showers also interact with the atmosphere, causing a cascade effect which results in the production of Cherenkov radiation, which is discussed in Section 1.5.2.

Using reflecting telescopes, it is possible to focus the very faint Cherenkov radiation onto high speed cameras in order to image the progression of the air shower through the atmosphere. This method of ground-based gamma ray detection is widely referred to as the Imaging Atmospheric Cherenkov technique (IACT) and is the technique implemented by the H.E.S.S. experiment in Namibia. H.E.S.S. is not the only active IACT experiment; others include the Major Atmospheric Gamma-ray Imaging Cherenkov (MAGIC) [37] telescope located in the Canary Islands, the Very Energetic Radiation Imaging Telescope Array System (VERITAS) [52] in the United States and the Collaboration between Australia and Nippon for a Gamma Ray Observatory in the Outback (CANGAROO) [14] in Australia. A brief overview of the H.E.S.S. experiment is provided in Section 1.7.

1.5.1 Extensive Air Showers

When cosmic rays enter the Earth's atmosphere they interact with atmospheric matter, producing a cascade of secondary particles that propagate down towards the Earth. The following sections present the two types of extensive air showers (EAS) relevant to very high energy gamma ray astronomy.

1.5.1.1 Gamma Ray Air Showers

Very high energy gamma rays entering the Earth's atmosphere can initiate an air shower by pair production. For the cascade to continue, the resulting electron positron pairs need an energy > 20 MeV. Gamma ray air showers occur at an altitude of approximately 10 km. However, the greater the energy of the primary gamma ray photon, the closer to the ground the air showers can propagate and

the greater the intensity of the Cherenkov light produced. Figure 1.9 illustrates a typical air shower model.

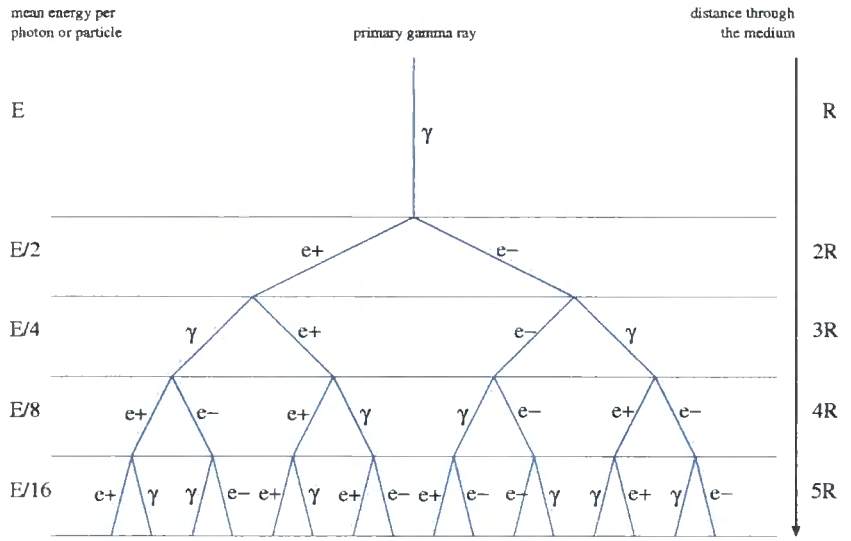

Figure 1.9: A gamma ray induced electromagnetic air shower. A simple model adapted from Longair[36]

The pair-produced electrons and positrons generate additional gamma ray photons through Bremsstrahlung as they are deflected by the atmospheric atomic nuclei as explained in Section 1.3.1.4. However, in order to generate additional gamma ray photons in the atmosphere via Bremstrahlung the electrons and positrons need an energy approximately > 84 MeV. This is known as the critical energy of air, and is the the energy at which energy loss by ionization and Bremsstrahlung are equal [25].

1.5.1.2 Hadronic Air Showers

Hadronic air showers occur when a high energy proton or other heavy nucleus such as iron enters the Earth's atmosphere and interacts with atmospheric mat-

ter. Traditionally cascades, initiated by hadronic interactions, have been called cosmic ray air showers and are the dominant type of air showers (around 1000 hadronic to every 1 gamma ray induced air shower) occurring in the Earth's atmosphere. Hadronic air showers are far more complicated than gamma ray induced air showers as they produce many more types of secondary particle. Figure 1.10 illustrates an example of the types of secondary particles produced in hadronic air showers compared to gamma ray induced air showers, which are purely electromagnetic.

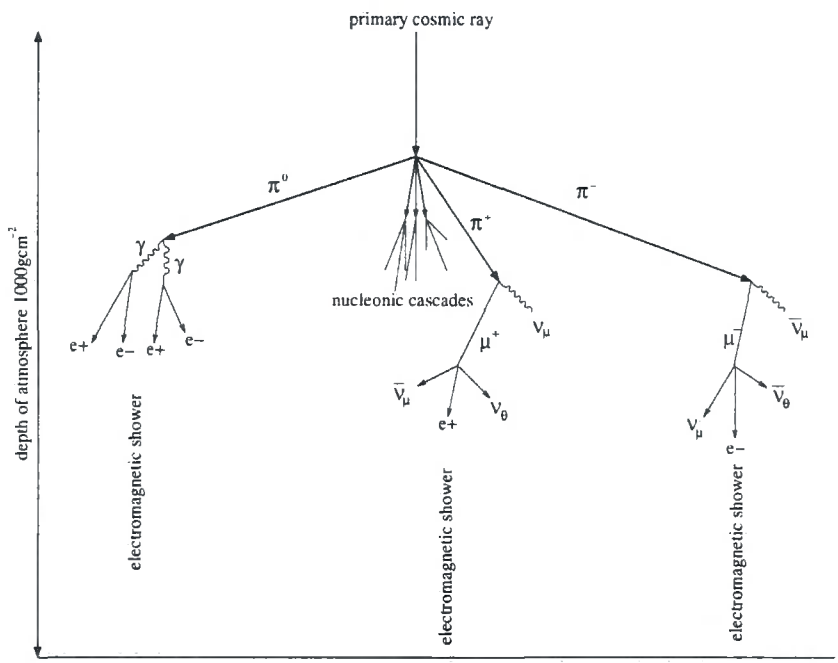

Figure 1.10: A cosmic ray induced air shower decays into many more secondary particles including electromagnetic air shower particles. A simple model adapted from Longair[36]

As Figure 1.10 shows, hadronic interactions produce charged $\pi^{\pm}$ and neutral π^0 pions. Earlier in Section 1.3.2 it was shown that neutral pions decay into two gammas ($\pi^0 \rightarrow \gamma\gamma$) which can subsequently pair produce. This implies that

cosmic rays are responsible for most of the electromagnetic pair production air showers in the atmosphere and thus being able to distinguish between gamma-ray-induced electromagnetic air showers and cosmic-ray-induced electromagnetic air showers is very important in very high energy gamma ray astronomy from the ground. Fortunately pions are produced with a large scattering angle compared to that of gamma rays, whose secondary air shower particles scatter relatively closely to the original gamma ray path. This makes it relatively easy to distinguish between the gamma-ray-induced air showers and the hadronic air showers as will be seen in Section 4.2.2.1, following.

1.5.1.3 Cosmic Ray Background

Hadronic interactions are treated as a background noise encountered by ground-based gamma-ray detectors as well as by space-based gamma-ray detectors. This background is commonly referred to as the cosmic ray background and in high energy gamma ray astronomy this background needs to be distinguished from 'real' gamma ray detections. An anti-coincidence shield helps to block out the cosmic ray background encountered on space-based detectors, and for ground-based detectors it is the air shower characteristics that help to distinguish between gamma-ray-induced air showers and the cosmic ray background. The air shower properties are as follows:

- hadronic air showers are spread over a larger area than gamma ray showers due to the bigger opening angle from pion decay.
- the morphology of hadronic air showers is irregular compared to gamma ray induced air showers.

- the intensity of Cherenkov light produced in a gamma ray air shower is much greater than that from a hadronic air shower of similar primary energy.

Figure 1.11 illustrates the differences between gamma ray and hadronic Cherenkov radiation by comparing a simulated hadronic air shower induced by an incident proton to that of an electromagnetic air shower induced by a gamma ray.

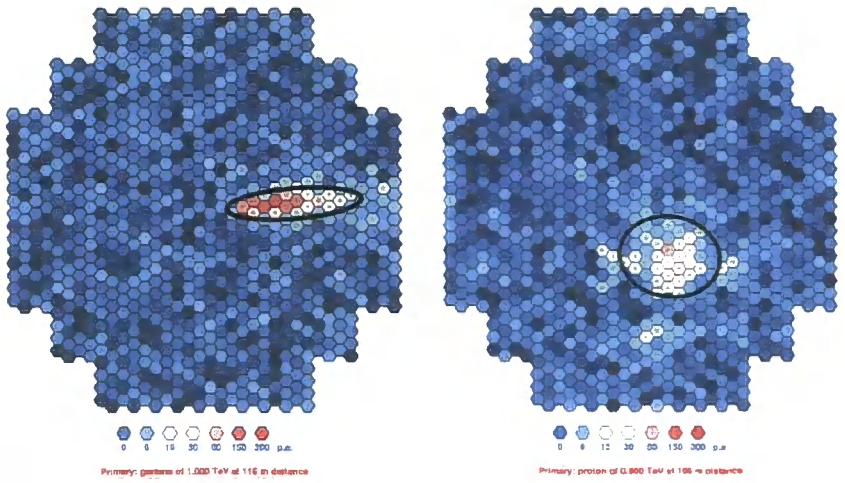

Figure 1.11: Illustrated here is a simulated view of a gamma ray (left) and hadronic (right) air shower as seen by the H.E.S.S. ground-based Cherenkov imaging cameras. The gamma ray source is at the centre of the camera and has a primary energy of 1 TeV whereas the hadronic shower has a primary energy of 0.8 TeV. The different morphology of the air showers makes it relatively easy to distinguish between the two. The gamma ray (left) has an elliptical shape that points toward the source at the centre of the camera, however the hadronic air shower (right) is more dispersed with no certain direction. Image courtesy of Dr.K.Bernlöhr and H.Dickinson: Private Communication.

Cosmic rays electrons incident upon the Earth's atmosphere can also induce electromagnetic air showers which are indistinguishable from those induced by gamma rays. Electrons are strongly influenced by the Sun and the Earth's magnetic fields due to their much lighter mass compared to protons. Only at energies above 10 GeV are electrons free from the effects of the Sun and the Earth's magnetic fields

[36]. Fortunately the flux of such high energy electrons incident on the Earth is low and, for ground-based experiments like H.E.S.S. currently exploring energies above $\approx$ 100 GeV, these electrons can be ignored.

1.5.2 Cherenkov Radiation

When a particle moves through a medium faster than the phase velocity of light in that medium then Cherenkov radiation is emitted. The phase velocity c_n of light in a medium is equal to the speed of light c divided by the refractive index n of the medium the light passes through, as shown in Equation 1.9.

$$c_n = \frac{c}{n} \tag{1.9}$$

For example, if it is assumed that the refractive index of air is approximately n = 1.0003, then a particle moving through the atmosphere with a velocity greater or equal to $299,702,547.2 \text{ m s}^{-1}$ will emit Cherenkov radiation. The energy threshold for emission of Cherenkov radiation is mass-dependent. For example, an electron will emit Cherenkov radiation if its kinetic energy is $\approx >$ 20 MeV.

Figure 1.12 illustrates Huygen's simple geometric construction of Cherenkov radiation, useful for determining the direction of propagation of the Cherenkov radiation wavefront. When a charged particle like an electron travels through a medium like air at a velocity v greater than the phase velocity of light in air then Cherenkov radiation is emitted. As Figure 1.12 shows, a shockwave forms behind the relativistic particle which ultimately results in the particle losing energy.

The Cherenkov radiation emitted propagates outward at a fixed angle from the

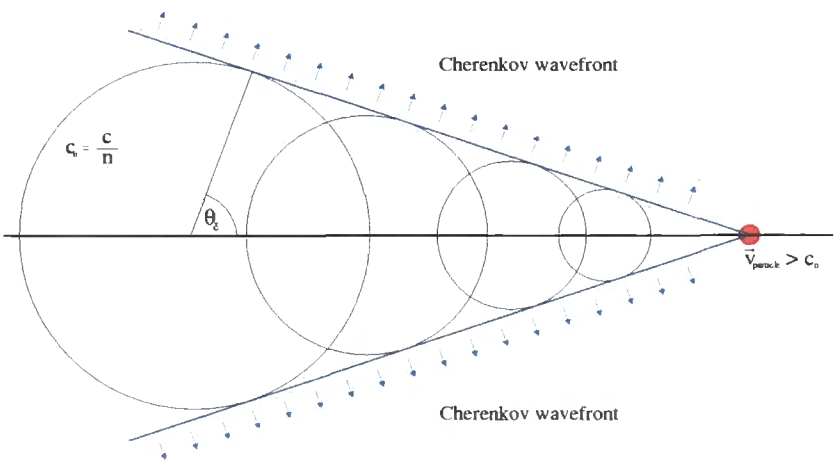

Figure 1.12: The Huygen's construction for determining the direction of propagation of Cherenkov radiation. If a particle travels through a medium with velocity v greater than the phase velocity c_n of light within that medium, then Cherenkov radiation will be emitted. The Huygen's construction illustrates the shockwave that forms behind the relativistic particle and which ultimately results in the particle losing energy. The resulting Cherenkov radiation wavefront propagates outward at a fixed angle from the velocity vector of the particle, and is referred to as the Cherenkov opening angle ($\theta_{\check{c}}$). Image adapted from [36].

velocity vector of the particle, referred to as the Cherenkov opening angle ($\theta_{\check{c}}$) shown in Equation 1.10.

$$\theta_{\check{C}} = \arccos(\frac{1}{n\beta}) \tag{1.10}$$

where $\beta = \frac{v}{c}$ and typical opening angles in the atmosphere range between 1 and 2 degrees. An opening angle of this magnitude relates to a ground surface area of $\sim 45000\ \mathrm{m}^2$ which represents a radius of $\pm 120\ \mathrm{m}$. Figure 1.13 illustrates a typical gamma ray shower of roughly 1 TeV energy, emphasising the Cherenkov opening angle and ground surface area. Furthermore, the small opening angles expected for gamma ray showers illustrate the point made in Section 1.5.1.2, that gamma ray showers are focused around the primary gamma ray's original path.

It is possible to estimate the number of Cherenkov photons per unit path length $(\frac{dN}{dx})$ generated between wavelengths λ_1 and λ_2 arriving at the ground using Equation 1.11 [9]. This is constrained to the particular wavelength of interest, which in the case of Cherenkov radiation is in the region of 320 nm:

$$\frac{dN}{dx} = 2\pi\alpha z^2 \int_{\lambda_1}^{\lambda_2} \Big(1 - (\frac{c}{vn(\lambda)})^2 \frac{1}{\lambda^2}\Big) d\lambda \tag{1.11}$$

where $\alpha \approx \frac{1}{137}$ is the fine structure constant and z is the charge of the particle. From Equation 1.11 it can be seen that the refractive index affects the number of Cherenkov photons arriving at the surface of the Earth; similarly from Equation 1.10 the refractive index affects the Cherenkov opening angle. This implies that monitoring and analysis of the atmosphere at the H.E.S.S. site in Namibia is of

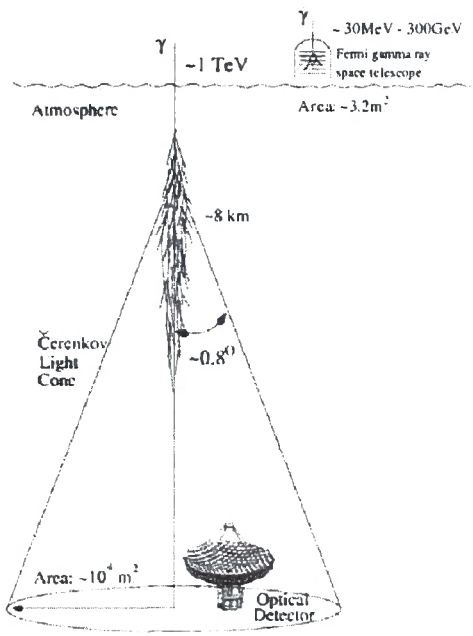

Figure 1.13: Illustrated here are two techniques used for detecting gamma rays including the imaging atmospheric Cherenkov technique for ground-based observations, and the Fermi satellite detector for space-based observations. In this example the gamma ray induced air shower occurs at a height of approximately 8 km and the Cherenkov radiation wavefront propagates toward the ground at an opening angle of $\approx 0.8°$. The Cherenkov radiation emitted from the air shower results in a light pool on the ground spread over an area of $\approx 10^4$ m^2. Image adapted from Badran & Horan [5].

paramount importance in order to accurately calibrate the imaging atmospheric Cherenkov telescopes.

1.6 IACT Atmospheric Parameters

Chapter 1 has presented the main principles of gamma ray astronomy and the Imaging Atmospheric Cherenkov Technique (IACT). From this the following observations can be summarised:

- the energy of a primary gamma ray photon constrains how far into the atmosphere the photon can penetrate before interacting with atmospheric matter to produce secondary particles;
- likewise, the primary energy constrains the number of the secondary particles produced, which can be used to estimate the total amount of Cherenkov radiation emitted;
- however, the total amount of Cherenkov radiation readily available for collecting at ground level is also strongly dependent on various atmospheric parameters like the refractive index.

Therefore the challenge faced by very high energy gamma ray astronomy experiments employing the imaging atmospheric Cherenkov technique is to monitor the atmosphere accurately in order to improve the inferred Cherenkov radiation intensities. Doing so will then improve the inferred primary gamma ray energy estimates.

Bernlöhr [9] highlights various atmospheric parameters that can be investigated in order to improve energy calibration of the imaging atmospheric Cherenkov technique including:

- vertical atmospheric profiles;
- the transmission, refraction and scattering of Cherenkov radiation;
- the importance of spherical versus plane parallel geometry used for simulating air-showers.

The first two parameters above will be addressed in Chapter 2. For further information on the importance of spherical versus plane parallel geometry then further investigation of [9] is recommended.

1.7 The H.E.S.S. Experiment

The High Energy Stereoscopic System (H.E.S.S.) is an array of imaging atmospheric Cherenkov telescopes located in Namibia (23°16′18"S, 16°30′00"E). The telescopes observe in the very high energy range, from approximately 100 GeV to 100 TeV. The array consists of four 12 m diameter reflector telescopes with an focal length of 15 m. The mirror facets are arranged in a Davis-Cotton design [16] providing good imaging of "off-axis" air showers. Each dish has 382 round mirror facets of 60 cm each. They are all individually adjustable by remotely controlled motors.

The H.E.S.S. cameras have a 5 degree field of view and are comprised of 960 photon detector elements or pixels. Each pixel has a photo-multiplier tube (PMT)

that captures the reflected Cherenkov radiation. The PMT signals are sampled on nanosecond timescales allowing the system to process images extremely rapidly.

The array is set-up geometrically as a square with a telescope at each of the corners. The distance between each telescope is 120m which allows stereoscopic imaging of air showers. The separation distance between each of the telescopes ensures that all four of the telescopes are within the Cherenkov light pool which is estimated to be approximately 250 m in diameter. The diagonal of the square is aligned North to South.

As a location for astronomy, the Gamsberg region of Namibia allows for the observation of the Galactic Plane and the centre of the Galaxy itself. Since the inception of H.E.S.S. in 2003 the number of known gamma-ray sources has increased from about 20 to 73 published sources as at 26 October 2008 [53]. Thus H.E.S.S. has made a significant contribution towards better understanding of the most violent phenomena in the Universe and more specifically the Galactic Plane [28].

Figure 1.14 is an aerial image of the H.E.S.S. site in Namibia illustrating the layout of the telescope array.

Figure 1.14: The H.E.S.S. site in the Gamsberg region of Namibia illustrating the square layout of the telescopes. The location of the lidar used for atmospheric monitoring is also highlighted on this map.

Chapter 2

The Atmosphere

The previous chapter introduced the fundamental physics associated with the imaging atmospheric Cherenkov technique. This chapter builds upon what was presented in Chapter 1 by discussing the atmospheric parameters important to the imaging atmospheric Cherenkov technique. To begin with, the chapter presents the basic structure and composition of the atmosphere. This is then followed by the introduction of atmospheric models widely used in atmospheric analysis. The theory of light absorption and scattering is discussed, including the concept of extinction by a cloud of many particles. This leads to the presentation of Rayleigh and Mie scattering theory including the formalisation of important atmospheric quantities like optical depth and transmission. Techniques for monitoring the atmosphere are briefly discussed focusing on the lidar remote sensing technique, which is one of the methods employed at the H.E.S.S. site in Namibia. Finally, the local atmospheric conditions and assumptions for the H.E.S.S. site are presented and discussed.

2.1 Structure and Composition

Chapter 1 outlined the importance of the atmosphere to the IACT and it is generally accepted that the atmosphere forms part of the detector. Although the IACT doesn't suffer from the high costs and constraints of satellite gamma ray detectors, the technique still faces a challenge because the atmosphere is a complex and variable medium that presents a range of physical problems for consideration.

The atmosphere can be imagined as a layered mass (see Figure 2.1) of mixed gases including nitrogen (78% by volume), oxygen (21%) and trace gases (1%) like neon, helium, hydrogen, methane and carbon dioxide [46]. In addition to these molecular gases, the atmosphere is also composed of a few suspended solids and liquids like dust, ice and salt. These suspended substances are widely referred to as aerosols. The degree to which these are present is influenced by two primary factors. First, the local environment where any particular atmospheric measurement is made; for example the salt content will be much higher for measurements taken over the Pacific Ocean compared to those taken over the Sahara Desert. Secondly, the motion or trajectory paths of the atmosphere itself; for example measurements taken nearby, but not necessarily, in a desert might contain a very high percentage of dust if the measurement site lies downwind from the desert. Therefore, winds create a large scale mixing process that influences local atmospheric composition.

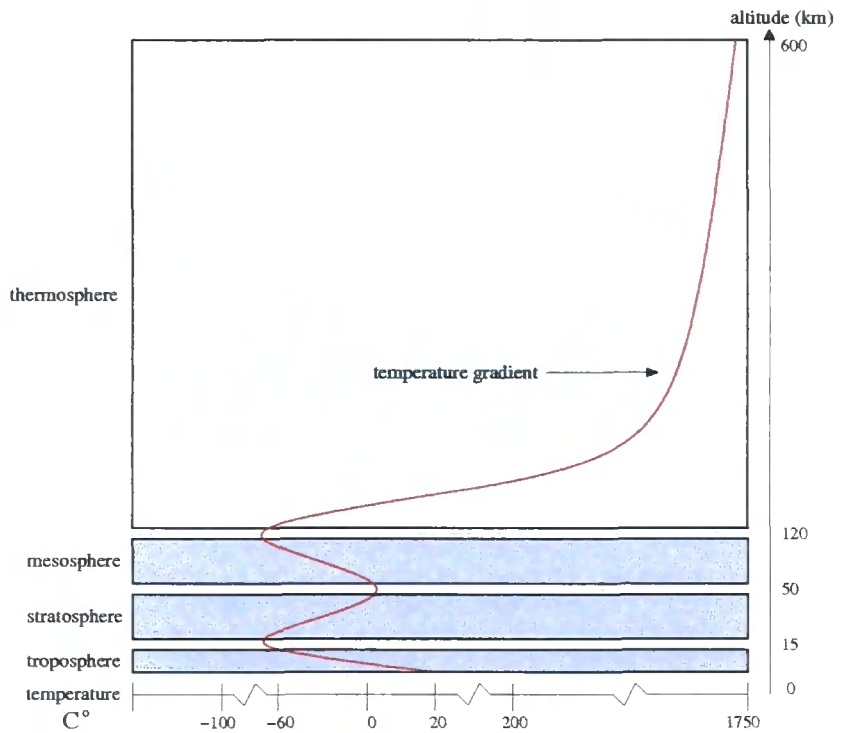

Figure 2.1: The Earth's atmosphere divided into a set of layers. In reality the layers are continuous and not separated as is shown in this figure. The layered concept was conceived as a result of the Earth's temperature gradient which is also shown here. Smaller intermediary layers called 'pauses', such as the mesopause, are sometimes referred to by atmospheric scientists, but these are not important for this work.

2.1.1 Pressure, Mass and Density

Relative to its radius, the height of the Earth's atmosphere is approximately 2%. Thus the atmosphere can be seen as a very thin layer of air enveloping the planet. The atmosphere is bound to the Earth by gravity, and the atmospheric pressure recorded at a height (z) is a measure of the mass of air above that height [46]. Atmospheric mass decreases with increasing height and hence so does atmospheric pressure. For example, it is estimated that only about 1% of atmospheric mass lies above an altitude of 30 km [30]. Similarly, because the mass of the atmosphere decreases with altitude, it follows that the density of atmospheric molecules contributing towards the mass also decreases with altitude.

2.1.2 Temperature

The Sun is more efficient at heating up the surface of the Earth than at heating up the atmosphere. The lower part of the atmosphere is heated by radiative and convective processes caused by the Earth's heated surface. Within the troposphere the temperature decreases with altitude up to the stratosphere. All of the weather experienced on the surface of the Earth such as rain clouds, for example, occur in the upper part of the troposphere. Above the troposphere is the stratosphere which is sometimes referred to as the "inversion layer" because the atmospheric temperature begins to increase with altitude in this layer. The reason this occurs is due to the presence of ozone (O_3) gas in this layer. The ozone gas absorbs most of the ultraviolet radiation incident on the Earth from the Sun, and some of this energy is re-emitted by the ozone gas back into the atmosphere in the form of heat. Above the stratosphere is the mesosphere where

once again, due to the lack of ozone gas, the temperature decreases with altitude until the thermosphere is reached, where the atmospheric density is so low that temperature once again rises rapidly as there are no more atmospheric gases to absorb the intense radiation from the Sun.

2.2 Modelling the Atmosphere

The atmosphere has been modelled by various agencies; for example the United States Committee on Extension to the Standard Atmosphere published the U.S. Standard Atmosphere model back in 1958 [10]. Since then this particular model has had many updates, with the most recent published in 1976. Similarly, the International Organisation for Standardisation (ISO), published the International Standard Atmosphere (ISO 2533:1975) in 1975. The purpose of these model atmospheres is to describe how the properties of the atmosphere change as a function of height. Specifically, the atmosphere is treated as an ideal gas and as such model atmospheres try to describe how the properties of an ideal gas change with respect to height. An ideal gas can be described by using the following properties, most of which were introduced in Section 2.1:

- pressure (P);
- temperature (T);
- density (ρ);
- molecular weight (M).

For convenience it is useful to classify atmospheric models that describe the above properties as molecular atmospheric models. However, the Earth's atmosphere is not a pure molecular atmosphere. Section 2.1 briefly mentioned that, in addition to the molecular gases, the composition of local atmospheres is influenced by the local environment such as natural factors (e.g. oceans and deserts) as well as human activity, for example urbanisation and agriculture. Each of these factors results in the atmosphere becoming contaminated with a different mixture of aerosols whose characteristics can be described by radius, refractive index and size distribution. Atmospheric models that describe these properties can be defined as aerosol atmospheric models.

These models are very useful tools for conducting atmospheric analysis. However it is important to remember that the atmosphere is a dynamic medium and variability occurs in both time and space. Thus atmospheric models only provide a reference point to the macro atmosphere. In order to improve atmospheric analysis the preferred approach is to collect detailed data at the site of interest which can be compared against atmospheric models.

All of these atmospheric models described above are widely used with a computer program known as MODTRAN (MODerate Resolution Atmospheric TRANsmission). The purpose of this software is to model the propagation of electromagnetic radiation in the atmosphere and is used by H.E.S.S. for atmospheric analysis. It is also used in other disciplines including atmospheric sciences and aeronautical engineering. The use of MODTRAN requires a license and for further information regarding the program including its capabilities and uses, investigation of the MODTRAN user manual is recommended. [29].

For very high energy gamma ray astronomy employing the Imaging Atmospheric Cherenkov technique, MODTRAN provides optical depth simulations for the effects of both the molecular and aerosol components of the atmosphere.

2.2.1 Molecular Atmospheric Models

The most widely accepted molecular atmospheric models and those which are used by MODTRAN include:

- U.S. Standard Atmosphere (1976);
- Mid-latitude Summer;
- Mid-latitude Winter;
- Subarctic Summer;
- Subarctic Winter;
- Tropical.

Further information on the details and specifications of each of these model atmospheres can be found in the MODTRAN user manual [29]. The molecular atmospheric model used by H.E.S.S. is the tropical model which will be discussed later in Section 2.5.

2.2.2 Aerosol Atmospheric Models

The most widely accepted aerosol atmospheric models and those which are used by MODTRAN include:

- Continental;
- Desert Dust;
- Maritime.

The properties and characteristics describing each of these models is detailed in Hess et al [27]. In MODTRAN it is possible to alter the wind speed from $0\ \mathrm{m\ s^{-1}}$ to $30\ \mathrm{m\ s^{-1}}$, the result of which increases the concentration of aerosols in the planetary boundary layer (PBL)[1]. The aerosol model used by H.E.S.S. is the Desert Dust model which is discussed later in Section 2.5

2.3 The Scattering and Absorption of Light

In Section 1.5.2 it was established that the amount of Cherenkov light detected by the H.E.S.S. telescopes was fundamental to the success of the Imaging Atmospheric Cherenkov technique. Some of the Cherenkov light produced in air showers will not reach the telescopes on the ground due to absorption and scattering as a result of the Cherenkov photons interacting with both the molecular and aerosol components of the atmosphere. Thus in order to account for the amount of Cherenkov light that is not collected by the telescopes it is important to understand the principles of absorption and scattering theory. This section discusses in detail the theory of absorption and scattering of light in a medium.

[1]The lower 2 km of the atmosphere is widely referred to as the planetary boundary layer. The actual height of the layer varies locally and this region of the atmosphere takes significance within atmospheric analysis because this is the region where the majority of atmospheric aerosols reside.

2.3.1 Basic Theory of Scattering and Absorption

To understand the effects of absorption, scattering and transmission it is important to understand what happens when an electromagnetic wave such as a laser beam encounters an obstacle in its path. Matter in the atmosphere is made up of atoms whose own particles comprise discrete charges, like electrons (-) and protons (+). When an electromagnetic wave interacts with these charges, the electric field of the electromagnetic wave sets these charged particles in motion. The result of this is that secondary radiation is created as the charged particles are accelerated, emitting radiation in all directions. This secondary radiation can be referred to as scattering. In addition, it is not unusual for the incident electromagnetic energy to be transformed into a different form of radiant energy by these moving charges. The most basic example of this energy transformation is heat or thermal energy and this is referred to as absorption.

Any scattering target with a positive refractive index has the ability to scatter incident electromagnetic waves. This includes transparent media such as water, ice and gases. The refractive index m can be described by a complex number:

$$m = n + ik \tag{2.1}$$

where the imaginary part determines the attenuation of the wave propagating through the medium and the real part determines the phase velocity ($v_{phase} = \frac{c}{n}$) of the wave.

Scattering and absorption both remove energy from an electromagnetic wave that propagates through a medium and this process is often referred to as at-

tenuation. When an electromagnetic wave propagates through the atmosphere this attenuation is called extinction, and for the purposes of this thesis, extinction refers to scattering plus absorption i.e. the overall effect of both scattering and absorption by a particle, either molecular or aerosol. Similarly the scattering addressed in this section and all future sections refers only to elastic scattering, i.e. the scattered wavelength of radiation is the same as the incident wavelength. Any change of wavelength implies a quantum mechanical effect which is not addressed in this thesis. An example of this includes the inelastic scattering process known as Raman scattering, and for more information about this process see [48].

2.3.2 Conservation of Energy

For energy to be conserved the sum of the total energy scattered in all directions plus the total energy absorbed by a particle must be equal to the total energy incident on that particle. The effective area of the particle upon which the incident energy strikes is widely referred to as the cross section (C). In accordance with the law of energy conservation the extinction cross section can be defined as [17]:

$$C_{ext} = C_{scat} + C_{abs} \tag{2.2}$$

This implies that in situations where extinction results only from elastic scattering, the extinction cross section is equal to the scattering cross section i.e. no absorption occurs and hence $C_{ext} = C_{scat}$.

2.3.3 Efficiency Factors

Using the cross sections of a particle, both Van de Hulst [17] and Bohren & Huffman [13] define efficiency factors by dividing the cross section by the particle's geometric cross section (G). The most widely used geometric cross section is a sphere, and thus $G = \pi r^2$ where r is the sphere radius. By dividing the respective cross sections of the particle by its geometric cross section it is possible to define the particle's efficiency factor for scattering, absorption and extinction:

$$Q_{ext} = \frac{C_{ext}}{G}, Q_{scat} = \frac{C_{scat}}{G}, Q_{abs} = \frac{C_{abs}}{G} \tag{2.3}$$

Efficiency factors are simply dimensionless cross section ratios that are strongly dependent on particle orientation (if the particle is asymmetric) and the polarisation of the incident electromagnetic wave. This thesis will only consider the special case of a sphere where the efficiency factors are independent of both polarisation and orientation. Thus all findings and results presented in this thesis provide a good first order approximation of the extinction problem, but are not intended to be conclusive. Scattering by non-spherical particles is a very complex problem that has been addressed by various authors including Mishchenko et al [40].

2.3.4 Extinction by a Cloud of Many Particles

So far this Chapter has only discussed the effects of scattering by a single particle. In practice, the atmosphere is not comprised of a single particle. Instead, it can be seen as a cloud of many particles; this is true for both atmospheric molecules and

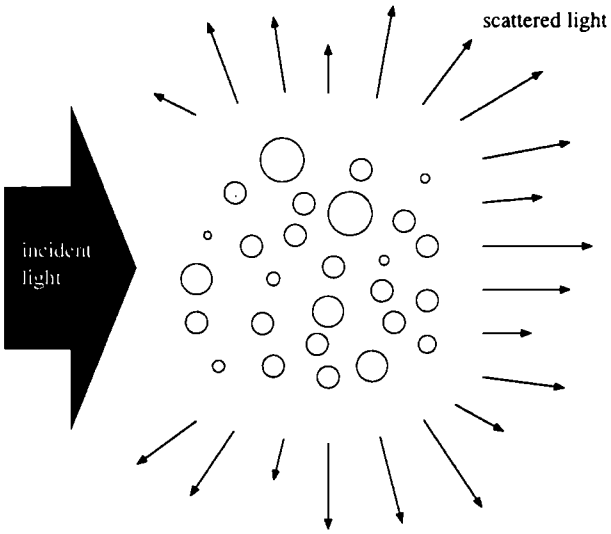

Figure 2.2: Aerosol extinction due to a cloud of many particles where the particles are all spherical, have different radii but share the same optical properties. Adapted from Bohren & Huffman [13]

aerosols. Thus, in applications that aim to solve for extinction due to aerosols, it is very useful to consider the cloud being comprised of spherical particles that have the same composition but different sizes. In others words the particles all share the same optical properties but each has a different radius. Figure 2.2 illustrates the concept of extinction due to a homogeneous cloud of many aerosol particles.

By using the 'cloud of spherical particles' approach in atmospheric analysis it is possible to define the extinction coefficient, which is simply the total cross section per unit volume:

$$\alpha(r) = \pi r^2 \int Q_{ext}(r, \lambda, m) n(r) dr \tag{2.4}$$

where m is the complex refractive index of the particle, λ is the wavelength of the

incident electromagnetic radiation, r is the particle radius, $n(r)$ is the number density of the particles and Q_{ext} is the extinction efficiency factor.

For convenience the extinction coefficient can be thought of as an inverse attenuation length. In other words it represents the average distance travelled between interactions of electromagnetic radiation and the medium it is traversing. In practice, the extinction coefficient is a measure of how much a beam of light is absorbed into the atmosphere for example.

2.3.5 Rayleigh and Mie Scattering

Rayleigh scattering of light by particles occurs when the particles are small compared to the wavelength of the incident electromagnetic radiation. Furthermore Rayleigh scattering describes the elastic scattering of the incident electromagnetic waves which was introduced in Section 2.3.1. Rayleigh scattering is common in the atmosphere and examples include the scattering of sunlight by atmospheric nuclei. Thus Rayleigh scattering determines the characteristics of scattering by molecules in the atmosphere.

The intensity of light resulting from Rayleigh scattering varies as a function of wavelength where $I \propto \lambda^{-4}$. The consequence of this is evident in the atmosphere where, as a result of this dependency, blue light scatters much more efficiently than red light and hence the sky appears blue.

The intensity of electromagnetic radiation emitted by a Rayleigh scatterer is characterised by that of a dipole. Figure 2.3 illustrates the scattered intensity of electromagnetic waves by a particle whose radius is small compared to the

wavelength of incident radiation, where an equal amount of radiation is scattered in the forward direction as the backward.

Mie scattering of light by particles occurs when the particles are of a similar size to or bigger than the wavelength of the incident electromagnetic radiation. Thus Mie scattering determines the characteristics of scattering by aerosols in the atmosphere, particularly so for the lower part of the atmosphere where aerosols are the dominant scatterer. In the context of this research all aerosols are considered to be confined to the PBL. Above this height aerosols rapidly decrease in number with altitude, but this does not mean they no longer exist. In fact above 15 km in the stratosphere another layer of aerosols can be found whose origin is from volcanic activity [27] [3]. In the context of very high energy gamma ray astronomy this upper aerosol layer can be ignored because the gamma ray induced air showers occur below it, at an altitude of approximately 10 km.

The intensity of electromagnetic radiation emitted by a Mie scatterer is illustrated in Figure 2.4. The scattered intensity of electromagnetic waves by a particle whose radius is large compared to that of the wavelength of the incident radiation is predominantly in the forward direction.

The intensity of radiation scattered in the forward and backward directions is an important parameter for the IACT. In the absence of multiple scattering and inelastic scattering effects, it is therefore reasonable to assume that the amount of light back-scattered by Rayleigh and Mie scattering is light which does not propagate toward the ground and hence is not collected by the IACT telescopes. Thus being able to estimate the amount of this back-scattered light will enable better energy calibration of the inferred primary gamma ray. This thesis considers

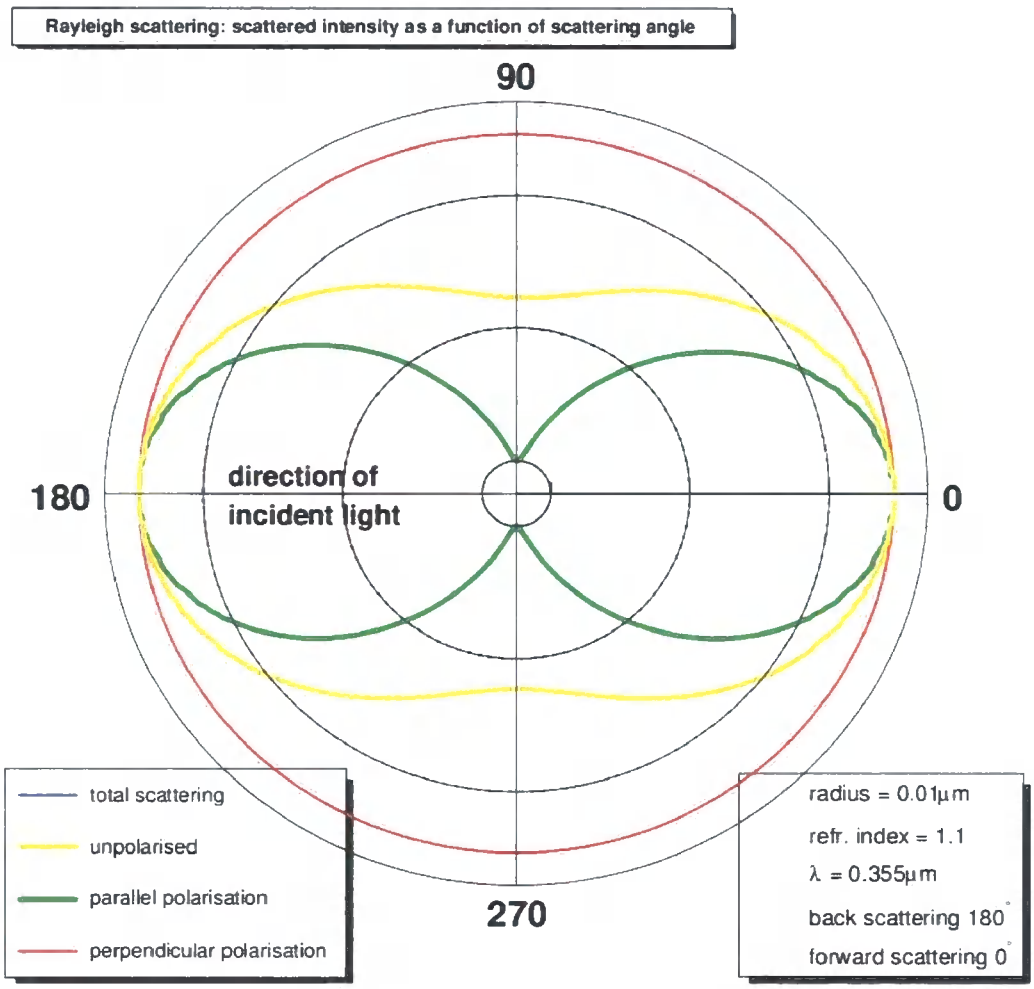

Figure 2.3: Polar plot of scattered intensity versus scattering angle for Rayleigh scattering. When the radius of a particle is « smaller than the wavelength of incident radiation then Rayleigh scattering dominates. As is shown here, Rayleigh scattering can be characterised as a dipole. Scattered intensities calculated using Draine & Flatau's [19] BHMIE code.

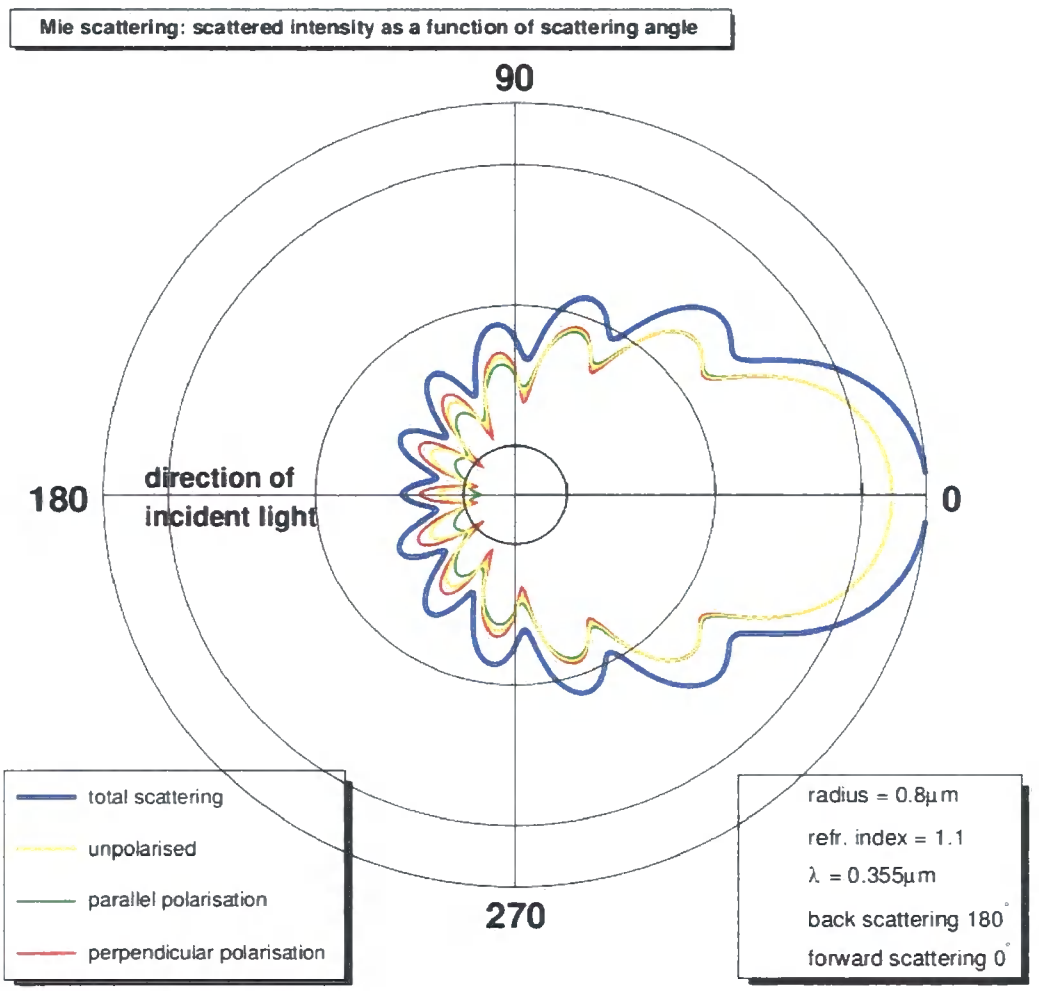

Figure 2.4: Polar plot of scattered intensity versus scattering angle for Mie scattering. When the radius of a particle is large compared to the wavelength of incident radiation then Mie scattering occurs. As is shown here Mie scattering dominates in the forward direction (0°). Scattered intensities calculated using Draine & Flatau's [19] BHMIE code.

back-scattered light to be the electromagnetic waves scattered from a particle at an angle of 180°.

The formalisation of Rayleigh and Mie scattering of an electromagnetic wave by a small particle is a problem encountered in electromagnetic theory. In order to better understand the properties of the scatterer, it is possible to solve Maxwell's equations for an electromagnetic wave incident upon an object such as a homogeneous sphere. This was done by integrating into the computer programs written for this research the widely used BHMIE computer program written by Bohren & Huffman [13] and later modified by Draine & Flatau [19]. The main purpose of the computer program is to calculate the scattering efficiencies (see Equation 2.3) for a given set of physical parameters. This thesis does not present the full solution of Maxwell's equations for an electromagnetic wave incident upon a sphere; for this refer to [13] or [17].

2.3.6 Optical Depth

In Section 2.3.1 it was suggested that extinction can be thought of as the average distance between interactions of electromagnetic radiation and the medium it traverses. Thus for a beam of light travelling through the atmosphere, extinction is a measure of how much the beam of light is absorbed into the atmosphere. Similarly the optical depth can be thought of as the average number of interactions within a medium. Optical depth is therefore unit-less despite its misleading name which might imply distance. Within astrophysics and astronomy, optical depth often refers to the optical thickness of the atmosphere, that is the total amount of extinction along a path through the atmosphere. The usual practice

in astronomy is to estimate the optical depth of the whole atmosphere using starlight. However, in very high energy gamma ray astronomy this method is not wholly adequate for estimating the optical depth from the ground to the height of air showers which occur at an altitude of approximately 10 km. Instead innovative remote sensing techniques need to be implemented in order to estimate the optical depth of the atmosphere to a specific altitude. Remote sensing techniques will be discussed later in Section 2.4.

The optical depth can be represented by Equation 2.5:

$$\tau(h) = \int_0^h \alpha(h)dh \tag{2.5}$$

where h is the height or range in the atmosphere and α is the extinction coefficient. Knowing the optical depth is required in order to estimate the transmission of light through the atmosphere. This is an important parameter for the IACT, as is discussed in the next section.

2.3.7 Transmission of Light

Section 1.5.2 highlighted the transmission of Cherenkov light in the atmosphere as an important IACT parameter. In very high energy gamma ray astronomy it is important to be able to estimate the amount of Cherenkov light that is not collected by the telescopes. The simplest and most widely used method for quantitatively measuring this is to estimate the probability of transmission for light of a specific wavelength passing through a specific medium. The probability of the two-way transmission of light through the atmosphere can be represented

by Equation 2.6:

$$T(h) = exp[-2\tau(h)] = exp[-2\int_0^h \alpha(h)dh] \tag{2.6}$$

where τ is the atmospheric optical depth and h is the range or height within the atmosphere. In a vacuum the probability of transmission is equal to unity i.e. $T(h) = 1$, in other words all photons transmitted at some point would be received at a different point separated by some distance. However, due to the physical processes of absorption and scattering as a result of the various atmospheric components, such as the molecular gases and aerosols, it is expected that the probability of transmission within the atmosphere will be less than unity i.e. $T(h) < 1$. In other words the number of photons detected some distance away is lower than the number transmitted. Therefore the transmission can be thought of as the probability of success (i.e. the probability of non-interaction of an electromagnetic wave) of passing through a medium.

Atmospheric transmission is required in order to estimate the Cherenkov photon flux as shown by Equation 2.7 [54].

$$C(\lambda) = kE(\lambda)T(\lambda) \tag{2.7}$$

where $E(\lambda)$ is the shower Cherenkov emission spectrum, $T(\lambda)$ is the atmospheric probability of transmission for a specific wavelength and k is a constant that depends on various factors such as the number of particles in the shower.

Therefore the transmission probability is a key atmospheric parameter required by IACT Monte Carlo simulations in order to infer the energy of the primary

gamma ray photons.

2.4 Remote Sensing

Remote sensing can be described as the recording of information about an object or phenomenon without actually being in direct contact with the object or phenomenon. Remote sensing techniques are used in many fields including the military and satellite industries; for example the Royal Air Force might monitor the skies of Britain for rogue aircraft, as naturally to cover such a large area of sky requires a method that enables high speed, real time observation. In this case the method most commonly used is of course radar. Similarly, for scientific research it is extremely useful to be able to take measurements of phenomena remotely. In the field of meteorology, clouds are recorded using various instruments such as radar, radiosondes and cloud cameras.

Remote sensing solutions that monitor atmospheric phenomena have been implemented at the H.E.S.S. site in Namibia. These include radiometers, a transmission meter, a ceilometer and a monostatic lidar. It is not the aim of this thesis to discuss the details of each instrument, however further details on the remote sensing instruments located at the H.E.S.S. site can be found in [50]. For a detailed look at remote sensing techniques in general, then Rees [46] is recommended. Instead this thesis focuses on the lidar remote sensing technique implemented at the H.E.S.S. site by the Durham University Very High Energy Gamma Ray Astronomy Group.

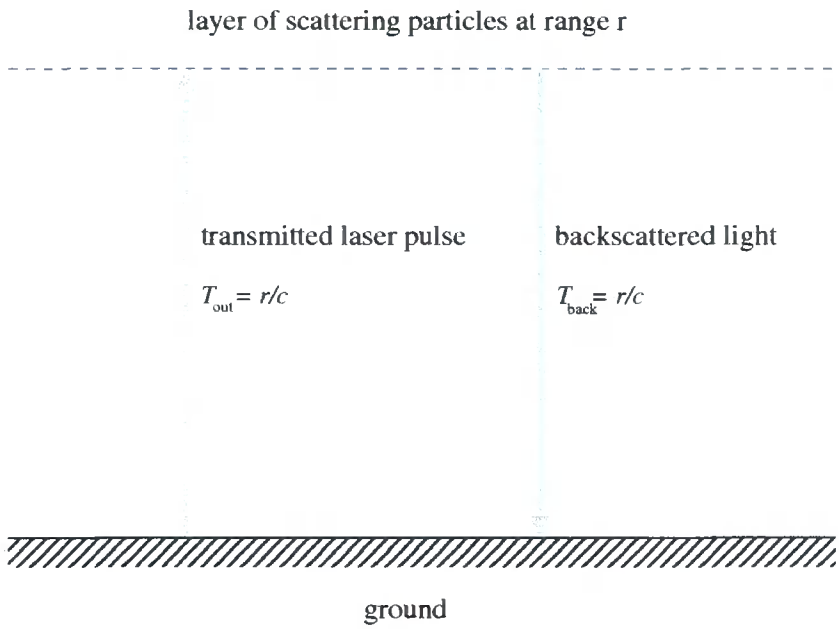

Figure 2.5: The basic concept of the lidar remote sensing technique. The time (T) taken for the transmitted laser pulse to propagate from the lidar to the scattering layer is equal to the distance or range travelled (r) divided by the velocity of the laser pulse (c). The total time taken from the ground to the scattering layer and back again is the sum of the two paths i.e. $T_{out}+T_{back} = 2r/c$ [4].

2.4.1 Lidar Remote Sensing Technique

The word "lidar" is derived from "light detection and ranging". The basics of the lidar technique (see Figure 2.5) involves projecting a beam of light up into the atmosphere; a ground-based detector is then used to record the amount of light that is back-scattered or reflected back down to the ground.

A lidar works on the same principle as a radar except for the wavelength of the transmitted radiation; the lidar remote sensing technique uses a much shorter wavelength optical beam as opposed to radio waves employed by radar. The optical beam source in a lidar is a laser operating most commonly at 355 nm

(near ultra-violet) and 532 nm (optical green) wavelengths. The H.E.S.S. lidar operates at a wavelength of 355 nm which is near to the Cherenkov light peak of ≈320 nm. The wavelength of the lidar's laser is important if a lidar is to be useful to the IACT and this will be discussed later in Section 3.1.

Within the context of the IACT, the basic lidar remote sensing technique might proceed as follows:

- a series of lidar laser pulses is fired into the atmosphere;
- the lidar records the raw signals and filters them for noise in order to suppress the background;
- the corrected signals are then used to calculate the height varying extinction coefficient and/or backscatter coefficient. This is usually done with a certain number of assumptions about the aerosols present at the measurement site;
- finally, the lidar-recorded extinction and backscatter coefficients can be used to estimate the probability of transmission for light at the lidar's wavelength through the local atmosphere.

Chapter 3 will present and discuss the techniques used for determining the probability of transmission using the measurements recorded with a lidar.

2.4.1.1 Lidar Configuration

Lidars can be configured in different ways, but the basic components of the instrument include:

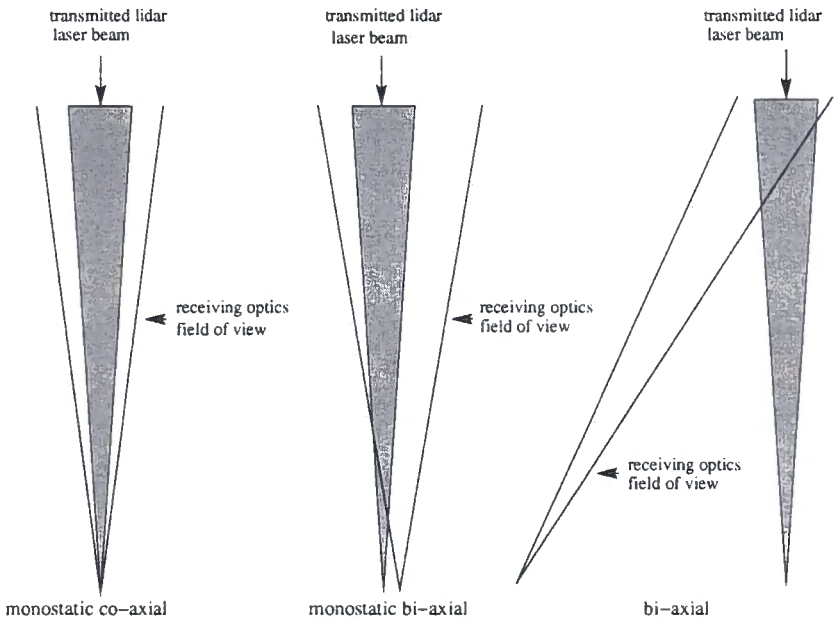

Figure 2.6: The most widely used lidar configurations. The H.E.S.S. lidar is set-up in a monostatic bi-axial configuration which imposes a lower boundary limit.

- the transmitter - the laser beam which is fired into the atmosphere;
- the receiver - includes the optical mirror for collecting and focusing the back-scattered light through a narrow-band filter to minimise background;
- the detector - converts the detected light into electrical signal. Usually a Photo Multiplier Tube (PMT), but can also be a Micro-Channel Plate (MCP), photodiode or Charge-Coupled Device (CCD).

The two components which govern the instrument's field of view, the transmitter and the receiver, are usually configured in one of three different ways.

Figure 2.6 illustrates each of these three different lidar field of view configurations. The lidar at the H.E.S.S. site is set up in a mono-static bi-axial configuration. Such a configuration means that there is an enforced lower boundary limit of

approximately 300 m which is the point at which the transmitted laser crosses into the receiver's field of view. Thus, under 300 m, analysis of the atmosphere cannot be done by the lidar and instead it is done by a transmissometer (transmission meter) which will not be discussed in this thesis. Further information on the transmissometer located at the H.E.S.S. site can be found in [50].

For more information on the instrumentation of a lidar, including the techniques used for signal detection and recording such as photon counting, further investigation of Argall [4] is recommended.

2.4.1.2 Specifications of The Easy-Lidar ALS450XT

Chapter 4 will present the results of analysis conducted using data from the lidar located on the H.E.S.S. site in Namibia. This is a commercially built lidar developed with Leosphere, the Easy-Lidar ALS450XT. Table 2.1 details the main specifications of this instrument:

Table 2.1: Lidar Specifications: Easy-Lidar ALS450XT

Laser Specifications:	
wavelength:	355 nm
frequency:	20 Hz
output density of energy:	31.1 J per sq m
Detection Specifications:	
detector:	PMT
range:	50 m up to 15 km
spatial resolution:	1.5 m
optical head dimensions:	60x38x20 cm

This thesis will not concentrate on the instrumentation but rather on the analysis techniques of lidar data and how the lidar remote sensing technique is of use to the IACT.

2.5 The Local Atmosphere

The H.E.S.S site, introduced in Section 1.7, is located 1800 m above sea level in the Gamsberg region of Namibia. This region can be described as an arid semi-desert plateau benefiting from a stable climate and good seeing. In terms of atmospheric models the H.E.S.S. site is best described by MODTRAN's tropical model. Radiosonde measurements taken in Windhoek, which is < 100 km from the H.E.S.S. site, have been compared against the MODTRAN atmospheric models listed in Section 2.2.1.

Figure 2.7 clearly illustrates that MODTRAN's tropical model fits best with the seasonal changes recorded using radiosondes. Bernlöhr [9] shows that using an inappropriate atmospheric model to infer primary gamma ray energies can result in systematic errors because of the significant difference in Cherenkov photon density yield between models. As an example Bernlöhr [9] shows that a photon density yield difference of 60% between the Antarctic winter model and the tropical model exists. Thus being able to conduct radiosonde measurements on-site, at least quarterly, would help to establish a molecular atmospheric model appropriate for the IACT.

On-site measurement of the local aerosol optical properties have not been conducted at the H.E.S.S. site in Namibia. Instead it has been assumed that the aerosol properties at the H.E.S.S. site closely match the aerosol optical properties described by the bi-modal desert dust model. Part of this research is to discover whether the optical properties of aerosols can be inferred using the lidar remote sensing technique. This will be discussed in Chapter 4.

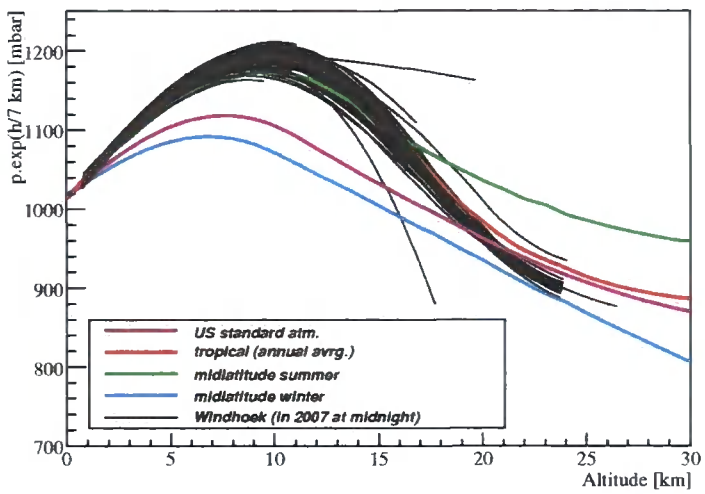

Figure 2.7: Seasonal comparison of radiosonde measurements (black lines) versus MODTRAN's atmospheric models. The radiosonde measurements were taken in Windhoek, which is < 100 km from the H.E.S.S. site. These radiosonde measurements suggest that the MODTRAN tropical model fits best with the local atmosphere. Image courtesy of Dr. S.Nolan: private communication.

A parameter which can affect the optical properties of aerosols is relative humidity. Figure 2.8 illustrates the average relative humidity recorded at the site for the period March 2004 through to and including September 2008. The average relative humidity does not peak above 80%, from which it is inferred that on a seasonal timescale the site enjoys very good atmospheric conditions for astronomy and in particular very high energy gamma ray astronomy employing the IACT.

Figure 2.8 also shows that relative humidity peaks around the first quarter of each year, which is mid summer and the season during which Namibia receives its peak rain fall. The assumption that the H.E.S.S. site can be represented by a Desert Dust aerosol model means that if relative humidity is below 90%, it has little influence on the aerosol optical properties as suggested by Ackermann [1].

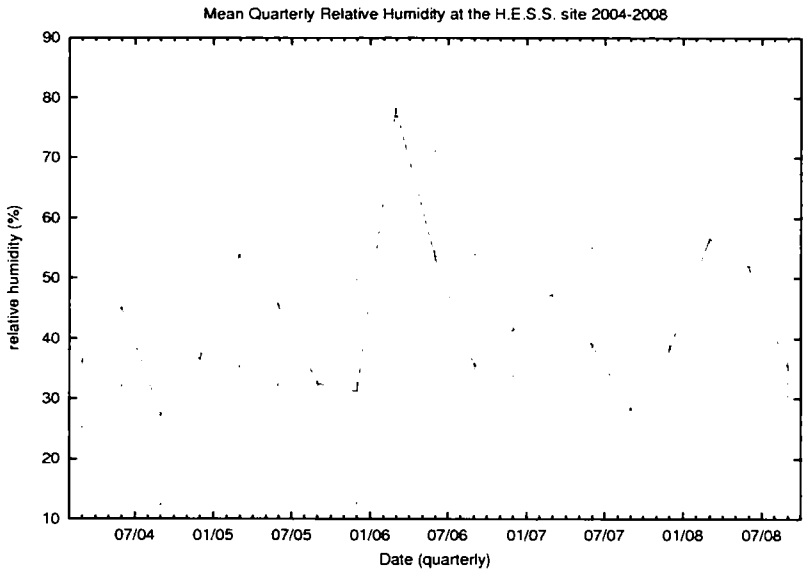

Figure 2.8: Average Quarterly Relative Humidity recorded at the H.E.S.S. site in Namibia from 2004-2008. Relative humidity tends to peak in the first quarter during mid-summer when Namibia receives the majority of its annual rainfall. The error bars show the spread of values rather than the uncertainty.

Figure 2.8 suggests that on a seasonal timescale the relative humidity is unlikely to go above 90%; however, this is not impossible. If there is a detour from the desert dust aerosol model, then relative humidity is an important parameter for atmospheric monitoring of aerosols and their impact on the IACT.

The aerosols present at the H.E.S.S. site are assumed to have the same optical properties as those used by Barnaba & Gobbi [6] which are summarised in Table 2.2.

Table 2.2: Bi-modal Desert Dust Aerosol Optical Properties at the H.E.S.S. site in Namibia [6]

				Refractive Index	
$Mode$	$Radii(\mu m)$	$Composition(\%)$	$Number/cm^{-3}$	m_{real}	$m_{imag}(\times 10^{-3})$
1	0.02-0.08	93-98	180-1470	1.50-1.55	4-8
2	0.3-1.5	2-7	4-105	1.50-1.55	4-8

Chapter 3

Lidar Analysis Techniques and Theory

The previous chapter introduced the lidar remote sensing technique and how it can be used to measure certain atmospheric parameters useful for the imaging atmospheric Cherenkov technique (IACT). This chapter aims to expand upon these basic concepts by discussing the accepted lidar analysis techniques suitable for extracting probability transmission profiles. Section 3.1 introduces the lidar equation the solution of which is fundamental to the remote sensing lidar technique. This is followed by discussion of three established methods widely used for analysis of lidar data. Section 3.5 then presents and discusses a numerical method for determining the aerosol lidar ratio using Mie theory. Finally, Section 3.6 discusses a model that can be used to generate a vertical profile of the changing lidar ratio.

3.1 The Lidar Equation

For a vertically pointing monostatic lidar like the Easy-Lidar ALS450XT the return signal received can be represented by the equation:

$$P(r) = P_0 C r^{-2} \beta(r) T(r) \tag{3.1}$$

where:

- r is the range;
- P_0 is the power of the transmitted optical beam;
- C is an instrumentation constant that takes into account the efficiencies of the transmitting and receiving optics, including any overlap function to allow for the lidar configuration as illustrated in Figure 2.6;
- β(r) is the backscatter at range r;
- T(r) is the probability of transmission from the lidar to range r.

Range as opposed to height has been used above because a lidar measurement is not necessarily taken at the zenith angle in which case any height calculations need to be angle corrected.

Section 2.3.7 introduced the probability of transmission and discussed its importance to the IACT. The probability of transmission, Equation 2.6, can be substituted in Equation 3.1 above. Hence the lidar equation is now written as:

$$P(r) = P_0 C r^{-2} \beta(r) exp[-2 \int \alpha(r') dr'] \tag{3.2}$$

Solving for the lidar equation makes it possible to find the probability of transmission for a single wavelength. This result can then be represented by a model, and assuming its predictions are correct, the probability of transmission can be inferred for the Cherenkov radiation wavelengths in the range 280 nm to 650 nm detected using the IACT. The the optical beam of a 355 nm lidar is expected to propagate very similarly to Cherenkov light through the atmosphere; because the wavelengths are comparable, both will undergo similar amounts of absorption and extinction from molecular and aerosol particles in the atmosphere.

The challenge in solving Equation 3.2 is that there are two unknowns in the equation i.e. the extinction coefficient α and the backscattering coefficient β. A single scattering lidar can only measure one of these values with a good degree of accuracy. The second unknown is usually derived by making certain assumptions regarding the functional relationship that exists between extinction and backscatter. The following sections discuss the accepted approaches and assumptions required in order to solve the lidar equation.

3.2 The Klett Method

The first and most widely used lidar analysis technique to solve for extinction and backscatter is the Klett inversion method. This is a simple analytical method that provides a stable solution for processing lidar return signals. Klett [32] suggests the logarithmic range-corrected power value is a much more convenient variable to work with. This is defined by:

$$S(r) = ln[r^2 P(r)] \tag{3.3}$$

This can be normalised so that an auxiliary function, commonly referred to as the S-function, is created:

$$\begin{aligned} S(r) &= ln\left[\frac{P(r)r^2}{P(r_0)r_0^2}\right] \\ &= ln\left[\frac{\beta(r)}{\beta_0(r)}\right] - 2\int \alpha(r')dr' \end{aligned} \tag{3.4}$$

Where r_0 is a constant reference range, usually defined as the far-end range, which in this case would be a height at or above the lidar range limit i.e. $r_0 \geq$ 15,000 m. The differential of Equation 3.4 is:

$$\frac{dS}{dr} = \frac{1}{\beta}\frac{d\beta}{dr} - 2\alpha \tag{3.5}$$

which is a Bernoulli differential equation and Klett [32] suggests that any solution to such an equation requires knowing or assuming a relationship between α and β. Klett also suggests that this relationship can be approximated using a power law:

$$\beta(r) = M\alpha(r)^k \tag{3.6}$$

where M is a constant and k depends on the lidar wavelength used as well as the constituents of the local atmosphere. By assuming such a power law relationship Klett then reformulates Equation 3.5 by firstly substituting Equation 3.6 into Equation 3.4 and then taking the derivative to get:

$$\frac{dS}{dr} = \frac{k}{\alpha}\frac{d\alpha}{dr} - 2\alpha \tag{3.7}$$

then assuming that k is a constant, a solution to this Bernoulli differential equa-

tion can be written for α as:

$$\alpha(r) = \frac{exp\left[\frac{S(r) - S_0(r)}{k}\right]}{\alpha_0^{-1} - \frac{2}{k}\int exp\left[\frac{S(r) - S_0(r)}{k}\right]dr'} \tag{3.8}$$

where $\alpha_0 = \alpha_0(r_0)$ and is an estimate for the extinction at the very far end of the lidar range where one would expect to find a molecular dominated atmosphere almost free from aerosols.

The main weakness with the Klett method resides in the assumptions that need to be made. For example, the far-end boundary value α_0 must be extrapolated from a lower range value. Similarly, empirically solving for this value is non-trivial, if not impossible. However, Knauss [34] suggests that overestimating the far-end boundary value α_0 is preferable in order to minimise any error resulting from an incorrect guess.

Furthermore the approach of using the relationship defined in Equation 3.6 can also lead to errors. The usual practice is to solve Equation 3.6 assuming $k = 1$ or $k \approx 1$ as done by Carnuth & Reiter [15], however this may not be an accurate representation of the real functional relationship at the site of measurement.

Nonetheless, the Klett method provides a stable solution for the extinction coefficient which performs exceptionally well as a first order approximation. The results of the Klett method as applied to lidar measurements taken at the H.E.S.S. site in Namibia are presented and discussed in Chapter 4.

3.3 The Fernald Method

Building on the stability of the Klett method, Fernald presents an extra level of detail in solving for the extinction and backscatter coefficients. The Fernald solution to the lidar equation takes into account the scattering properties of both the aerosol and molecular components. In this way, a profile of the dominant aerosol scatterers can be built up in the lower part of the atmosphere, in particular the region in which Cherenkov light from gamma ray air-showers propagates. For this method to be successful a prerequisite is that some knowledge of the local atmosphere constituents is available e.g. whether there is dust, salt or any other minerals present. Section 2.2 introduced molecular and aerosol atmospheric models and it is normal practice to know which of these applies when using the Fernald method. As highlighted in section 2.2 the molecular atmosphere is somewhat predictable and Fernald suggests that the molecular scattering component can be modelled accurately to first order using molecular atmospheric models like those presented in Section 2.2.1. Thus the primary difference between the Klett and Fernald methods is that the Fernald method treats molecular scattering as an inherent background.

It has already been established that extinction and backscatter results from both molecular and aerosol particles. Thus the following relationships can be written:

$$\beta_{total}(r) = \beta_M(r) + \beta_A(r) \tag{3.9}$$

$$\alpha_{total}(r) = \alpha_M(r) + \alpha_A(r) \tag{3.10}$$

where subscript M denotes molecular and subscript A to denotes aerosol. In

addition to the relationships outlined above the extinction to backscatter ratio, or lidar ratio, can be defined as:

$$L(r) = \frac{\alpha(r)}{\beta(r)} \tag{3.11}$$

and hence the respective aerosol and molecular lidar ratios:

$$L_A(r) = \frac{\alpha_A(r)}{\beta_A(r)} \tag{3.12}$$

$$L_M = \frac{\alpha_M(r)}{\beta_M(r)} = \frac{8\pi}{3}\text{steradians} \tag{3.13}$$

Fernald [22] suggests that the probability of the two-way transmission for the aerosol scattered light can be expressed as:

$$\begin{aligned} T_A(r) &= exp\left[-2\int_0^r \alpha_A(r')dr'\right] \\ &= exp\left[-2L_A\int_0^r \beta_A(r')dr'\right] \end{aligned} \tag{3.14}$$

and similarly for the molecular scattered light:

$$\begin{aligned} T_M(r) &= exp\left[-2\int_0^r \alpha_M(r')dr'\right] \\ &= exp\left[-2L_M\int_0^r \beta_M(r')dr'\right] \\ &= exp\left[-\frac{16\pi}{3}\int_0^r \beta_M(r')dr'\right] \end{aligned} \tag{3.15}$$

Finally Fernald [21] presents a revised lidar equation which distinguishes between

the aerosol and molecular scatterers:

$$P(r) = P_0 C r^{-2} \Big[\beta_A(r) + \beta_M(r)\Big] T_A(r) T_M(r) \tag{3.16}$$

As previously mentioned, Fernald suggests that two of the unknown quantities in this new representation of the lidar equation ($\beta_M(r)$ and $\alpha_M(r)$) can be estimated using the atmospheric models presented in Section 2.2, leaving only the aerosol extinction $\alpha_A(r)$ and backscattering $\beta_A(r)$ still to be determined. Due to the complexity of deriving a vertical lidar ratio profile, a constant lidar ratio is often used with this method. This requires the assumption that the aerosol properties do not change vertically within the small column of measurement.

The performance of the Fernald method is dependent on the accuracy of the atmospheric model used to obtain $\alpha_M(r)$. Use of a model atmosphere that does not best describe the measurement site can lead to errors in the probability of transmission. For example Bernlöhr [9] points out that a difference of up to 60% in the probability of transmission of Cherenkov light exists between the tropical and the polar atmospheric models. Therefore it is reasonable to expect a similar size of error for a lidar measurement at similar wavelength.

Like the Klett method, the Fernald method also relies, although weakly, on an accurate guess of the far-end boundary extinction value (α_0), but unlike the Klett method it is not sensitive to an incorrect power-law approximation describing the relationship between α and β. Instead, this method requires either an accurate guess of the lidar ratio or at least accurate modelling of the lidar ratio by means of Mie theory.

There are two ways to solve the lidar equation using the Fernald Method.

3.3.1 The Fernald Algorithm

The aerosol extinction and backscatter coefficients can be solved by implementing the Fernald algorithm and the relationship represented in Equation 3.12. The Fernald algorithm can be represented by Equation 3.17 and Equation 3.18, adapted from Rocadenbosch [47]:

$$\beta_A(r) = \frac{P(r)r^2 exp\left[\xi(u)du\right]}{\frac{P(r_m)r_m^2}{\beta_A(r_m)+\beta_M(r_m)} + 2\int_r^{r_m} L_A(v)P(v)v^2 exp\left[\xi(u)du\right]dv} - \beta_M(r) \tag{3.17}$$

and

$$\xi(u) = 2\int_r^{r_m}\left[L_A(u) - L_M\right]\beta_M(u)du \tag{3.18}$$

where r, u and v are all the measurement range and r_m is the far-end boundary range. It is also worth noting that the logarithmic S-function, Equation 3.3, has not been used in Fernald's algorithm. Instead the linear range-corrected lidar return signal ($P(r)r^2$) is used. Young [55] suggests that this is to prevent heavy smoothing of the function which creates an artificial bias.

Finally the Fernald algorithm eliminates the need to guess for an extinction coefficient at the far-end boundary. Instead, the far-end boundary backscatter coefficient is required whose value can be approximated to zero as no aerosols are expected to exist at this boundary height. The results of the Fernald algo-

rithm, as applied to the lidar measurements conducted at the H.E.S.S. site, are presented and discussed in Chapter 4.

3.3.2 Klett's Revised Solution

Klett [33] presents a revised solution taking into account both Rayleigh and Mie scattering. This revised approach is consistent with Fernald's approach which aims to solve for the backscatter coefficient. Hence Klett expresses the following relation for total backscatter:

$$\beta(r) = B_A \alpha_A(r) + B_M \alpha_M(r) \tag{3.19}$$

where B is the inverse of lidar ratio for the respective aerosol and molecular components.

For the aerosol component it is acceptable to use either the inverse of an aerosol lidar ratio (usually in the range 10 - 100 str) or to first estimate the lidar ratio with greater accuracy by implementing a Mie theory Monte Carlo simulation. Strictly speaking the aerosol lidar ratio varies with height as suggested by Equation 3.11. However, for simplicity this thesis only considers the case where the aerosol lidar ratio remains constant with height. Section 3.6 will discuss a model for determining the functional relationship between extinction and backscatter that can be used in order to determine the aerosol lidar ratio as a function of height.

Klett defines a modified S-function as follows:

$$S' - S'_m = S(r) - S_m(r) + \frac{2}{B_M} \int_r^{r_m} \beta_M dr' - 2 \int_r^{r_m} \frac{\beta_M}{B_A} dr' \tag{3.20}$$

from which a new Bernoulli differential equation consistent with Equation 3.5 can be derived:

$$\frac{dS'}{dr} = \frac{1}{\beta}\frac{d\beta}{dr} - \frac{2\beta}{B_A} \tag{3.21}$$

This leads to Klett's revised solution for determining total backscatter consistent with the Fernald approach. This revised solution can be represented as:

$$\beta_{total}(r) = \frac{exp\left[S' - S'_m\right]}{\beta_m^{-1} + 2\int_r^{r_m} \frac{exp\left[S' - S'_m\right]}{B_A} dr'} \tag{3.22}$$

The aerosol backscatter can be calculated by rearranging the relationship defined in Equation 3.22:

$$\beta_A(r) = \beta_{total}(r) - \beta_M(r) \tag{3.23}$$

Finally, by substituting this into Equation 3.14 the probability of transmission in the presence of aerosol scatterers is found. The results for Klett's revised solution, as applied to the lidar measurements conducted at the H.E.S.S. site, are presented and discussed in Chapter 4.

3.4 Multi-angle method

The final lidar analysis technique is called the multi-angle method which came about because of the inherent difficulty associated with solving the lidar equation discussed in Section 3.1, that is that the lidar equation tries to solve two unknowns with one lidar return signal, a task that cannot be done without a

number of assumptions. Therefore, the multi-angle approach is an attempt to limit the number of assumptions that need to be made by the Klett and Fernald methods in order to solve for atmospheric extinction and backscatter. Limiting or even eliminating the number of assumptions required to derive the probability of transmission means greater confidence can be placed in the results which ultimately help to infer accurately the energy of primary gamma ray photons.

The main difference between the first two methods addressed in this thesis is that they both assume columnar homogeneity for any given range, whereas the multi-angle method assumes that the local atmosphere is horizontally as opposed to vertically invariant. In principle, this different approach is sound, certainly within reasonable limits and certainly when applied to the atmosphere above the effective area of an array of Cherenkov telescopes like that of H.E.S.S. For example one Cherenkov telescope, like that illustrated in Figure 1.13, has an effective area of 10^4 m^2 which translates to a horizontal ground diameter of approximately 100 m. It is not unreasonable to expect the atmosphere to be invariant over that distance scale or even a distance scale an order of magnitude greater. However, for observations at large zenith angle assuming horizontal homogeneity is no longer valid. This is because large zenith angles translate to greater horizontal distances and hence scales on which the atmosphere can no longer be horizontally invariant. This suggests that the multi-angle method should only be considered for small zenith angle IACT observations.

In addition, astronomical observations using the IACTs are only performed during total darkness when the atmosphere at the H.E.S.S. site suffers from fewer instabilities induced by convection processes during the warm days. However,

atmospheric instability does have a seasonal dependence as illustrated by Figure 2.8 when the average relative humidity peaks during mid-summer in Namibia which is normally during the first quarter of each calendar year.

The basic concept of the multi-angle method is to take measurements with a lidar maintaining a constant azimuth, but for each measurement select a new zenith angle. It is usual practice to take the first measurement at zenith and then work down to bigger angles away from zenith. Figure 3.1 illustrates the concept of the multi-angle method. To test the assumptions made under this method it is also possible to take equal measurements at opposite azimuth angles i.e. a set of zenith angle measurements can be recorded for an azimuth of 0 degrees and a matching set of zenith angle measurements can also be recorded for an azimuth of 180 degrees. In addition it is possible to take a horizontal measurement (90 degrees from zenith) to test the lidar response across the horizontal atmosphere.

The multi-angle method investigated here is that suggested by Filipčič et al [23]. This method is of interest because it is currently being used for fluorescence-detector energy calibration at the Pierre Auger Observatory, which too has a requirement to determine how much of the cosmic ray induced fluorescence being collected is absorbed or scattered by atmospheric particles [8].

The detection volume at the Pierre Auger Observatory is approximately $3000\ \mathrm{km}^2$ ground area by 15km in height. This is a much larger detection volume to that of H.E.S.S., which has a ground area of approximately $0.03\ \mathrm{km}^2 (\sim 30,000\ \mathrm{m}^2)$ and a similar height range of 12 km. As previously mentioned, the H.E.S.S. experiment is located at an altitude of approximately 1800 m above sea level, compared to the Pierre Auger Observatory which is located at an altitude of

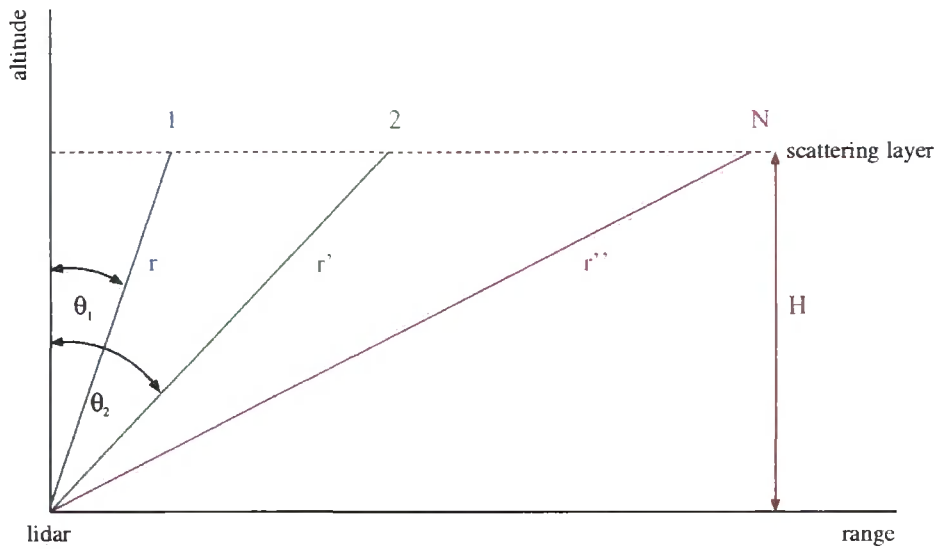

Figure 3.1: Illustrated here is the basic concept of the multi-angle method. The lidar is fired at different zenith angles (θ), each pulse travels a range r, r' and r'' to a scattering layer. To estimate the altitude (H) of the scattering layer, the range needs to be multiplied by the cosine of the zenith angle because the lidar pulse has to travel a greater distance to reach the scattering layer when fired at larger zenith angles. Adapted from Pahlow et al [43]

1450 m above sea level. Both experiments are located in desert regions. Despite being on different continents there are obvious atmospheric parameters shared by both experiments.

Building on the terminology introduced in the Klett and Fernald methods, Filipčič et al [23] presents a revised S-function taking into account both the height and the angle from zenith at which the lidar measurement was taken:

$$S(h,\theta) = ln\left[\frac{\beta(h)}{\beta_0}\right] - 2\theta\tau(h,h_0) \tag{3.24}$$

where $\theta = \frac{1}{cos\phi} = sec\phi$, $\tau(h,h_0) = \int_{h_0}^{h} \alpha(h')dh'$ and $\beta_0 = \beta(h_0)$.

As mentioned above, the principle of the multi-angle method is to take lidar

measurements at two or more different angles. The angles of measurement are denoted by θ_1 and θ_2.

Filipčič et al [23] presents two solutions, one for the vertical optical depth:

$$\tau(h) = -\frac{1}{2}\frac{S(h,\theta_1) - S(h,\theta_2)}{\theta_1 - \theta_2} \tag{3.25}$$

and one for the backscatter coefficient ratio:

$$\frac{\beta(h)}{\beta_0} = exp\left[-\frac{\theta_2 S(h,\theta_1) - \theta_1 S(h,\theta_2)}{\theta_1 - \theta_2}\right] \tag{3.26}$$

Finally Filipčič et al [23] suggests that both solutions of Equation 3.25 and 3.26 are proportional to the difference of the S-functions for each angle at the corresponding height and therefore a small separation between the angles allows for Equation 3.25 to be represented in a differential form:

$$\tau(h) = -\frac{1}{2}\frac{\partial S}{\partial \theta}\Big|_h \tag{3.27}$$

Thus by finding the gradient of the S-functions with respect to the angle of measurement, the probability of transmission is then calculated as highlighted in Equation 2.6 by finding the exponential of $\tau(h)$, the optical depth.

The major strength of the multi-angle method is the limited number of assumptions that need to be made apart from the, not unreasonable, assumption that the local atmosphere is horizontally invariant. The results of implementing the multi-angle method, as applied to the lidar measurements conducted at the H.E.S.S. site, are presented and discussed in Chapter 4.

3.5 Determining The Aerosol Lidar Ratio

The aerosol lidar ratio is a requirement of the Fernald method where it is assumed to be constant over all altitudes. It is possible to calculate an aerosol lidar ratio by implementing the concept introduced in Section 2.3.4 i.e. the cloud of many particles concept in which the scattering layer of aerosols is imagined as a distribution of spherical particles each with different sizes, but sharing the same optical properties.

The aerosol lidar ratio (L_A) represented in Equation 3.12 is really the ratio between the sum of all extinction and backscatter coefficients for all aerosol components. Therefore Equation 3.12 can be rewritten as:

$$L = \frac{\int_0^\infty \sum_{i=1}^{M} \alpha_i(r)dr}{\int_0^\infty \sum_{i=1}^{M} \beta_i(r)dr} \tag{3.28}$$

where α is the extinction coefficient, β the backscatter coefficient, r the particle radius and i the aerosol index of M modes. In order to treat the aerosols as a cloud of many particles, Equation 3.28 needs to be related to Equation 2.4. This can easily be done using the Mie theory efficiency factors for extinction and backscatter. Hence the lidar ratio can be represented as:

$$L = \frac{\sum_{i=1}^{M} \pi r^2 \int_0^\infty Q_{ext}(r, \lambda, m_i) n_i(r)dr}{\sum_{i=1}^{M} \pi r^2 \int_0^\infty Q_{back}(r, \lambda, m_i) n_i(r)dr} \tag{3.29}$$

where Q is the efficiency factor whose value is dependent on the particles' radius r, the incident wavelength λ and the particles' refractive index m. The many particles of different radius r can be described by a distribution $n_i(r)$ where index i denotes the aerosol component of M modes.

The lidar ratio can be calculated by employing a Monte Carlo numerical method, which is the approach taken by various authors including Barnaba & Gobbi [6], who were looking for the possible functional relationships that link backscatter and extinction, and Ackermann [1], who was looking for the lidar ratio using different aerosol models. A Monte Carlo numerical approach overcomes some of the challenges inherent when trying to solve such a problem. Aerosols are highly variable and this includes their characteristics like size, distribution and optical properties. A Monte Carlo numerical approach is efficient at processing large sets of size distributions as well as randomly selecting the distribution's descriptive parameters from any given range.

Therefore this approach is ideal for generating a large sample of aerosol particles whose properties are randomly chosen from the ranges outlined by the desert dust model in Table 2.2. It is assumed that the aerosols present at the H.E.S.S. site in Namibia follow a lognormal distribution as required by the desert dust model [27]. Generating a random sample of particles is only the first step towards calculating the lidar ratio. The second step is to find the efficiency factors by solving Maxwell's equations for an electromagnetic wave incident upon a sphere for each particle in the scattering cloud. This is done by integrating an adapted version of the BHMIE computer code into the Monte Carlo numerical method. The BHMIE computer code was introduced in Section 2.3.5 and a C++ adapted

version of the computer code used in this thesis is attached in the Appendix. The final step in the Monte Carlo numerical method is to solve Equation 3.29 by summing over all radii for each aerosol mode. As required by the Fernald method, this value can then be used to solve Fernald's algorithm Equation 3.17 and Equation 3.18 or Klett's revised backscatter solution Equation 3.22 and Equation 3.23.

The results of this Monte Carlo numerical method implementation are presented and discussed in Chapter 4.

3.6 Modelling the relationship between extinction and backscatter

Section 3.5 mentioned that Barnaba & Gobbi [6] used a Monte Carlo numerical approach in order to look at the possible functional relationships that exist between extinction and backscatter. In their research Barnaba & Gobbi [7][6] plot the extinction coefficients versus the backscatter coefficients for all aerosol size distributions, to which they fit a 7^{th} order polynomial. It is suggested that an expression of this kind best describes the functional relationship between extinction and backscatter i.e. $\alpha = \alpha(\beta)$. The order of polynomial used depends on whether a mix of aerosol models or a single aerosol model is being analysed. For example Ackermann [1] analyses each aerosol model individually and for the desert dust model fits only a 5^{th} order polynomial.

Both of these approaches are in contrast to the assumption made under the Klett method that the functional relationship between extinction and backscat-

ter is best described by a simple power law. Klett [32] demonstrates that an empirical relationship can be found between extinction and backscatter coefficients by using linear regression to fit Equation 3.6 to lidar-returned data. Klett also demonstrates that a lognormal function can be fitted to the lidar-returned extinction coefficients for a range of lidar ratios from 0 to 100 steradians.

The research undertaken for this thesis includes implementing the Monte Carlo numerical method discussed in Section 3.5 in order to determine any functional relationship between the extinction and backscatter of aerosol scatterers assumed to exist at the H.E.S.S site in Namibia. All of the functions discussed above have been fitted to the results obtained in the Monte Carlo numerical method. In addition, it has been shown that fitting a 6^{th} order polynomial to the Monte Carlo generated lidar ratios and extinction coefficients can be used with lidar recorded extinction values to obtain a vertical profile of the changing lidar ratio. The purpose of this is to demonstrate that assuming a constant lidar ratio under the Fernald method is not good practice and instead a varying ratio dependent on height should be used.

All the results of the analysis undertaken for this thesis are presented and discussed in Chapter 4. This includes the results, of the analysis methods presented in this chapter, as applied to data recorded with the Easy-Lidar ALS450XT at the H.E.S.S. site in Namibia.

Chapter 4

Lidar Results and Analysis

The following chapter presents and discusses the results of the Mie scattering analysis and the lidar analysis undertaken for this thesis. Section 4.1 outlines the approach taken in order to produce a Monte Carlo simulation that estimates an integrated lidar ratio which is used in Section 4.2.2 for the Fernald method. Section 4.2 then outlines how data were collected using a single scattering mono-static lidar located at the H.E.S.S. site in Namibia. This is followed by the results of the Klett method, the Fernald method and the multi-angle method in Sections 4.2.1, 4.2.2 and 4.2.3. Section 4.3 presents and discusses the models fitted to the apparent relationships explored during the Monte Carlo numerical analysis. Finally Section 4.4 discusses how one of these models can be used to derive the vertical lidar-ratio profile.

4.1 Mie Scattering Analysis

Section 3.5 discussed how a lidar ratio can be calculated by implementing a Monte Carlo simulation. Two computer programmes were written using the C++ computer programming language including library functions from the ROOT (version 5.14) object-orientated data analysis framework. The two programmes, minimie.cpp and fullmonty.cpp, are both included on a compact disc attached to this thesis. The first of these two programmes, minimie.cpp, randomly generates 20,000 aerosol distributions as described by Equation 3.29. The aerosol optical properties and sizes for each distribution are randomly selected from the ranges highlighted in Table 2.2. Integrated into the programme is the BHMIE code [19] which is included as a function and called in order to solve for the extinction and backscatter efficiency factors for each random distribution. The programme then uses these values to solve the integral given in Equation 3.29.

Empirical evidence suggests that desert dust aerosols are log-normally distributed [27] and Figure 4.1 illustrates a sample of a randomly generated bi-modal desert dust aerosol which follows a lognormal distribution. The two components of the bi-modal desert dust aerosol model used in this analysis are: a water soluble component which, as Table 2.2 suggests, is the largest by number per unit volume; and a mineral component that is fewer in number but has a much greater radius than the water soluble component.

Figure 4.2 illustrates the calculated extinction efficiency factors for each component of the bimodal desert dust aerosol model. Figure 4.2 shows the evolution of the extinction efficiency with changing component radius. Similarly Figure 4.3 illustrates the backscatter efficiency factor for each component of the bi-modal

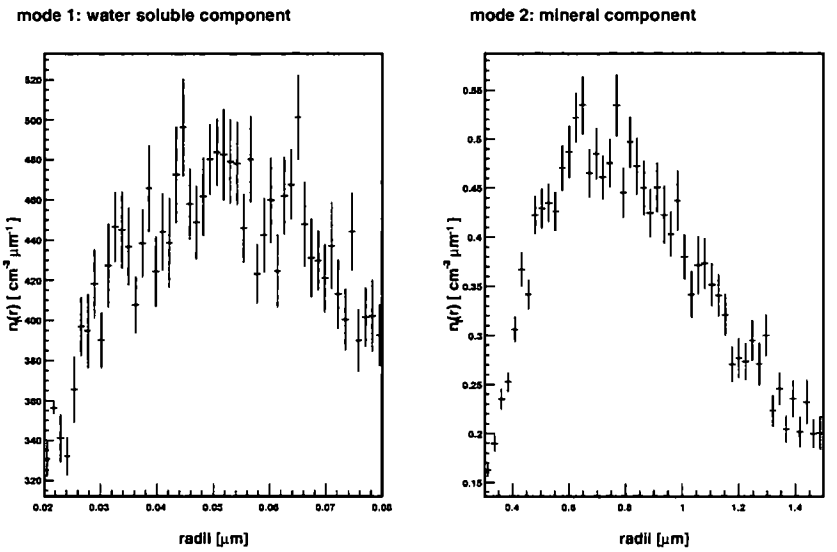

Figure 4.1: The lognormal distribution of the bi-modal desert dust aerosol created for the Mie scattering analysis. These two distributions were generated by 20,000 random selections from the aerosol ranges highlighted in Table 2.2. The bi-modal aerosol is comprised of a water soluble component (left) and a mineral component (right).

desert dust aerosol model. Consistent with lidar backscatter, the backscatter efficiency factor is the scattering efficiency estimated at the backscattering angle of 180 degrees. Figure 4.3 shows the evolution of the backscatter efficiency factor with changing component radius.

The minimie.cpp code sums up the numerator and denominator of Equation 3.29 in order to obtain the respective extinction and backscatter coefficients. These are then summed and the extinction versus backscatter ratio then provides an integrated lidar ratio that is suitable for use in the Fernald method. The fullmonty.cpp code performs exactly the same task as the minimie.cpp code except that it generates 10 $\times$ 20,000 random distributions and then finds the average distribution. The purpose of this is to increase the statistical validity of

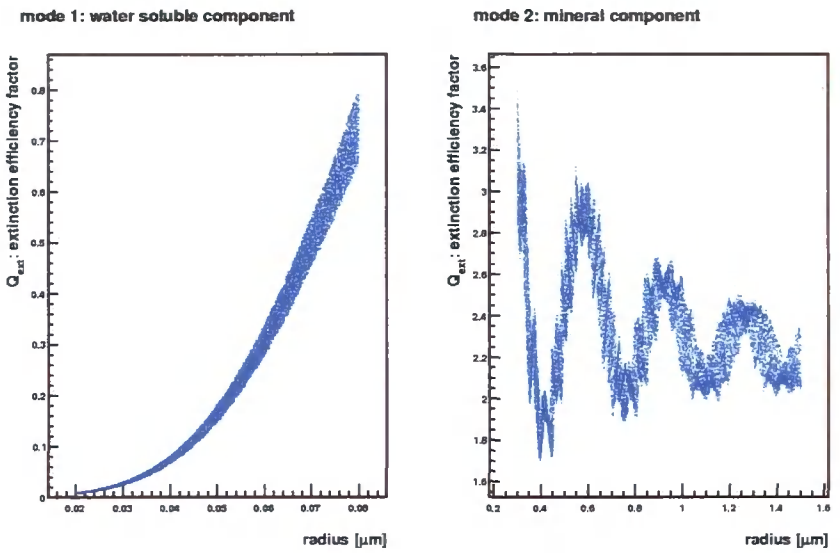

Figure 4.2: The evolution of the extinction efficiency factor with respect to changing radius for an electromagnetic wave incident upon a spherical particle of the bi-modal desert dust aerosol. The radius and optical properties of the spherical particle are defined by random selection from the desert dust aerosol ranges highlighted in Table 2.2. The bi-modal aerosol is comprised of a water soluble component (left) and a mineral component (right).

the random aerosol generation. Both the minimie.cpp code and the fullmonty.cpp code were executed 10 times and the fullmonty.cpp results have been quoted in this thesis. The minimie.cpp code produces a lidar ratio of approximately 29 $\pm$ 3 steradians and the fullmonty.cpp code also produces a lidar ratio of approximately 29 $\pm$ 3 steradians. This value has been used for both the revised Klett solution and the Fernald algorithm.

4.2 Lidar Analysis

This section discusses the analysis of data obtained using a single-scattering monostatic lidar located at the H.E.S.S. site in Namibia. Each lidar analysis

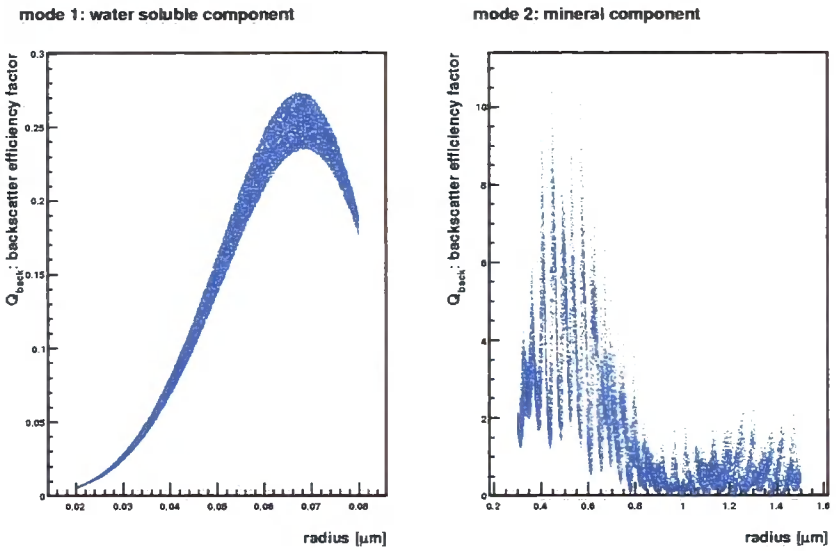

Figure 4.3: The evolution of the backscatter efficiency factor with respect to changing radius for an electromagnetic wave incident upon a spherical particle of the bi-modal desert dust aerosol. The radius and optical properties of the spherical particles are defined by random selection from the desert dust aerosol ranges highlighted in Table 2.2. The backscatter efficiency factor is the scattering efficiency at the backscattering angle of 180 degree. The bi-modal aerosol is comprised of a water soluble component (left) and a mineral component (right).

method presented in Chapter 3 was implemented in the form of a computer programme using the C++ object-orientated programming language including many library functions from the ROOT (version 5.14) object-orientated data analysis framework. In total, four computer programmes were written for each of the methods outlined in Chapter 3, namely klett.cpp, revklett.cpp, fernald.cpp and multiangle.cpp. All of these programmes are included on the compact disc attached to this thesis.

Measurements of the local atmosphere at the H.E.S.S. site in Namibia were recorded on 1st July 2008 using the Easy-Lidar ALS450XT. For the Klett and Fernald methods the lidar was pointed to the zenith and 10 profile runs of 600 laser

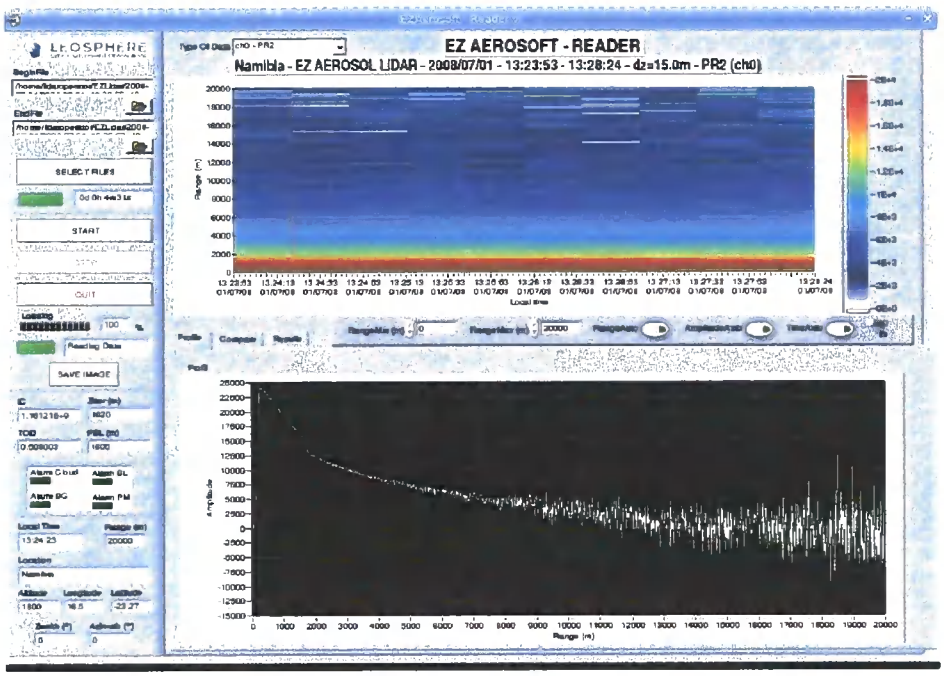

Figure 4.4: Shown here is a "screen-shot" of the Easy-Lidar ALS450XT interface. This screen-shot represents data taken at the H.E.S.S. site in Namibia on 1st July 2008. The top profile illustrates the intensity of scatterers versus range over a 5 minute period. This profile suggests the atmosphere was stable over the measurement period. The bottom profile shows the amplitude of the lidar return signal versus range for a single run of 600 shots. The gradient change at a range of approximately 2 km suggests the location of the planetary boundary layer. Beyond a range of 15,000 m the lidar return signal appears to reduce to noise.

shots were recorded. Figure 4.4 is a "screen-shot" of the Easy-Lidar ALS450XT interface. The profile in Figure 4.4 demonstrates the amplitude of the lidar return signal versus range.

The top profile in Figure 4.4 shows the intensity of scatterers versus range over a period of 5 minutes. This profile suggests that the atmosphere was stable over the duration of the measurements. The bottom profile in Figure 4.4 shows the amplitude of the lidar return signal versus range for a single run of 600 laser

shots. The change in gradient at $\pm$ 2 km appears to illustrate the location of the planetary boundary layer. Beyond a range of 15,000 m the amplitude of the return signal appears to deteriorate to noise. In summary it can be concluded that, on the 1st July 2008, the local atmosphere at the H.E.S.S. site was stable over the 5 minute period of lidar measurements.

4.2.1 The Klett Method

This section discusses the results of the klett.cpp computer programme which is an implementation of the Klett method. Firstly the lidar return signal was range-corrected and normalised according to the peak amplitude value $P_0 \approx 25{,}000$ (see Figure 4.4). Then the natural logarithm was calculated in order to create the convenient S-function, as shown in Equations 3.3 and 3.4. Figure 4.5 illustrates the newly created S-function for the the range of interest.

In addition to the power return signal, the instrument's software written by the lidar's manufacturer generates a profile of extinction coefficients (α) that can be used to estimate the transmission. The extinction profile produced by the instrument is illustrated in Figure 4.6. At the time of this analysis, the lidar was not generating a profile of backscatter coefficients with enough significant figures useful for analysis and comparison with the backscatter profiles shown in this thesis. Thus the backscatter profiles generated in this research cannot be compared with an independent measure and as such can only be taken at face value. Despite this, the main goal of this research with respect to very high energy gamma ray astronomy, is to explore the transmission probabilities useful for the IACT. Therefore a lack of independently measured backscatter coefficient

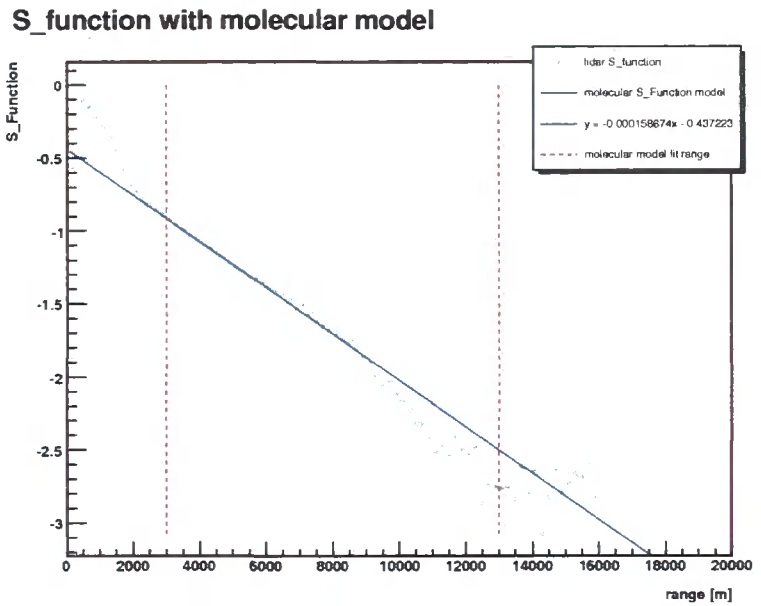

Figure 4.5: The lidar S-Function used in the Klett method (stars). This is simply the natural logarithm of the normalised range corrected lidar power return signal. The S-function clearly highlights the planetary boundary layer where there is a gradient change at a height of approximately 2 km. Also shown here is the molecular S-Function model (straight line) used in the Fernald method Section 4.2.2.1.

values did not hinder the progress of this research.

In accordance with the Klett method detailed in Section 3.2, a profile of extinction coefficients (α) was generated by implementing Equation 4.1 i.e. Klett's solution to the Bernoulli differential Equation 3.7.

$$\alpha(r) = \frac{exp\left[\frac{S(r) - S_0(r)}{k}\right]}{\alpha_0^{-1} - \frac{2}{k}\int exp\left[\frac{S(r) - S_0(r)}{k}\right] dr'} \tag{4.1}$$

The assumed values chosen were k = 1 for the exponent and $\alpha_0 = 0.03$ m^{-1} for the far end boundary extinction value. These were the same values used by

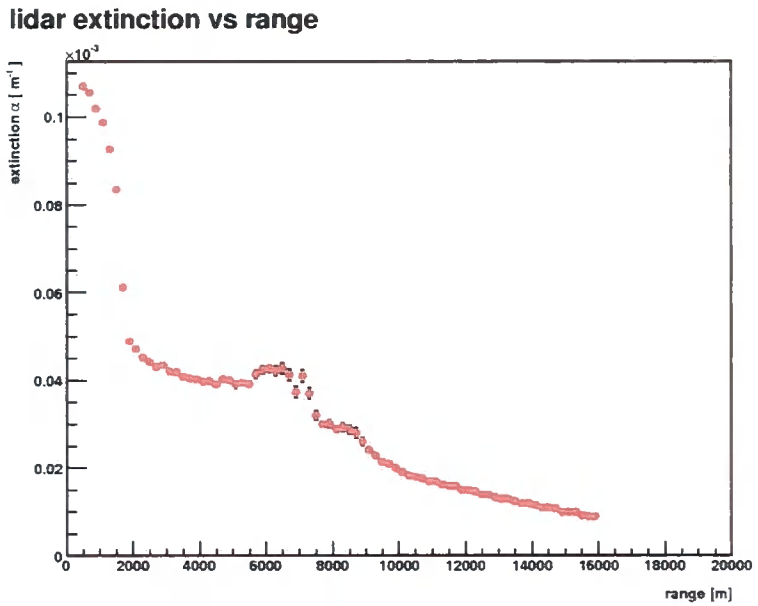

Figure 4.6: The profile of extinction coefficients generated by the Easy-Lidar ALS50XT. The greater amount of extinction due to aerosols present in the planetary boundary layer is clear below a height of approximately 2 km. There also appears to a volume of scatterers between 5 km and 8 km.

Carnuth & Reiter [15] in their implementation of the Klett method. Figure 4.7 illustrates the resulting profile of extinction coefficients.

Figure 4.7 shows that the Klett solution returns extinction values in the same range as that generated by the lidar. However, unlike the extinction profile shown in Figure 4.6, Figure 4.7 shows a much smoother function. This is most likely due to the process of using the natural logarithm of the normalised power return signal. The klett.cpp computer programme integrates these calculated extinction coefficients to find the optical depth τ as shown in Equation 2.5, then finds the exponential of the negative optical depth values to estimate the probability of transmission as shown in Equation 2.6. Using the lidar generated extinction coefficient values the lidar probability of transmission was calculated using the

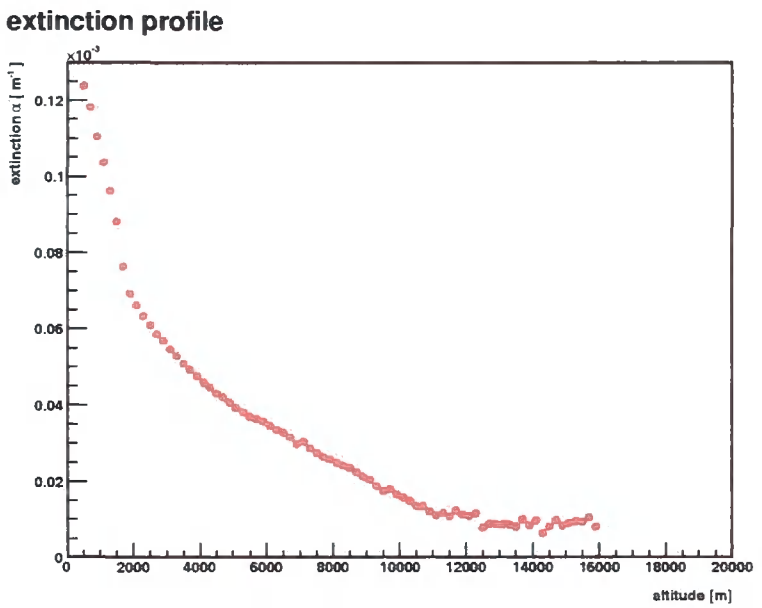

Figure 4.7: The profile of extinction coefficients calculated by implementing the Klett solution for extinction. This profile demonstrates that by implementing the Klett method it is possible to reproduce an extinction profile similar to that given by the instrument in Figure 4.6. Again, the greater amount of extinction due to the presence of aerosols is visible below a range of approximately 2 km.

same approach. These two probability of transmission curves were then plotted together as illustrated in Figure 4.8.

Figure 4.8 suggests that the probability of transmission calculated using the Klett method is in good agreement with that obtained from the lidar generated extinction coefficients. This suggests that the instrument has employed a similar method to the Klett method in order to derive its extinction coefficients. However, the Klett method comes with a number of assumptions including that of a power law relationship between extinction and backscatter. Thus the solutions under the Klett method are sensitive to the values chosen for the exponent (k) and the far-end boundary extinction value (α_0). Figure 4.7 has no error bars

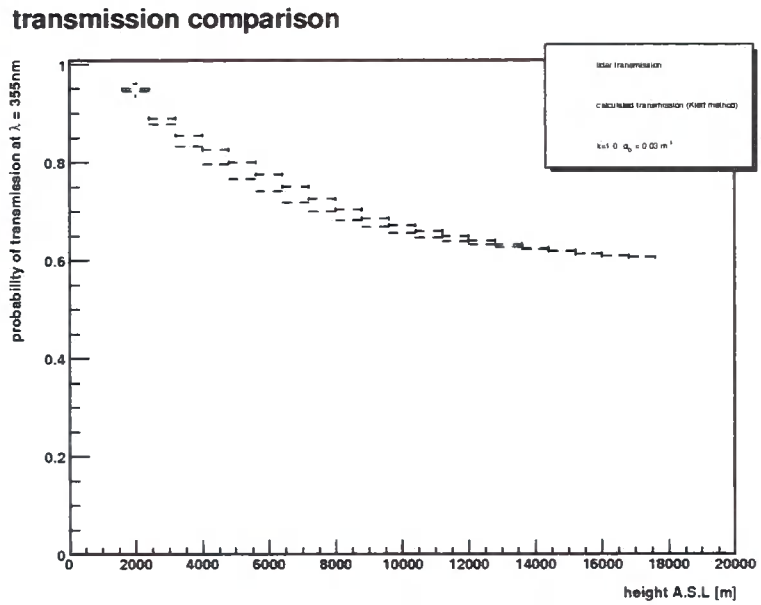

Figure 4.8: The estimated probability of transmission of an electromagnetic wave of wavelength $\lambda = 355$ nm through the lower 18 km of the atmosphere. The lidar generated transmission (circles) is compared to the transmission estimated following the Klett method (stars). It is clear from this plot that the Klett method is in good agreement with that of the lidar.

because the error is dominated by the systematic error associated with choosing the appropriate values for these two assumed values under the Klett method. Thus error bars on the extinction profile are meaningless in terms of describing the accuracy of the result. Instead a more meaningful exercise is to demonstrate the sensitivity of the extinction result by choosing different values of either k or α_0.

Figure 4.9 illustrates the sensitivity of the Klett extinction solution to the far-end boundary extinction value. The process of altering the far-end boundary value only has a very small effect on the deviation of the extinction coefficient from its initial value. Section 3.2 suggested that it is better to over-estimate α_0 and

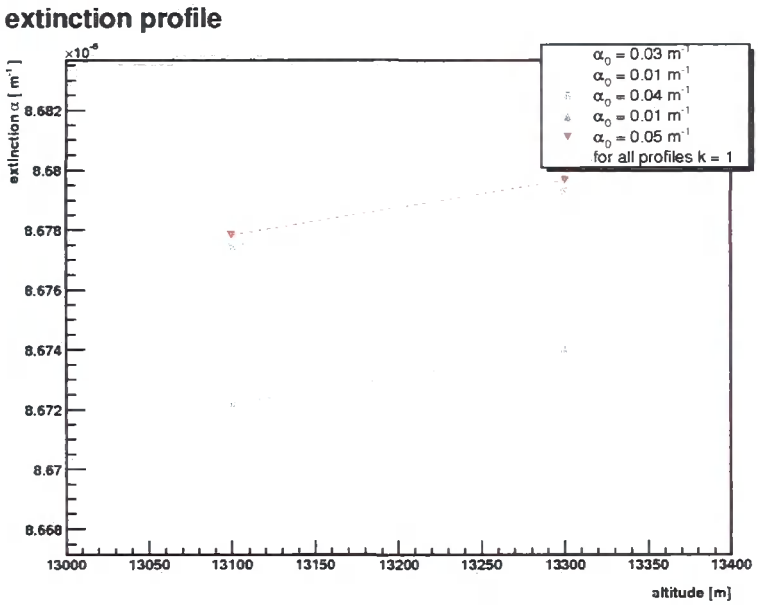

Figure 4.9: Sensitivity of the Klett method derived extinction coefficients to different far-end boundary values (α_0). This figure shows that changing the far-end boundary value has a small effect on the resulting extinction coefficient. To see any effect we have to analyse a magnified section of the extinction coefficient versus range. Shown here are two points on the extinction coefficient profiles for different values of α_0. To illustrate the problem we assume that the correct value of $\alpha_0 = 0.03$ m^{-1}. The effect on the derived extinction coefficients as a result of choosing a different α_0 is clearly visible and, as this graph suggests, it is better to overestimate the far-end boundary value rather than underestimate it. The deviation of the extinction coefficient solution using the assumed correct α_0 value is much smaller for over-estimated α_0 values compared to under-estimated α_0 values.

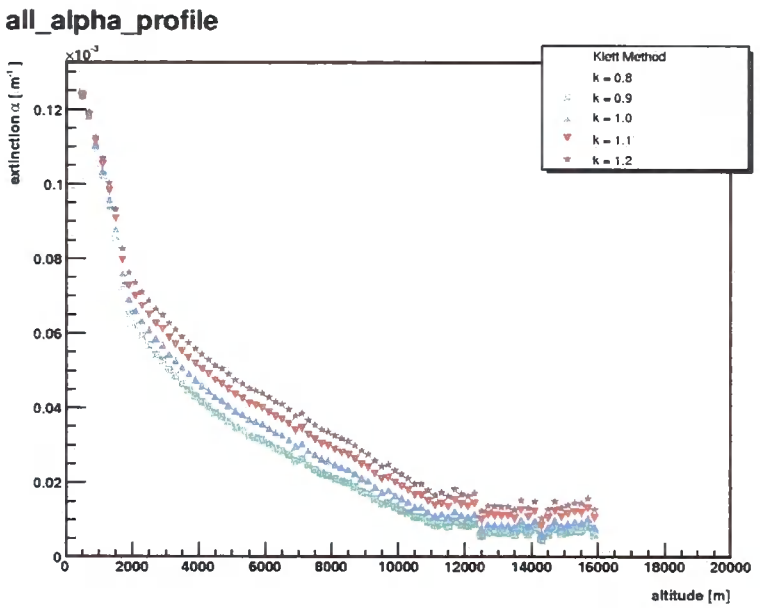

Figure 4.10: Sensitivity of the Klett method derived extinction coefficients to different exponent (k) values. It is clear that altering the value of k by small amount has a large effect on the resulting extinction solution.

Figure 4.9 confirms this recommendation, as deviations from the correct extinction coefficients are much smaller for over-estimated far-end boundary values compared to those for under-estimated far-end boundary values.

The process of altering the value chosen for the exponent (k) appears to have a much greater effect on the solution of the extinction coefficient as expected. Figure 4.10 illustrates the sensitivity of the extinction coefficient to a varying exponent k. Figure 4.10 clearly shows that altering the value of k by a very small amount translates into a big difference between extinction profiles.

Therefore the solution of the extinction coefficients using the Klett method is subject to error if an inappropriate value for the exponent k is used. Hence these errors can also be carried forward to the resulting probability of transmission

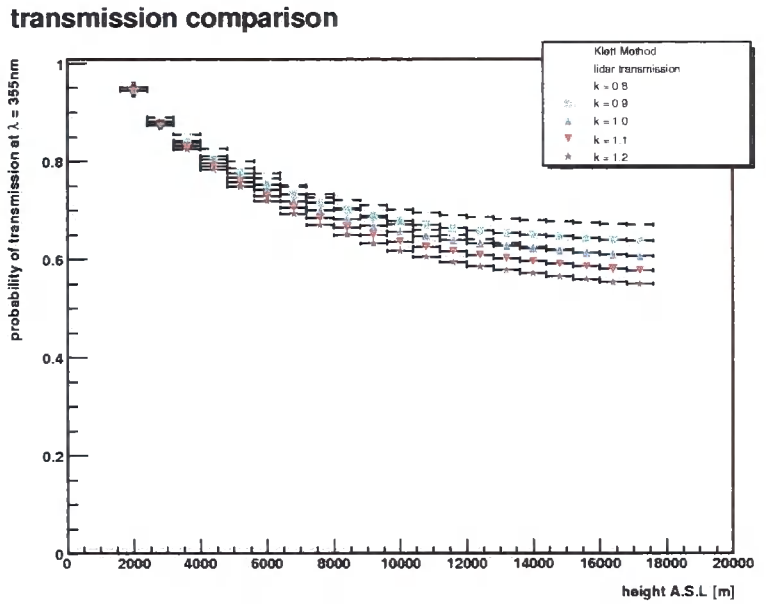

Figure 4.11: The probability of transmission for $\lambda = 355$ nm using different values for the exponent k. It is clear that altering the value of k by a small amount has a large effect on the resulting probability of transmission profile, especially at higher altitudes and importantly in the region where gamma ray induced Cherenkov air showers reach their maximum i.e. $\pm$ 10 km.

as illustrated in Figure 4.11. The Monte Carlo numerical method discussed in Section 4.1 can be used to determine the functional relationship between backscatter and extinction coefficients. If this relationship can be represented by a power law then the appropriate value of k can be found. The correct value of α_0 cannot be measured accurately as already discussed in Section 3.2.

4.2.2 The Fernald Method

The Fernald method tries to improve upon the Klett method by distinguishing between the effect of background molecular scattering and that due to aerosols. Thus implementation of the Fernald method provides an opportunity to see if the probability of transmission can be improved relative to the Klett method. Two different approaches were taken in order to obtain the backscatter coefficient following the Fernald method; firstly the backscatter coefficient was calculated using the Fernald algorithm highlighted in Equations 4.2 and 4.3;

$$\beta_A(r) = \frac{P(r)r^2 exp\left[\xi(u)du\right]}{\frac{P(r_m)r_m^2}{\beta_A(r_m)+\beta_M(r_m)} + 2\int_r^{r_m} L_A(v)P(v)v^2 exp\left[\xi(u)du\right]dv} - \beta_M(r) \tag{4.2}$$

$$\xi(u) = 2\int_r^{r_m}\left[L_A(u) - L_M\right]\beta_M(u)du \tag{4.3}$$

secondly the backscatter coefficient was calculated by implementing the revised Klett solution highlighted in Equation 4.4:

$$\beta(r) = B_A\alpha_A(r) + B_M\alpha_M(r) \tag{4.4}$$

4.2.2.1 Background Molecular Extinction and Backscatter

Before discussing the results of the Fernald algorithm and the revised Klett solution, this section discusses how the background molecular extinction and

backscatter coefficients were calculated. The Fernald method assumes that these two values are known and are readily available using standard atmospheric data like that presented in Section 2.2.1. This research uses data from the MODTRAN tropical model atmosphere. From MODTRAN it is possible to retrieve the probability of transmission for a pure molecular atmosphere as described by the tropical atmospheric model, see Section 2.2.1. A power-law was then fitted to the transmission profile as expressed in Equation 4.5.

$$y(x) = (1.14117) \times x^{-0.0189} \tag{4.5}$$

Then using Fernald's two-way transmission defined in Equation 3.15, it is possible to derive the molecular extinction and backscatter coefficients using the one-way representation as follows:

$$\begin{aligned} T_M(r) &= exp\left[-\int_0^r \alpha_M(r)dr\right] \\ ln\left[T_M(r)\right] &= -\int_0^r \alpha_M dr \\ \alpha_M(r) &= -\frac{1}{T_M(r)}\frac{dT_M(r)}{dr} \end{aligned} \tag{4.6}$$

Then using the relationship defined in Equation 3.13, the molecular backscatter was derived. Figures 4.12 and 4.13 illustrate the results of the MODTRAN tropical model derived molecular extinction and backscatter coefficients. As expected, the extinction coefficient is larger than the backscatter coefficient.

An alternative method for determining the background molecular extinction and

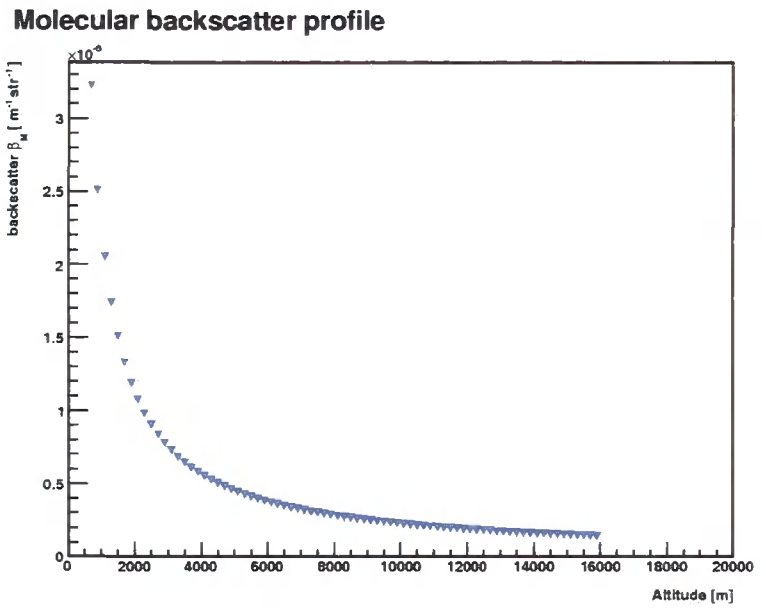

Figure 4.12: The profile of the background molecular backscatter coefficients derived using the MODTRAN tropical atmospheric model.

backscatter coefficients was also implemented. The second approach was done by fitting a straight line to a stable region of the lidar S-function. A stable region of the lidar S-function is determined where the lidar return signal has little or no aerosol scattering, and before the lidar return signal deteriorates to noise. It is assumed that this region lies between 3000 m and 13,000 m, highlighted in Figure 4.5. The straight line function, as illustrated in Figure 4.5, was extrapolated forwards and backwards to cover the full range of the lidar. This newly-fitted straight line function now represents the linear S-function, which is the lidar return signal that would be expected if the atmosphere were wholly molecular. The Klett method detailed in Section 3.2 was then applied to the linear S-function to calculate the molecular extinction coefficient. Once the extinction coefficient was determined the relationship defined by Equation 4.4 was applied to calculate

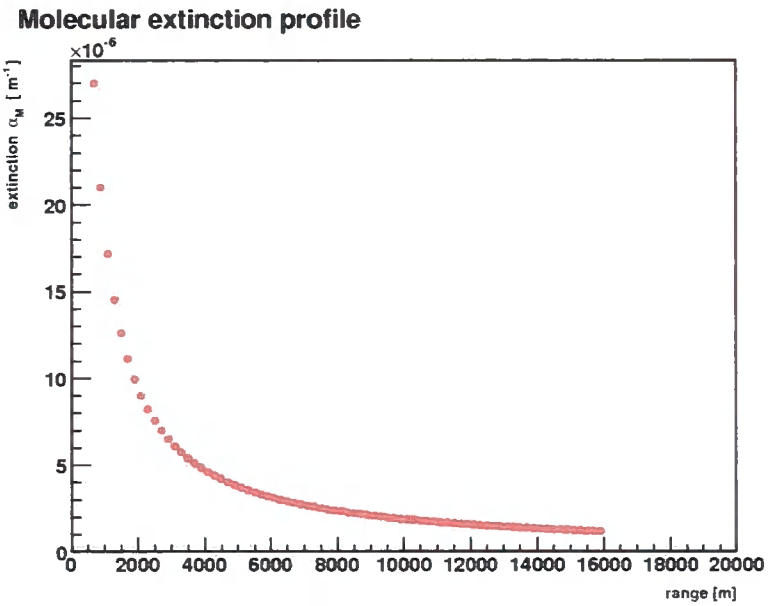

Figure 4.13: The profile of the background molecular extinction coefficients derived from the MODTRAN tropical atmospheric model.

the molecular backscatter coefficient.

The molecular extinction coefficients calculated using this method were integrated to estimate the optical depth. The exponential of the negative optical depth value was then calculated to determine the probability of transmission for a background of molecular scatterers. Figures 4.16 and 4.21 both illustrate the lidar-derived background molecular transmission, and it is clear that they are both in good agreement with the MODTRAN tropical model-derived transmission values. This method suggests that the linear response of the lidar is calibrated very closely to that of the MODTRAN tropical model atmosphere. The lidar derived molecular transmission values are expected to have systematic errors inherited from the Klett method used to calculate these values.

This second method is a useful way to determine the background molecular

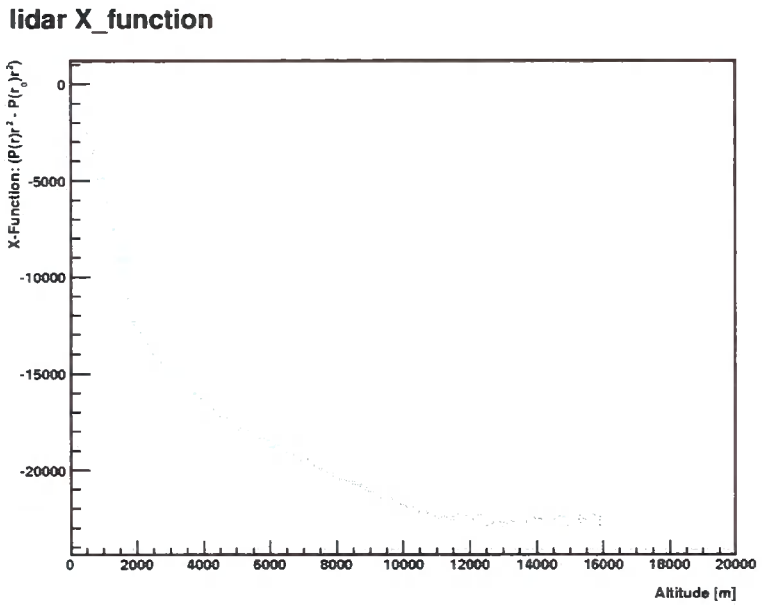

Figure 4.14: The normalised linear X-Function used when implementing the Fernald algorithm. The linear function avoids possible over smoothing effects associated with using the S-Function.

component if MODTRAN models are not available, or at least to unveil the background molecular component that is "seen" by the lidar.

4.2.2.2 The Fernald Algorithm

The computer programme fernald.cpp implements the Fernald algorithm. Unlike the Klett method, the Fernald algorithm does not use an S-function, but instead uses the linear X-function, as discussed in Section 3.3.1. Figure 4.14 illustrates the lidar X-function used for implementing the Fernald algorithm.

In order to solve Equations 4.2 and 4.3 the fernald.cpp computer programme uses the X-function with the constant aerosol lidar ratio and the molecular lidar ratio. The value used for the aerosol lidar ratio was 29 steradians (see Section 4.1) and

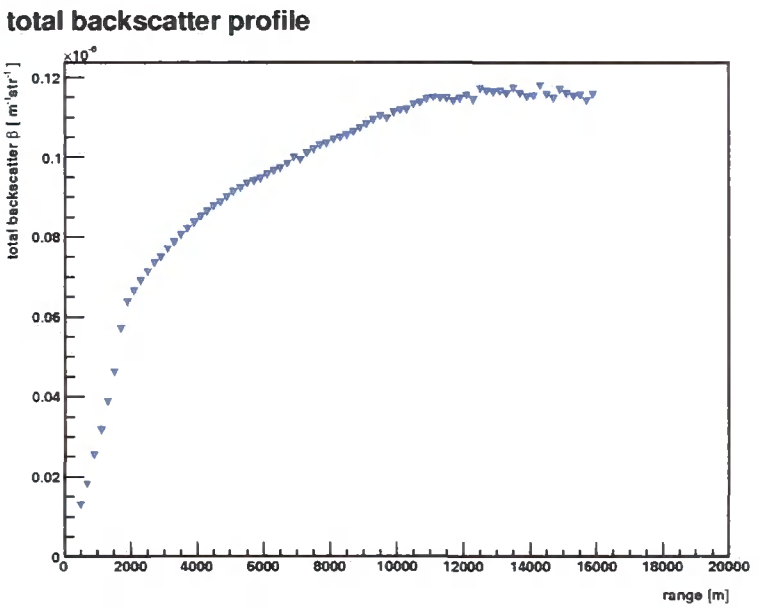

Figure 4.15: The inverted profile of the total backscatter coefficients calculated using the Fernald algorithm.

the value used for the aerosol backscatter coefficient at the far-end range was zero because the number of aerosols present at the far-end range is expected to be negligible. Figure 4.15 illustrates the inverted total backscatter coefficient calculated using the Fernald algorithm.

The aerosol backscatter coefficient was then calculated by subtracting the derived molecular backscatter coefficient from the total backscatter coefficient, see Equation 3.9. The aerosol extinction coefficient was calculated by multiplying the aerosol lidar ratio and the aerosol backscatter coefficient together as defined by the relationship highlighted in Equation 3.12. Finally, the aerosol extinction coefficient was integrated to find the optical depth and the exponential of the negative optical depth value was calculated to produce the probability of transmission at the lidar wavelength $\lambda = 355$ nm. Figure 4.16 illustrates the proba-

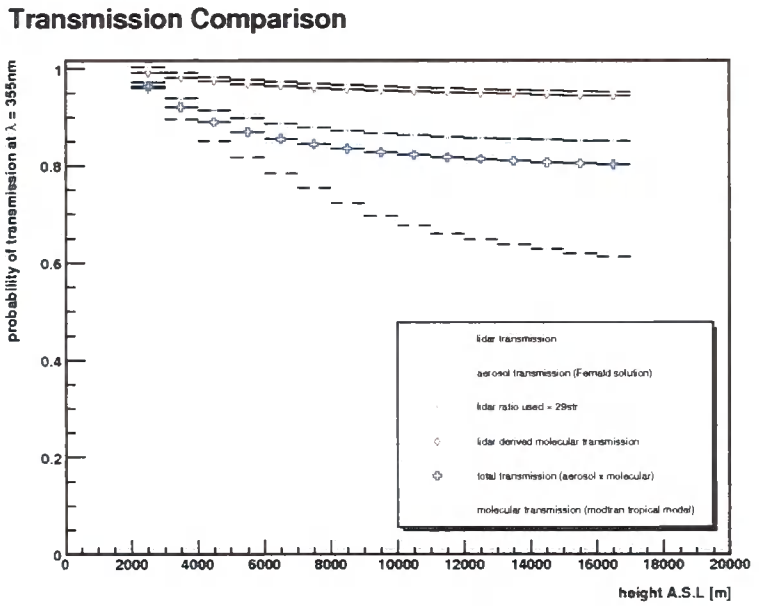

Figure 4.16: The aerosol, molecular, total and lidar probability of transmission at wavelength $\lambda = 355$ nm. These were calculated under the Fernald method using the Fernald algorithm. Using a constant lidar ratio of 29 steradians results in a higher probability of transmission compared to that generated by the lidar. This is clear above the planetary boundary layer.

bility of transmission at lidar wavelength $\lambda = 355$ nm. The total probability of transmission is the product of the respective molecular and aerosol probabilities.

Figure 4.16 shows that using the Fernald algorithm with a lidar ratio of 29 steradians results in a higher probability of transmission for $\lambda = 355$ nm compared to that generated by the lidar. This is most noticeable above the planetary boundary layer.

4.2.2.3 Klett's Revised Solution

The computer programme revklett.cpp implements the revised Klett solution to the backscatter coefficient as required by the Fernald method. As outlined by

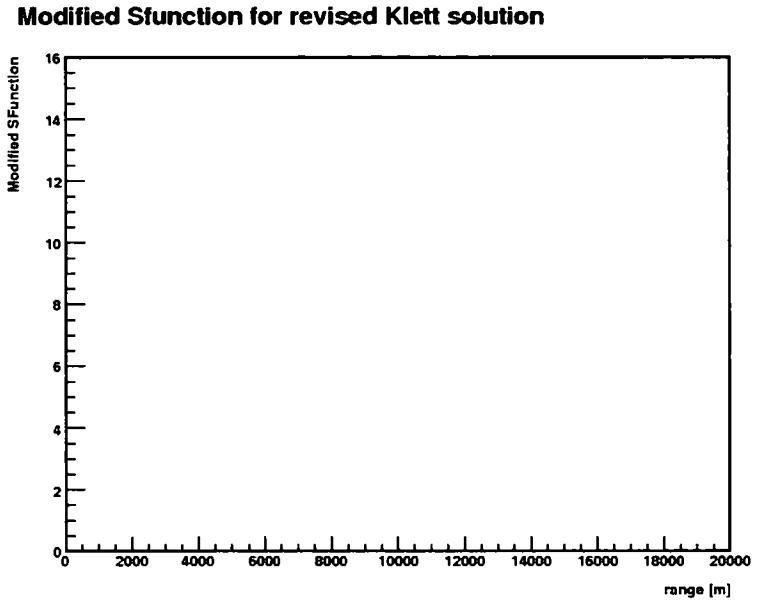

Figure 4.17: The modified S-function required in order to solve for the backscatter coefficient using the revised Klett solution.

the revised Klett method in Section 3.3.2 the background molecular backscatter coefficient was used to calculate the modified S-Function shown in Equation 3.20.The inverse molecular lidar ratio was calculated by using the inverse of the relationship shown in Equation 3.13 and the inverse aerosol lidar ratio used was $\frac{1}{29}$ steradians^{-1}. Figure 4.17 illustrates the modified S-function.

The modified S-function was then used to solve Equation 4.4, the total backscatter coefficient, as stated by Klett's revised solution to the new Bernoulli differential equation highlighted by Equation 3.21. The inverse aerosol lidar ratio used for Equation 4.4 was $\frac{1}{29}$ steradians^{-1}. The backscatter contribution at the far-end range due to aerosols is considered to be negligible, as the presence of aerosols rapidly decreases above the PBL, and the total backscatter coefficient at the far-end range is expected to be dominated by molecular contributions.

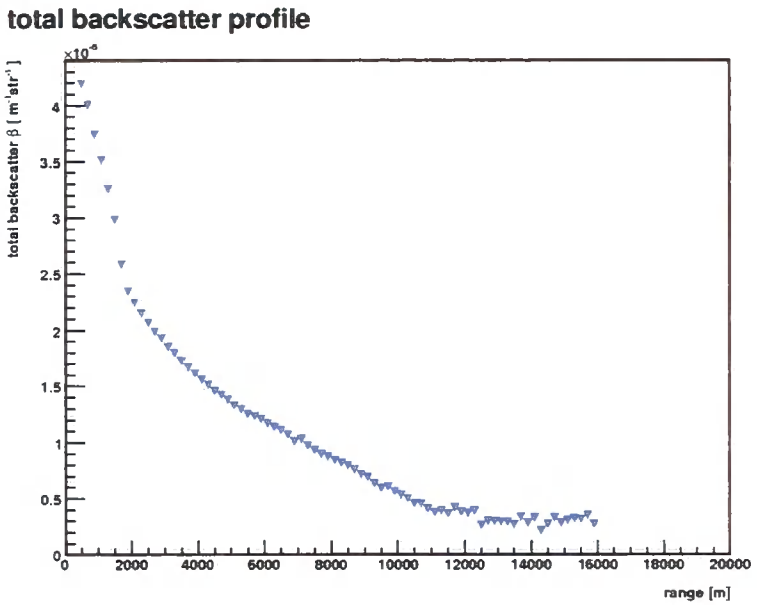

Figure 4.18: The profile of the total backscatter coefficients calculated under the Fernald method using the revised Klett solution.

Therefore the backscatter coefficient at the far-end boundary range that was used in Equation 4.4 was the derived molecular backscatter coefficient at the far-end boundary range ($\beta_m^{-1} \approx 0.1 \times 10^{-6}$ m^{-1} steradians) as shown in Figure 4.12.

Figure 4.18 illustrates the profile of the total backscatter coefficients calculated using the revised Klett solution, Equation 4.4. Then using the relationship outlined in Equation 3.23, the aerosol backscatter coefficient was calculated by subtracting the molecular backscatter coefficient from the total backscatter coefficient. Figure 4.19 illustrates the aerosol backscatter coefficients calculated using the revised Klett solution.

The aerosol backscatter coefficients and the derived molecular backscatter coefficients were used to calculate the aerosol extinction coefficients. This was

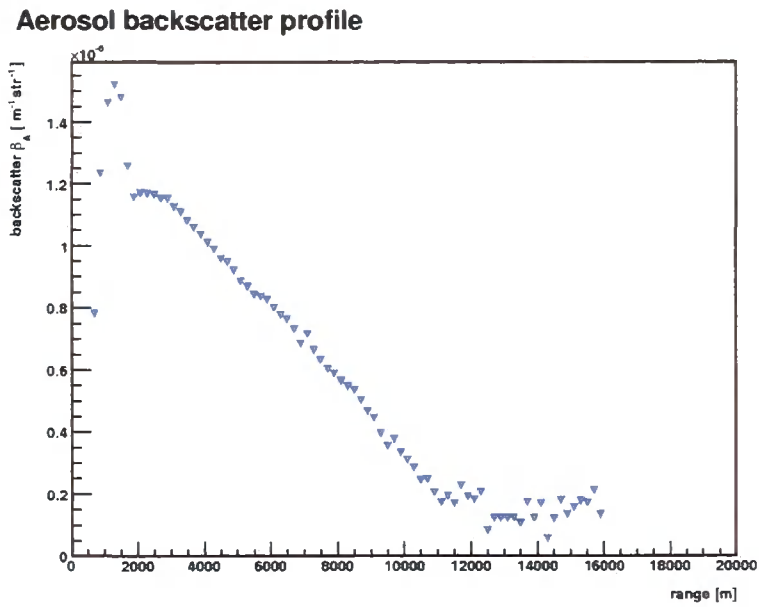

Figure 4.19: The profile of aerosol backscatter coefficients calculated using the revised Klett solution.

done using the relationships stated in Equations 4.4 and 3.23. The revised Klett solution also used a constant aerosol lidar ratio of 29 steradians and a molecular lidar ratio of $\frac{8\pi}{3}$ steradians. As expected the aerosol extinction coefficients are much greater than the molecular extinction coefficients; Figure 4.20 illustrates the profile of the calculated aerosol extinction coefficients. The figure shows the aerosol extinction coefficients to be 3 orders of magnitude greater than the aerosol backscatter coefficients.

Once again these extinction coefficients were integrated to estimate the aerosol optical depth. The aerosol probability of transmission was then calculated using the exponential of the negative optical depth values. The total probability of transmission was estimated by finding the product of the molecular and aerosol probabilities of transmission. Figure 4.21 illustrates the respective probabilities

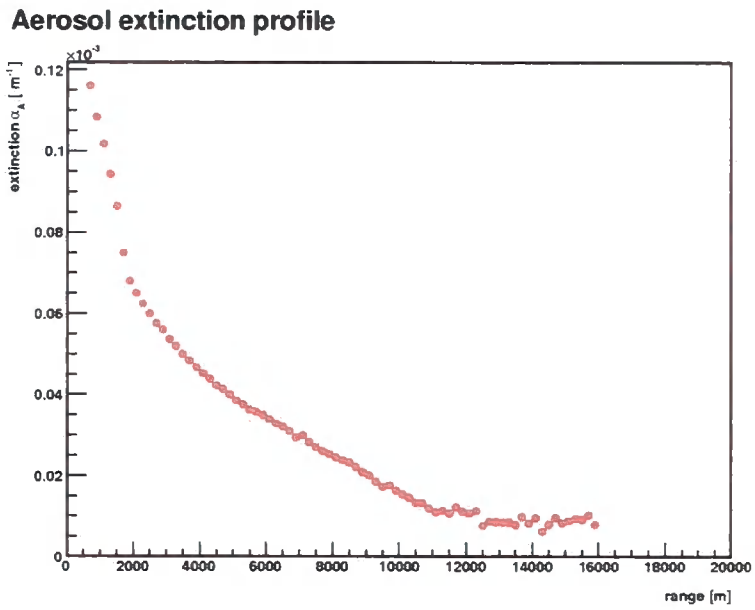

Figure 4.20: The profile of the calculated aerosol extinction profiles using the revised Klett solution. As expected the aerosol extinction coefficients are approximately 3 orders of magnitude greater than the aerosol backscatter coefficients.

of transmission calculated using the revised Klett solution at the lidar wavelength of $\lambda = 355$ nm.

Figure 4.21 suggests that the revised Klett method is in good agreement with the lidar generated probability of transmission. Again, this suggests that the lidar manufacturer employed the Klett method.

4.2.2.4 Fernald Method Errors and Comparisons

Section 4.2.1 discussed the errors associated with using the Klett method in order to solve for the extinction coefficients. Similarly this section discusses the main source of error associated with using the Fernald method. Systematic errors associated with choosing an appropriate molecular atmospheric model as well as

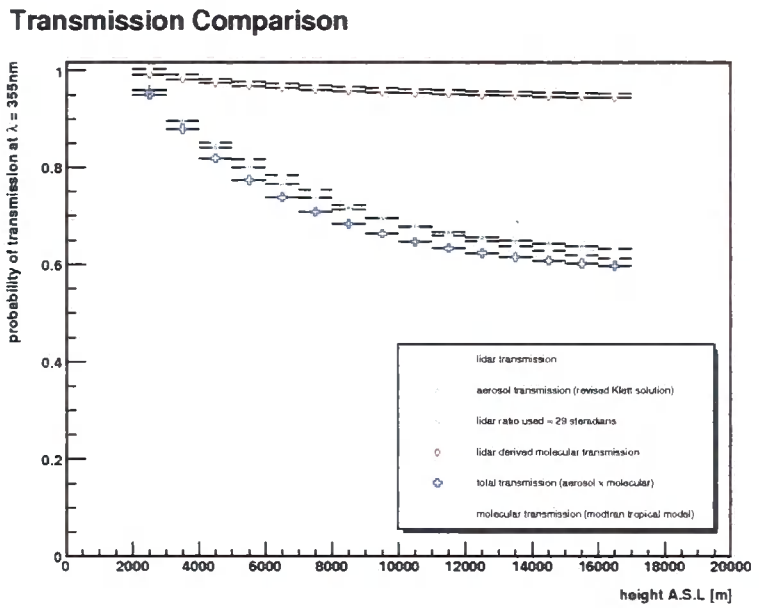

Figure 4.21: The aerosol, molecular, total and lidar probability of transmission at a wavelength of 355 nm. The aerosol and molecular transmissions were calculated using the revised Klett solution with a constant aerosol lidar ratio of 29 steradians.

assuming the lidar ratio remains constant for all altitudes means that, like the Klett method, the Fernald method is also subject to systematic errors. Clearly the assumption that the lidar ratio remains constant for all altitudes is not a reasonable one. Hence completing the Fernald method with a varying lidar ratio is the preferred approach and it is recommended that this be done in future lidar analysis.

Comparison of Figure 4.21 and Figure 4.16 suggests that the Fernald algorithm results in a higher probability of transmission compared to that returned by the revised Klett solution, which is in closer agreement with the lidar generated probability of transmission.

This is confirmed in Figure 4.22, which compares the total probability of trans-

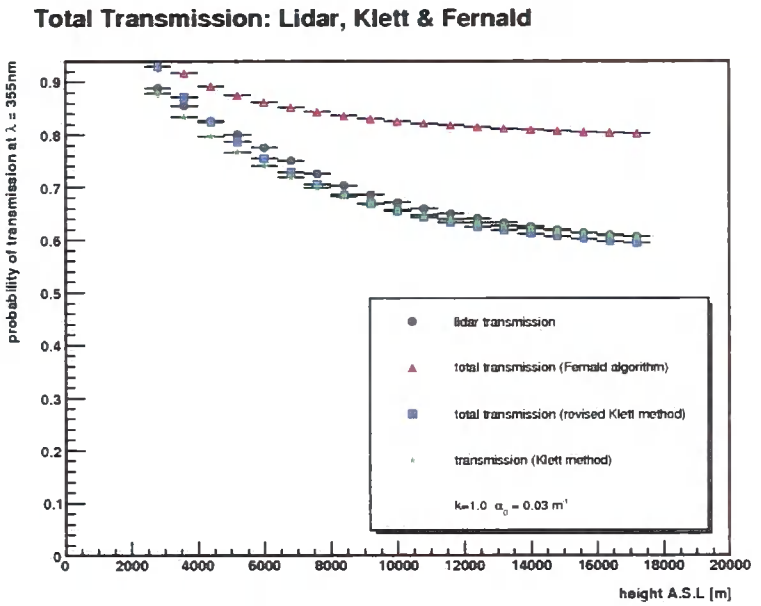

Figure 4.22: The total probability of transmission at a wavelength of 355 nm for the lidar, the Klett method, the Fernald algorithm and the revised Klett method. This figure shows that the probability of transmission returned by the lidar as well as that derived using the Klett and revised Klett methods all return similar values. In contrast, the Fernald algorithm returns a higher probability of transmission. It is not known which method is the correct method for the type of atmospheric conditions prevalent at the H.E.S.S. site in Namibia.

mission returned by the lidar as well as that derived using the Klett method, the revised Klett solution and Fernald algorithm. Figure 4.22 illustrates that the Klett and revised Klett methods return similar probability of transmission values to those generated by the lidar. Furthermore, Figure 4.22 clearly shows that the Fernald algorithm returns a higher probability of transmission compared to the other methods. This is despite the fact that both the revised Klett solution and the Fernald algorithm use the same constant aerosol lidar ratio of 29 steradians.

There is no apparent reason for the Fernald algorithm returning higher probability of transmission values other than the intrinsic performance of the respective

algorithms. It is not known which method is the correct method for the type of atmospheric conditions prevalent at the H.E.S.S. site in Namibia. As already suggested above, implementing the revised Klett solution and the Fernald algorithm with a varying aerosol lidar ratio may provide a better understanding as to which solution performs best.

4.2.3 The Multi-Angle Method

The Easy-Lidar ALS450XT is attached to a pan and tilt unit which can steer the instrument both in azimuth and altitude. On 1st July 2008, a set of 5 data-taking runs were completed, with the first set of measurements taken at zenith angle $\theta = 0$ degrees. Lidar measurements were then taken at an altitude of 20 and 30 degrees at a North (0 degrees) azimuth followed by measurements at an altitude of 20 and 30 degrees at a South (180 degrees) azimuth. For each angle of measurement, 10 sets of 600 lidar shots were recorded. Like the previous methods, the multi-angle method was also implemented in the form of a computer programme, multiangle.cpp, which is included on the compact disc attached to this thesis. Figure 4.23 illustrates the combined lidar S-functions generated for each of the angular measurements.

Similarly, the profile of extinction coefficients generated by the lidar are illustrated for each angle of measurement in Figure 4.24. The consistent stacking of the extinction coefficient profiles suggest that there is very little horizontal inhomogeneity in the atmosphere. Thus the multi-angle method prerequisite of horizontal atmospheric homogeneity appears to have been satisfied.

The multi-angle S-functions in Figure 4.24 were used to calculate the vertical

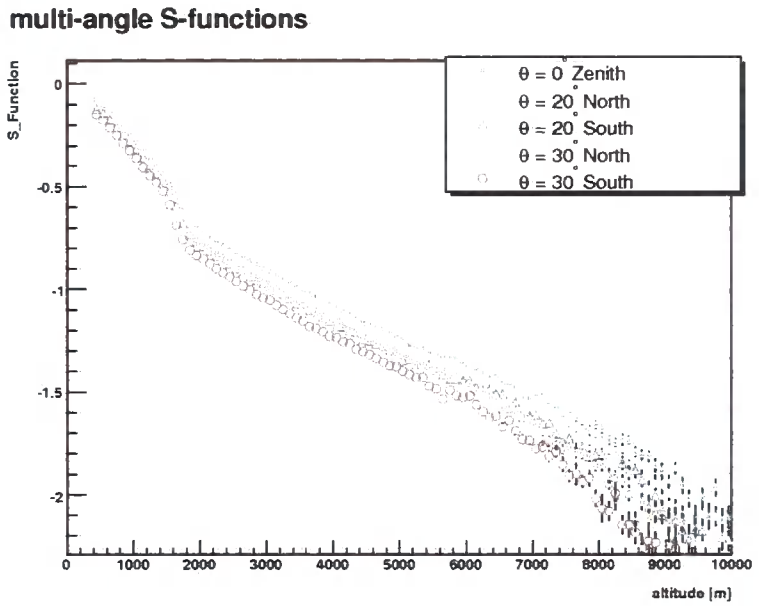

Figure 4.23: The combined lidar S-Function profiles recorded for each angle of measurement. On the 1st July 2008, a set of 5 runs were completed with the first set of measurements taken at zenith angle $\theta = 0$ degrees. Lidar measurements were then taken at an altitude of 20 and 30 degrees in a North (0 degrees) azimuth followed by measurements at an altitude of 20 and 30 degrees in a South (180 degrees) azimuth.

optical depth profile for each angle of measurement, expressed in Equation 3.27. Figure 4.25 shows the averaged vertical optical depths over all measured angles.

Finally, the exponentials of the negative vertical optical depth values were calculated in order to obtain the probability of transmission at the lidar wavelength λ = 355 nm. Figure 4.26 compares the multi-angle method derived probability of transmission versus the lidar generated probability of transmission. Figure 4.26 shows that the multi-angle method results in a lower probability of transmission compared to the lidar generated transmission. Figure 4.26 also shows that the multi-angle probability of transmission rapidly decreases above $\pm$ 7 km. This is an unexpected result because transmission should improve or at least stabilise

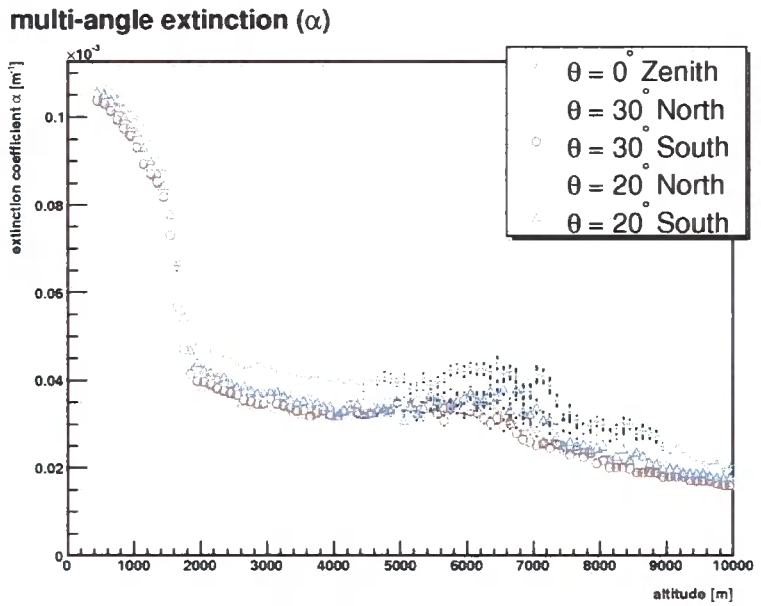

Figure 4.24: The combined profiles of lidar generated extinction coefficients calculated using the multi-angle method. The consistent stacking suggests that the local atmosphere is horizontally homogeneous, or at least, undergoes very little horizontal change.

with increasing altitude due to the lower density of aerosols at these higher altitudes. Therefore it is believed that this drop off is a systematic error resulting from too few measurements at large zenith angles. For the multi-angle method to work effectively a bigger separation between the smallest and largest measured angle is required, possibly >60 degrees. Unfortunately the lidar's range limit of 15 km means that large zenith angle measurements taken using the multi-angle method will not reach the gamma ray induced Cherenkov air shower region because the true altitude is proportional to cos θ (see Figure 3.1). Nonetheless the multi-angle method may prove to perform better at low altitudes within the PBL and further research can be conducted incorporating larger angles to improve the derived probability of transmission at $\lambda = 355$ nm using the multi-angle method.

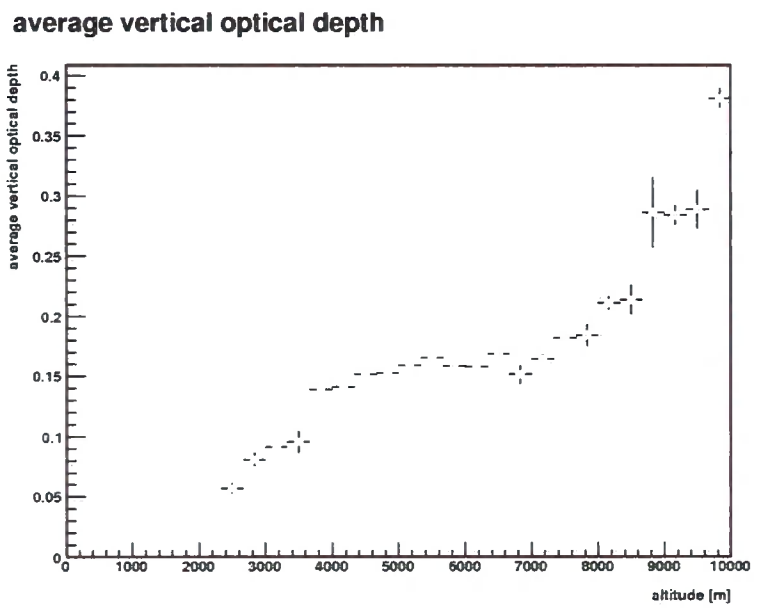

Figure 4.25: The averaged vertical optical depth profile for all measured angles calculated using the multi-angle method.

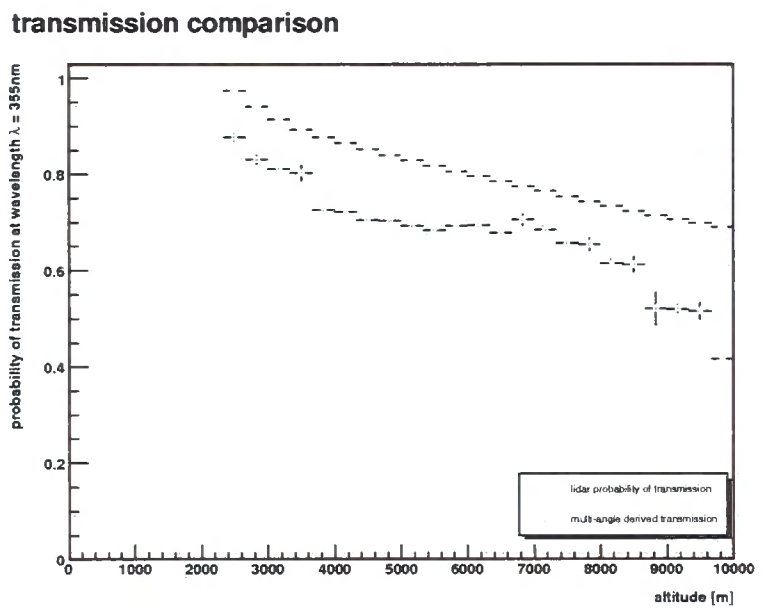

Figure 4.26: The probability of transmission at lidar wavelength $\lambda = 355$ nm calculated using the multi-angle method. The figure suggests that there is a systematic error causing the transmission values above ± 7 km to rapidly deteriorate. It is believed that this systematic error is a result of too small a separation between the smallest and greatest angle of measurement used in this analysis.

4.3 Modelling Extinction versus Backscatter Relationships

Sections 3.5 and 3.6 discussed the need for analysing the functional relationships between the extinction and backscatter coefficients of the desert dust aerosol. The functional relationships that exist between the extinction and backscatter coefficients help to determine the lidar ratio needed for the Fernald method. In addition, this analysis enables the construction of a vertical lidar ratio profile for the H.E.S.S. site in Namibia, which to date, has not been done before.

Section 4.1 discussed the two computer programmes minimie.cpp and fullmonty.cpp written to simulate the aerosol distributions assumed to exist at the H.E.S.S. site in Namibia. As already mentioned, both these codes use a Monte Carlo numerical approach in order to solve for the lidar ratio. However, in solving for a lidar ratio it is also possible to analyse the functional relationships that exist between the aerosol extinction and backscatter coefficients in addition to the lidar ratio itself. In both of these programmes three relationships were analysed:

- extinction versus backscatter
- backscatter versus extinction
- lidar ratio versus extinction

The first relationship looked at was the natural logarithm of the extinction versus backscatter coefficients. The fullmonty.cpp programme was executed ten times and each time consistently returned similar results. The median result is shown

in Figure 4.27 which illustrates the relationship between the natural logarithm of the extinction and backscatter coefficients. A 5th order polynomial represented in Equation 4.7 was fitted to the data with a reduced chi squared test of $\frac{\chi^2}{ndf} = 1.07$.

$$\begin{aligned} ln\alpha = &(-64.773613) + (-13.839700)ln\beta \\ &+ (-0.770258)ln\beta^2 + (0.044827)ln\beta^3 \\ &+ (0.005286)ln\beta^4 + (0.000128)ln\beta^5 \end{aligned} \tag{4.7}$$

This suggests that the model is a good fit with the data and can be used to approximate an extinction coefficient for any given backscatter coefficient so long as it is representative of the aerosols described by the desert dust model.

The second relationship looked at was the inverse of the above i.e. the natural logarithm of the backscatter versus extinction coefficients. Finding a functional relationship linking these two aerosol characteristics is useful due to the lidar not currently generating backscatter coefficients. This particular functional model was applied for convenience as the backscatter coefficients can be found by rearranging the polynomial in Equation 4.7. As before, the fullmonty.cpp programme was executed ten times and each time consistently returned similar results. The median result is shown in Figure 4.28 which illustrates the the natural logarithm of the backscatter versus extinction coefficients. A 5th order polynomial shown in Equation 4.8 was fitted to the data with a resulting reduced chi squared of $\frac{\chi^2}{ndf} = 1.63$.

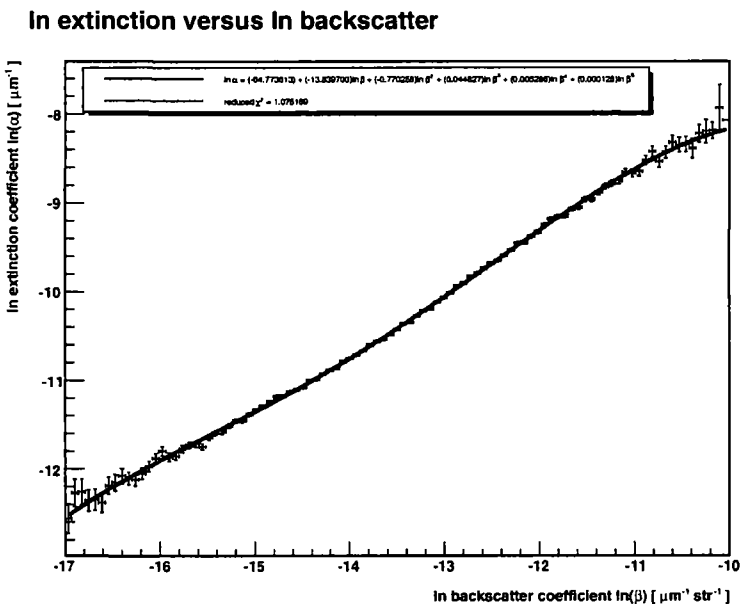

Figure 4.27: The natural logarithm of the extinction versus backscatter coefficients for the desert dust aerosol generated using a Monte Carlo numerical approach. A 5th order polynomial was fitted to the data with a reduced chi square test of $\frac{\chi^2}{ndf} = 1.07$, suggesting a good fit.

$$\begin{aligned} ln\beta = {} & (-54.159199) + (-19.445467)ln\alpha \\ & + (-3.144841)ln\alpha^2 + (-0.213170)ln\alpha^3 \\ & + (-0.005155)ln\alpha^4 + (0.000009)ln\alpha^5 \end{aligned} \tag{4.8}$$

This suggests that the model is a reasonable fit with the data and can be used to approximate the backscatter coefficients by substituting in the lidar generated extinction coefficients.

The final relationship looked at was the lidar ratio versus the natural logarithm of the extinction coefficients. A 6th order polynomial, expressed in Equation 4.9,

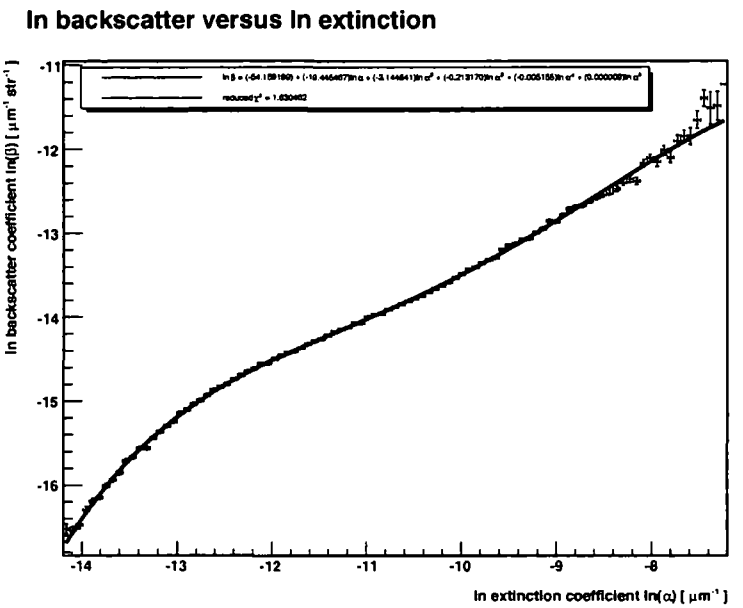

Figure 4.28: The natural logarithm of the backscatter versus extinction coefficients for the desert dust aerosol generated using a Monte Carlo numerical approach. A 5^{th} order polynomial was fitted to the data with a reduced chi square test of χ^2 / ndf = 1.63, suggesting a reasonable fit.

was fitted to the data with a reduced chi squared test of $\frac{\chi^2}{ndf} = 1.45$.

$$\begin{aligned} L(r) = {} & (-19501.240234) + (-10355.157227)[ln\alpha(r)] \\ & + (-2258.544678)[ln\alpha(r)]^2 + (-261.266510)[ln\alpha(r)]^3 \\ & + (-16.962925)[ln\alpha(r)]^4 + (-0.586436)[ln\alpha(r)]^5 \\ & + (-0.008427)[ln\alpha(r)]^6 \end{aligned} \tag{4.9}$$

Where L is the lidar ratio, $\alpha(r)$ the lidar-generated extinction coefficient and r the range or height. This suggests that the model is a reasonable fit with the data and that the model can be used to approximate the lidar ratio for any given

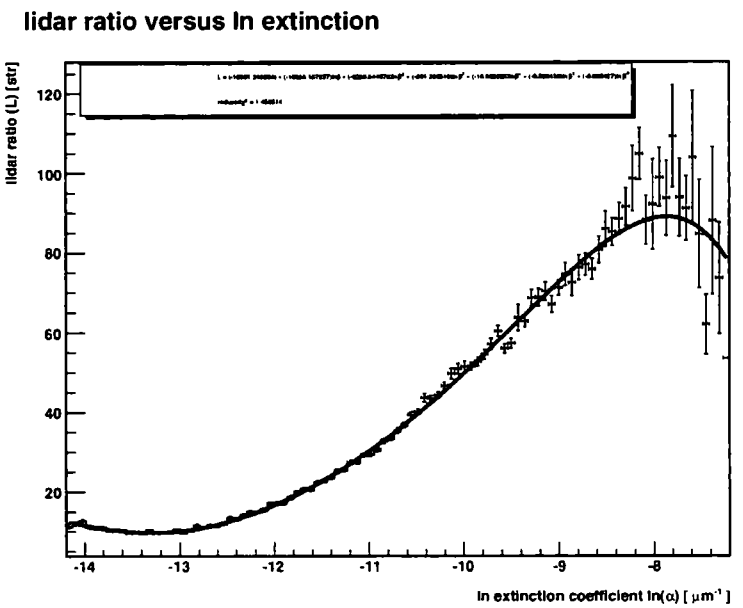

Figure 4.29: The lidar ratio versus natural logarithm of the extinction coefficients for the desert dust aerosol generated using a Monte Carlo numerical approach. A 6^{th} order polynomial was fitted to the data with a reduced chi square test of χ^2 / ndf = 1.45, suggesting a reasonable fit. The model can be used to approximate the lidar ratio for a given extinction coefficient.

extinction coefficient, as long as it is representative of the aerosols described by the desert dust model. Like the two previous models fullmonty.cpp was run three times and produced consistent results each time. The median result is shown in Figure 4.29 which illustrates the the lidar ratio versus the natural logarithm of the extinction coefficients.

The analysis undertaken for this thesis only considers Mie scattering resulting from spherical particles. Furthermore, no empirical evidence exists to confirm that the aerosols present at the H.E.S.S. site in Namibia can actually be described by the desert dust model. Both of these factors will have an impact on the models applied to describe the functional relationships between the extinction

and backscatter coefficients. It is recommended that any future Mie scattering analysis take these two factors into consideration, but until then the results presented in this thesis are a best first order approximation of the Mie scattering effects as applied to the desert dust aerosol model.

4.4 The Vertical Lidar Ratio Profile

Section 4.3 presented a model in Equation 4.9 that can be used to estimate the vertical lidar ratio profile by substituting in the lidar generated extinction coefficients. Figure 4.30 illustrates the vertical lidar ratio profile for the lidar measurements recorded on 1st July 2008. These variable lidar ratios can be used to improve the results of the Fernald method using both the Fernald algorithm and the revised Klett solution.

Figure 4.30 shows that within the PBL the lidar ratio was very high at $\pm$ 70 steradians, but then rapidly decreases to 50 steradians where it stays constant up to an altitude of approximately 8 km. In the height region where Cherenkov air showers reach their maximum, the lidar ratio stabilises near 40 steradians before steadily decreasing above $\pm$ 10 km.

Assuming the applied models are a reasonable representation of the relationship between the extinction and backscatter coefficients, then Figure 4.30 also highlights the need for implementing the Fernald method with a vertical lidar ratio profile. Based on these results, a constant lidar ratio of 29 steradians for the Fernald method is too low and exaggerates the resulting probability of transmission. The accepted lidar ratio values for the desert dust model should fall between 40

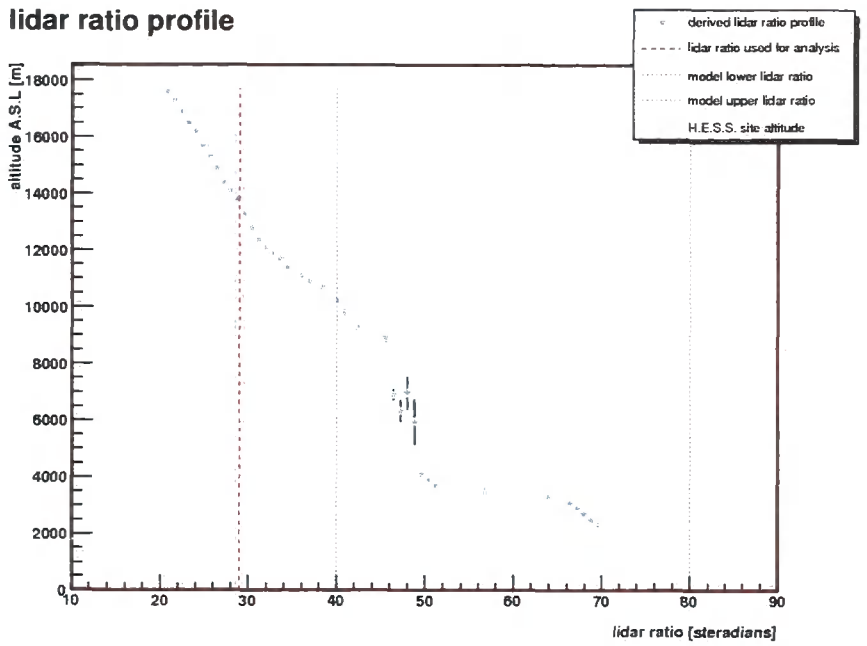

Figure 4.30: The vertical lidar ratio profile. This was calculated by substituting the lidar generated extinction coefficients in to the model expressed in Equation 4.9. The vertical lidar ratio profile provides insight into the atmospheric layers at the H.E.S.S. site and possibly the regions where the gamma ray induced Cherenkov air showers are most readily absorbed or scattered during their propagation to the ground.

and 80 steradians, and this range is also shown in Figure 4.30.

This vertical lidar ratio profile provides insight into the atmospheric layers at the H.E.S.S. site and possibly the regions where the gamma ray induced Cherenkov air showers are most readily absorbed or scattered during their propagation to the ground. The dynamic nature of the atmosphere means that these conclusions are only correct for the time of the lidar measurements. Regular atmospheric lidar measurements of the atmosphere at the H.E.S.S. site may provide a clear indication of the predictable aerosol layers that occur above the site.

Chapter 5

Summary, Recommendations and Future Work

The following chapter provides a summary of the key points discussed in this thesis. In addition, recommendations are made for improving the results presented in Chapter 4. In conclusion, this chapter provides a brief outline of the future work intended to be implemented, not only to improve the results of this research, but to also apply the results to observations of very high energy gamma ray sources with a view to reducing the uncertainty in estimating inferred gamma ray energies.

5.1 Summary

Chapter 1 introduced the field of very high energy gamma ray astronomy within the context of cosmic rays. This included the discussion of the known primary

interactions responsible for the creation and destruction of gamma rays within the Universe. Chapter 1 also discussed how gamma rays incident onto the Earth interact with atmospheric nuclei to produce Cherenkov light which propagates down to the ground. Various atmospheric parameters were highlighted, since the atmosphere has a direct impact on the amount of Cherenkov light available for collecting with ground based telescopes using the imaging atmospheric Cherenkov technique (IACT).

Chapter 2 discussed the structure and composition of the Earth's atmosphere including the different molecular and aerosol models used when conducting atmospheric analysis. The basic principles and theory governing the scattering of light incident onto a particle were discussed, including the Rayleigh and Mie theories widely used to describe the scattering process. In Chapter 2 it was highlighted how two measurable atmospheric quantities, optical depth and the probability of transmission, are key atmospheric parameters required by the IACT Monte Carlo simulations in order to infer the energy of the primary gamma ray photons. The lidar remote sensing technique was discussed as a suitable means of measuring the probability of transmission in the atmosphere over the range from which it is expected that Cherenkov photons, as a result of very high energy gamma ray induced air showers, will propagate.

Chapter 3 introduced various techniques widely used for analysing data recorded with a single-scattering lidar like that used at the H.E.S.S. site in Namibia. Three methods of analysis were discussed; the Klett method, the Fernald method and the multi-angle method. Chapter 3 also discussed how, using Mie theory, a lidar ratio can be calculated for the types of aerosol assumed to occur at the

H.E.S.S site in Namibia. This included how the resulting relationships between the extinction and backscatter coefficients can be analysed in order to generate a vertical lidar ratio profile.

Chapter 4 presented and discussed the author's main body of work which included the results of the Mie scattering analysis and lidar analysis undertaken for this thesis. The Mie scattering analysis was accomplished by implementing a Monte Carlo numerical method, which resulted in an integrated lidar ratio of 29 $\pm$ 3 steradians. Furthermore, the results derived for the probability of transmission (at $\lambda = 355$ nm) using each of the lidar analysis techniques introduced in Chapter 3 were discussed and compared against the results of the lidar manufacturer's closed-source software. The Klett method was found to be in strongest agreement with the probability of transmission calculated by the lidar manufacturer's closed-source software. Finally, Chapter 4 presented and discussed models representing the functional relationships between the extinction and backscatter coefficients derived for aerosols described by the desert dust aerosol model. This included a model that can be used with lidar measured extinction coefficients to generate a vertical lidar ratio profile, providing for the first time, insight into the aerosol layers present at the H.E.S.S. site in Namibia.

5.2 Recommendations

This section outlines the authors various recommendations for improving the results discussed in Chapter 4.

The Fernald method was implemented with a constant lidar ratio (29 steradians)

using both the Fernald algorithm and the revised Klett solution. The results of the revised Klett solution are in good agreement with the results of the lidar manufacturer's closed-source software. However, the Fernald algorithm returns a higher probability of transmission, particularly above the planetary boundary layer. There is no apparent reason for this other than the intrinsic performance of the respective algorithms. It is recommended that the Fernald method be implemented using a vertical lidar ratio profile because the lidar ratio does not remain constant for all altitudes. It is also recommended that it be investigated whether the performance of the Fernald algorithm and the revised Klett solution can be tested by analysing the trigger rates of the H.E.S.S. Cherenkov telescopes for observations taken at the same time as the lidar measurements. It might be possible to use the cosmic ray trigger rate, although a well known constant gamma ray source located close to zenith may be better.

The implementation of the multi-angle method returns an unsatisfactory probability of transmission profile. It is concluded that this is a result of not taking large zenith angle measurements (>60°) rather than a consequence of the local atmosphere being horizontally inhomogeneous. Even if further multi-angle measurements are taken it is suggested that using the multi-angle method, with the Easy-Lidar ALS450XT, may not be adequate for ground-based very high energy gamma ray astronomy because measurement of large zenith angles drastically reduces the observable height as a result of the $\sec\theta$ dependence. Therefore, with the multi-angle method, the Easy-Lidar ALS450XT is not powerful enough to monitor the region where gamma-ray-induced Cherenkov air showers reach their maximum. However, the multi-angle method can be used with the Easy-Lidar ALS450XT in order to probe the planetary boundary layer where the majority of

aerosols are located.

The functional relationships between the extinction and backscatter coefficients were analysed. A 5^{th} order polynomial function was applied to represent the relationship between extinction and backscatter. This can be useful for estimating the backscatter coefficient values which are not currently being generated by the lidar manufacturer's closed-source software. A 6^{th} order polynomial was applied to represent the relationship between the lidar ratio and the extinction coefficient. This function can be used to generate a vertical lidar ratio profile using the lidar generated extinction coefficients, and it is strongly recommended that the Fernald method be implemented using this vertical lidar ratio profile.

To improve the Mie scattering analysis, it is encouraged that this be extended to include non-spherical particles. The resulting functional relationships will then improve upon the first order approximations presented in this thesis. It is also recommended that empirical evidence of the aerosols at the H.E.S.S. site be collected in order to test if they can be approximated by spherical particles. Furthermore, this evidence will enable the local aerosols to be compared with the desert dust aerosol model.

Investment in either a Raman lidar or a High Spectral Resolution Lidar (HSRL) [4][39] should be considered in order to overcome a fundamental problem endured by all single-scattering lidars, i.e. two physical quantities (the extinction and backscatter coefficients) must be estimated from only one measured quantity. Both of these lidars can improve upon the existing lidar capabilities by providing either an insight into the relative abundance of certain scatterers or by providing greater accuracy of the molecular and aerosol contributions including independent

measures of the extinction and backscatter coefficients. It is reported that single scattering lidars, like the one used in this work, have a systematic uncertainty of up to 30% associated with calculating the backscatter coefficient compared to 5% - 10% for a Raman or HSRL lidar. [44] Therefore, investing in either of these two types of lidar should lead to reduced uncertainty in the calculation of the inferred gamma ray energies detected by H.E.S.S. and future ground based very high energy gamma ray astronomy instruments such as the Cherenkov Telescope Array (CTA).

The atmosphere is variable in both time and space, and the atmospheric data analysed in this thesis was recorded during the day at the H.E.S.S. site in Namibia. Therefore, in order to accurately correct the inferred gamma ray energies using the derived probability of transmission, it is recommended that lidar measurements be taken at the same time as observations with the H.E.S.S. Cherenkov telescopes. If this is not practical then lidar measurements should be taken immediately before and after observations.

5.2.1 Implementing this work into H.E.S.S.

A significant population of aerosols can dim the images seen by the H.E.S.S. telescopes, and if this is not corrected, the gamma ray event will be recorded with a lower energy than it actually has [42]. It is possible to implement the findings of this work into the H.E.S.S. event reconstruction by folding in a modelled atmospheric probability of transmission. Instead of using the lidar manufacturer's closed-source probability of transmission, the model can use the independently reconstructed probability of transmissions presented in this work. These single

wavelength calculations can be folded in with a MODTRAN extrapolated probability of transmission for all other wavelengths of interest. Each method can be compared to see the overall affect on the reconstructed event energy. Finally, any future lidar investment should allow for a multi-wavelength lidar to reduce the systematic error associated with extrapolating the probability of transmission profile for all wavelengths of interest.

5.3 Future Work

This section outlines the work that will be done in the near future to improve the results presented in this thesis. The intention is to implement many of the recommendations suggested in Section 5.2. This includes implementing the Mie analysis with a non-spherical element as well as analysing the new functional relationships between the extinction and backscatter coefficients to produce a new vertical lidar ratio profile. It will be investigated whether the Fernald algorithm and the revised Klett method can be tested against the H.E.S.S. telescope trigger rates by taking lidar measurements at the same time as H.E.S.S. telescope observations of a known constant source such as the Crab.

Once the lidar analysis techniques have been tested then further atmospheric measurements should be taken at the same time as H.E.S.S. telescope observations. The derived probability of transmission data, in addition to MODTRAN extrapolated transmissions, will be used to analyse the observations of some H.E.S.S. sources in order to monitor the gamma ray retention rate. For example, the effect on the number of Cherenkov photons detected for different gamma

ray energies will be monitored as a result of including the derived probability of transmission values. Furthermore, investigation into whether it is possible to conduct active atmospheric calibration of a H.E.S.S. source using the vertical lidar ratio profile as an indicator of aerosol layer heights, will be conducted.

Future ground-based very high energy gamma ray instruments, such as CTA mentioned in Section 5.2, will also require atmospheric monitoring. CTA is expected to cover an area spanning ≈ 1 km^2, which is much greater than the existing very high energy ground based experiments. The work presented in this thesis, and continuing research by the author, will contribute toward the design study currently being conducted by the atmospheric and calibration working group of the CTA consortium. This includes researching the best methods and analyses for atmospheric monitoring of such a large ground-based gamma ray observatory as well as how current and future atmospheric analysis might be implemented into the event reconstruction of a CTA size observatory [41].

Appendix

```
/*-----------------------------------------------------------------------------

 Beginning of Bohren and Huffman's (BHMIE) code
 translated into C++ Draine & Flatau (Princeton Univ.)
 Minor adjustments have been made to this code by C.Rulten (University of Durham)

-----------------------------------------------------------------------------*/


/*
     Subroutine BHMIE is the Bohren-Huffman Mie scattering subroutine
     to calculate scattering and absorption by a homogenous isotropic
     sphere.
  Given:
     X = 2*pi*a/lambda
     REFREL = (complex refr. index of sphere)/(real index of medium)
     NANG = number of angles between 0 and 90 degrees
            (will calculate 2*NANG-1 directions from 0 to 180 deg.)
  Returns:
     S1(1 .. 2*NANG-1) =  (incid. E perp. to scatt. plane,
                                scatt. E perp. to scatt. plane)
     S2(1 .. 2*NANG-1) =  (incid. E parr. to scatt. plane,
                                scatt. E parr. to scatt. plane)
     QEXT = C_ext/pi*a**2 = efficiency factor for extinction
     QSCA = C_sca/pi*a**2 = efficiency factor for scattering
     QBACK = 4*pi*(dC_sca/domega)/pi*a**2
```

```
            = backscattering efficiency
       GSCA = <cos(theta)> for scattering

    Original program taken from Bohren and Huffman (1983), Appendix A
    Modified by B.T.Draine, Princeton Univ. Obs., 90/10/26
    in order to compute <cos(theta)>
    This code was translatted to C by P. J. Flatau Feb 1998. The C
    version uses "Numerical Recipes" public domain code for complex
    arithmetics "complex.c" and "nrutil.c" (http://www.nr.com).

*/



void  bhmie(double x,dcomplex cxref, unsigned long nang,dcomplex cxs1[],
 dcomplex cxs2[],double  *qext, double *qsca, double *qback, double *gsca)

{

  //------------------------------------------------------------------------
  // Array Arguments
  // COMPLEX :: cxs1(2*mxnang-1), cxs2(2*mxnang-1)
  // Local Scalars
  //------------------------------------------------------------------------

  dcomplex cxan, cxan1, cxbn, cxbn1, cxxi, cxxi0, cxy, cxxi1;
  dcomplex cxtemp;

  double apsi, apsi0, apsi1, chi, chi0, chi1, dang, fn, p, pii;
  double rn, t, theta, xstop, ymod;
  double  dn, dx, psi, psi0, psi1;

  unsigned int  j, jj, n, nmx, nn, nstop;

  //------------------------------------------------------------------------
  // Local Arrays
  //------------------------------------------------------------------------
```

```
dcomplex cxd[nmxx];

double amu[mxnang], pi[mxnang], pi0[mxnang], pi1[mxnang], tau[mxnang];

//------------------------------------------------------------------------


if (nang>mxnang)
  {
    printf(" STOP '***Error: NANG > MXNANG in bhmie");
    return;
  }

pii = 4.0*atan(1.0); //changed C.Rulten 20/02/08
dx = x;
cxy = Cmul(Complex(x,0.0),cxref);

//Series expansion terminated after NSTOP terms

xstop = x + 4.0*pow(x,0.3333) + 2.0; //changed C.Rulten 20/02/08
nstop = int(xstop); //implicit data type conversion made by C.Rulten 7th Feb 2008
ymod = Cabs(cxy);
nmx = int(FMAX(xstop,ymod) + 15);//implicit data type conversion made by C.Rulten 7th Feb 2008

if (nmx>nmxx)
  {
    printf(" x, nmx, nmxx, cxref %f %i %i  \n ", x, nmx, nmxx);
    printf(" xstop nstop ymod %f %i %f \n", xstop, nstop, ymod);
    printf(" Error: NMX > NMXX= %i \n", nmxx);
    return;
  }

dang = 0.5E0*pii/ (double)(nang-1);
for (j = 1; j<=nang; j++)
  {
    theta = (double)(j-1)*dang;
```

```
      amu[j] = cos(theta);
    }

//---------------------------------------------------------------------------
// Logarithmic derivative D(J) calculated by downward recurrence beginning
// with initial value (0.,0.) at J=NMX
//---------------------------------------------------------------------------


  cxd[nmx] = Complex(0.0E0,0.0E0);
  nn = nmx - 1;

  for (n = 1; n<= nn; n++)
    {
      rn = (double)nmx - (double)n + 1.0;

      //cxd(nmx-n) = (rn/cxy) - (1.E0/(cxd(nmx-n+1)+rn/cxy))
      cxtemp=Cadd(cxd[nmx-n+1],Cdiv(Complex(rn,0.0),cxy));
      cxtemp=Cdiv(CXONE,cxtemp);
      cxd[nmx-n]=Csub(Cdiv(Complex(rn,0.0),cxy),cxtemp);
    }

  for ( j = 1; j <= nang; j++)
    {
      pi0[j] = 0.0E0;
      pi1[j] = 1.0E0;
    }

  nn = 2*nang - 1;

  for(j = 1; j<= nn; j++)
    {
      cxs1[j] = Complex(0.0E0,0.0E0);
      cxs2[j] = Complex(0.0E0,0.0E0);
    }

  //---------------------------------------------------------------------------
```

```
//Riccati-Bessel functions with real argument X calculated by upward recurrence
//-------------------------------------------------------------------------

psi0 = cos(dx);
psi1 = sin(dx);
chi0 = -sin(x);
chi1 = cos(x);
apsi0 = psi0;
apsi1 = psi1;
cxxi0 = Complex(apsi0,-chi0);
cxxi1 = Complex(apsi1,-chi1);
*qsca = 0.0E0;
*gsca = 0.0E0;

for ( n = 1; n <= nstop; n++)
  {
    dn = (double)n;
    rn = (double)n;
    fn = (2.0E0*rn+1.0E0)/(rn*(rn+1.0E0));
    psi = (2.0E0*dn-1.0E0)*psi1/dx - psi0;
    apsi = psi;
    chi = (2.0E0*rn-1.0E0)*chi1/x - chi0;
    cxxi = Complex(apsi,-chi);

    // Store previous values of AN and BN for use in computation of g=<cos(theta)>

    if (n>1)
{
  cxan1 = cxan;
  cxbn1 = cxbn;
}

    //Compute AN and BN:
    //cxan = (cxd(n)/cxref+rn/x)*apsi - apsi1;

    cxan=Cdiv(cxd[n],cxref);
    cxan=Cadd(cxan,Complex(rn/x,0.0));
```

```
        cxan=Cmul(cxan,Complex(apsi,0.0));
        cxan=Csub(cxan,Complex(apsi1,0.0));

        //cxan = cxan/((cxd(n)/cxref+rn/x)*cxxi-cxxi1);
        cxtemp=Cdiv(cxd[n],cxref);
        cxtemp=Cadd(cxtemp,Complex(rn/x,0.0));
        cxtemp=Cmul(cxtemp,cxxi);
        cxtemp=Csub(cxtemp,cxxi1);
        cxan=Cdiv(cxan,cxtemp);

        //cxbn = (cxref*cxd(n)+rn/x)*apsi - apsi1;
        cxbn=Cmul(cxref,cxd[n]);
        cxbn=Cadd(cxbn,Complex(rn/x,0.0));
        cxbn=Cmul(cxbn,Complex(apsi,0.0));
        cxbn=Csub(cxbn,Complex(apsi1,0.0));
        //cxbn = cxbn/((cxref*cxd(n)+rn/x)*cxxi-cxxi1);
        cxtemp=Cmul(cxref,cxd[n]);
        cxtemp=Cadd(cxtemp,Complex(rn/x,0.0));
        cxtemp=Cmul(cxtemp,cxxi);
        cxtemp=Csub(cxtemp,cxxi1);
        cxbn=Cdiv(cxbn,cxtemp);

        //Augment sums for *qsca and g=<cos(theta)>
        //*qsca = *qsca + (2.*rn+1.)*(cabs(cxan)**2+cabs(cxbn)**2);
        *qsca = *qsca + (2.0*rn+1.0)*(Cabs(cxan)*Cabs(cxan)+Cabs(cxbn)*Cabs(cxbn));
        *gsca = *gsca + ((2.0*rn+1.0)/(rn*(rn+1.0)))*(cxan.r*cxbn.r+cxan.i*cxbn.i);

        if (n>1)
{
  *gsca = *gsca + ((rn-1.0)*(rn+1.0)/rn)*(cxan1.r*cxan.r+cxan1.i*cxan.i+cxbn1.r*cxbn.r+cxbn1.i*cxbn.i);
}

        for ( j = 1; j<= nang; j++)
{
            jj = 2*nang - j;
            pi[j] = pi1[j];
            tau[j] = rn*amu[j]*pi[j] - (rn+1.0E0)*pi0[j];
```

```
        p = pow(-1.0,n-1);

//cxs1[j] = cxs1[j] + fn*(cxan*pi[j]+cxbn*tau[j]);
        cxtemp=Cmul(cxan,Complex(pi[j],0.0));
        cxtemp=Cadd(cxtemp,Cmul(cxbn,Complex(tau[j],0.0)));
        cxtemp=Cmul(Complex(fn,0.0),cxtemp);
        cxs1[j]=Cadd(cxs1[j],cxtemp);
        t = pow(-1.0,n);

//cxs2[j] = cxs2[j] + fn*(cxan*tau[j]+cxbn*pi[j]);
        cxtemp=Cmul(cxan,Complex(tau[j],0.0));
        cxtemp=Cadd(cxtemp,Cmul(cxbn,Complex(pi[j],0.0)));
        cxtemp=Cmul(Complex(fn,0.0),cxtemp);
        cxs2[j]=Cadd(cxs2[j],cxtemp);

        if (j!=jj)
  {
    //cxs1[jj] = cxs1[jj] + fn*(cxan*pi(j)*p+cxbn*tau(j)*t);
    cxtemp=Cmul(cxan,Complex(pi[j]*p,0.0));
    cxtemp=Cadd(cxtemp,Cmul(cxbn,Complex(tau[j]*t,0.0)));
    cxtemp=Cmul(Complex(fn,0.0),cxtemp);
    cxs1[jj]=Cadd(cxs1[jj],cxtemp);

    //cxs2[jj] = cxs2[jj] + fn*(cxan*tau(j)*t+cxbn*pi(j)*p);
    cxtemp=Cmul(cxan,Complex(tau[j]*t,0.0));
    cxtemp=Cadd(cxtemp,Cmul(cxbn,Complex(pi[j]*p,0.0)));
    cxtemp=Cmul(Complex(fn,0.0),cxtemp);
    cxs2[jj]=Cadd(cxs2[jj],cxtemp);
  }
     }

    psi0 = psi1;
    psi1 = psi;
    apsi1 = psi1;
    chi0 = chi1;
    chi1 = chi;
    cxxi1 = Complex(apsi1,-chi1);
```

```
      //---------------------------------------------------------------
      //  For each angle J, compute pi_n+1 from PI = pi_n , PI0 = pi_n-1
      //---------------------------------------------------------------

      for ( j = 1; j<= nang; j++)
{
  pi1[j] = ((2.0*rn+1.0)*amu[j]*pi[j]-(rn+1.0)*pi0[j])/rn;
  pi0[j] = pi[j];
}
    } //end of big for loop

  //---------------------------------------------------------------
  //Have summed sufficient terms.Now compute *qsca,*qext,*qback,and *gsca
  //---------------------------------------------------------------

  *gsca = 2.0*( *gsca/ *qsca);
  *qsca = (2.0E0/(x*x))* *qsca;
  *qext = (4.0E0/(x*x))*cxs1[1].r;
  *qback = (4.0E0/(x*x))*Cabs(cxs1[2*nang-1])*Cabs(cxs1[2*nang-1]);


  return;
} //end of function bhmie
```

Bibliography

[1] **Ackermann.J**. Analytical solution of the two-frequency lidar inversion technique. *Applied Optics*, 38(36):7414–7418 (1999).

[2] **Aharonian.F**. Search for Gamma-rays from Dark Matter annihilations around Intermediate Mass Black Holes with the H.E.S.S. experiment. *astro-ph 0806.2981v2* (2008).

[3] **Ansmann.A** and **Muller.D**. *Lidar and Atmospheric Aerosol Particles*, pages 105–141. Springer (2005). ISBN 0-387-40075-3.

[4] **Argall.P.S** and **Sica.R.J**. *Lidar (Laser Radar)*, volume 2, chapter Lidar-Laser Radar, pages 1305–1322. Wiley-VCH Verlag GmbH and Co KGaA (2003).

[5] **Badran.H.M** and **Horan.D**. Gamma-Ray Astronomers Detect "Extreme" Galaxies (2001). Last accessed: 30th April 2009, URL `http://perry.sonoma.edu/gamma2001/wednesday/badran-horan/presentation.html`.

[6] **Barnaba.F** and **Gobbi.G.P**. Lidar estimation of tropospheric aerosol extinction, surface area and volume: Maritime and desert-dust cases. *Journal of Geophysical Research*, 106(D3):3005–3018 (2001).

[7] **Barnaba.F et al.** Extinction versus backscatter relationships for lidar applications at 351nm: maritime and desert aerosol simulations and comparison with observations. *Atmospheric Research*, (70):229–259 (2004).

[8] **Benzvi.S.Y et al.** The Lidar system of the Pierre Auger Observatory. *Nuclear Instruments and Methods in Physics Research*, A(574):171–184 (2007).

[9] **Bernlöhr.K**. Impact of atmospheric parameters on the atmospheric Cherenkov technique. *Astroparticle Physics*, 12:255–268 (2000).

[10] **Bilitza.D.K**. U.S. Standard Atmosphere 1976 (2008). Last Accessed: 13th December 2008, URL `http://modelweb.gsfc.nasa.gov/atmos/us_standard.html`.

[11] **Bishop.C**. *Astrophysics*. John Murray Publishers Ltd, 50 Ablemarle Street, London, UK (2000). ISBN 0-7195-8590-2.

[12] **Blackwood.J.D et al.** Exploring the Extreme Universe: Science Writers Guide (2008). Last accessed: 30th April 2009, URL `http://www.nasa.gov/mission_pages/GLAST/news/index.html`.

[13] **Bohren.C.F** and **Huffman.D.R**. *Absorption and Scattering of Light by Small Particles*. Wiley-VCH Verlag GmbH and Co KGaA, Weinheim, Germany (2004). ISBN 978-0-471-29340-8.

[14] **C.A.N.G.A.R.O.O.** (Collaboration of Australia and Nippon (Japan) for a GAmma Ray Observatory in the Outback) (2009). Last accessed: 9th January 2009, URL `http://icrhp9.icrr.u-tokyo.ac.jp/`.

[15] **Carnuth.W** and **Reiter.R**. Cloud extinction profile measurements by lidar using Klett's inversion method. *Applied Optics*, 25(17):2899–2907 (1986).

[16] **Davies.J.M** and **Cotton.E.S.** Design of the quartermaster solar-furnace. *Solar Energy*, 1:16 – 22 (1957).

[17] **de Hulst.H.C V.** *Light Scattering by Small Particles*. Dover Publications Inc, 180 Varick Street, New York, USA, dover edition (1981). ISBN 0-486-64228-3.

[18] **DeAngelis.A**. Very-High Energy Gamma Astrophysics. *astro-ph 0712.0315v1* (2007). 0712.0315v1.

[19] **Draine.B.T** and **Flatau.P**. Scattering and Absorption of Light by Small Particles (2008). Last accessed: 14th December 2008, URL `http://www.astro.princeton.edu/~draine/scattering.html`.

[20] **Duncan.R.C.** and **Thompson.C**. Formation of very strongly magnetized neutron stars: implications for gamma-ray bursts. *The Astrophysical Journal*, 392:9–13 (1992).

[21] **Fernald.F.G**. Analysis of atmospheric lidar observations: some comments. *Applied Optics*, 23(5):652–653 (1984).

[22] **Fernald.F.G et al.** Determination of Aerosol Height Distributions by Lidar. *Journal of Applied Meterology*, 11:482–489 (1972).

[23] **Filipčič.A et al.** Scanning lidar based atmospheric monitoring for flourescence detectors of cosmic showers. *Astroparticle Physics*, 18:501–512 (2003).

[24] **Gaisser.T.K.** *Cosmic Rays and Particle Physics.* Cambridge University Press (1990). ISBN 0-521-33931-6.

[25] **Grieder.P.** *Cosmic rays at Earth: researcher's reference manual and data book.* Elsevier Science B.V., P.O. Box 211, 1000 AE, Amsterdam, The Netherlands, first edition (2001). ISBN 0-444-50710-8.

[26] **Grupen.C.** *Astroparticle Physics.* Springer-Verlag, Berlin Heidelberg (2005). ISBN 3-540-25312-2.

[27] **Hess.M et al.** Optical Properties of Aerosols and Clouds: The Software Package OPAC. *Bulletin of the American Meteorological Society*, 79(5):831–844 (1998).

[28] **Hinton.J.** Ground based gamma-ray astronomy with Cherenkov Telescopes. *astro-ph 0803.1609v2* (2008). 0803.1609v2.

[29] **Hoke.M.** MODTRAN: MODerate resolution atmospheric TRANsmission (2008). Last Accessed: 13th December 2008, URL `http://www.kirtland.af.mil/afrl_vs/ir_clutter/index.asp`.

[30] **Houghton.J.** *The Physics of the Atmosphere.* Cambridge University Press, third edition (2002). ISBN 0-521-01122-1.

[31] **Iyengar.V.S et al.** The Absorption of Soft X-rays from the Crab Nebula. *Astrophysics and Space Science*, 32:431–446 (1975).

[32] **Klett.J.D.** Stable analytical inversion solution for processing lidar returns. *Applied Optics*, 20(2):211–220 (1981).

[33] **Klett.J.D.** Lidar inversion with variable backscatter/extinction ratios. *Applied Optics*, 24(11):1638–1643 (1985).

[34] **Knauss.D.C.** Significance of the boundary value term in the Klett lidar inversion formula. *Applied Optics*, 21(23):4194 (1982).

[35] **Konopelko.A et al.** The TeV Energy Spectrum of Mrk 421 Measured in A High Flaring State. *astro-ph 0708.3857* (2007). 0708.3857.

[36] **Longair.M.S.** *High Energy Astrophysics.* Cambridge University Press, second edition (1992). ISBN 0-521-38773-6.

[37] **M.A.G.I.C.** (Major Atmospheric Gamma-ray Imaging Cherenkov) (2009). Last accessed: 9th January 2009, URL `http://wwwmagic.mppmu.mpg.de/`.

[38] **Marshall.H et al.** M87's Energetic Jet (2004). Last accessed: 30th April 2009, URL `http://antwrp.gsfc.nasa.gov/apod/ap041211.html`.

[39] **McGill.M.J**. *Lidar-Remote Sensing*, pages 1103–1113. CRC Press (2003). ISBN 0-824-74251-6.

[40] **Mishchenko.M et al.** *Light Scattering by Nonspherical Particles*. Academic Press (2000). ISBN 0-12-498660-9.

[41] **Nolan.S.J** and **Rulten.C**. Studies of Lidar Calibration for the Next Generation of Imaging Atmospheric Cherenkov Telescopes. *Proceedings of 31st International Cosmic Ray Conference* (2009).

[42] **Nolan.S.J et al.** Active Atmospheric Calibration for H.E.S.S applied to PKS 2155-304. *Proceedings of 30th International Cosmic Ray Conference* (2007).

[43] **Pahlow.M et al.** Calibration method for multiangle lidar measurements. *Applied Optics*, 43(14):2948–2956 (2004).

[44] **Papayannis.A** and **Fokitis.E**. Laser Remote Sensing Techniques for Vertical Profiling of Cloud and Aerosol Extinction and Back-scatter in the Lower Atmosphere. *PAO Internal Note*, GAP(1998-018) (1998). Last accessed: 29th April 2009, URL `http://www.auger.org/technical_info/`.

[45] **Pontikis.A**. Nobel Prize in Physics (2008). Last accessed: 17th December 2008, URL `http://nobelprize.org/nobel_prizes/physics/laureates/1936/index.html`.

[46] **Rees.W.G**. *Physical Principles of Remote Sensing*. Cambridge University Press, 2nd edition (2001). ISBN 0-521-66948-0.

[47] **Rocadenbosch.F**. *Lidar - Aerosol Sensing*, pages 1090–1100. CRC Press (2003). ISBN 0-824-74251-6.

[48] **Sandeman.K et al.** Raman Spectroscopy (2007). Last accessed: 26th January 2009, URL `http://www.doitpoms.ac.uk/tlplib/raman/index.php`.

[49] **Seward.F.D et al.** CHANDRA Observations of the X-ray Halo around the Crab Nebula. *The Astrophysical Journal*, 636:873–880 (2006).

[50] **Spangler.D.H**. *Atmospheric monitoring and gamma-ray data anlaysis with the H.E.S.S. telescope array*. Ph.D. thesis, University of Durham (2008).

[51] **Swordy.S**. Cosmic Ray Spectrum Picture (2008). Last accessed: 30th April 2009, URL `http://astroparticle.uchicago.edu/announce.htm`.

[52] **V.E.R.I.T.A.S.** (Very Energetic Radiation Imaging Telescope Array System) (2009). Last accessed: 9th January 2009, URL `http://veritas.sao.arizona.edu/`.

[53] **Wakely.S** and **Horan.D**. TeVCat (2009). Last accessed: 10th January 2009, URL `http://tevcat.uchicago.edu/`.

[54] **Weekes.T.C**. *Very High Energy Gamma Astronomy*. IOP Publishing Ltd (2003). ISBN 0-7503-0658-0.

[55] **Young.S**. Analysis of lidar backscatter profiles in optically thin clouds. *Applied Optics*, 34(30):7019–7031 (1995).